Ministry of Higher Education and Scientific Research

University 8 Mai 1945 Guelma

Faculty of Sciences and Engineering

ELECTRONIC, MAGNETO-OPTICAL AND THE MAGNETIC PROPERTIES OF THE COMPOUNDS BASED ON THE TRANSITION METALS AND THE ELEMENTS OF THE GROUPS III, IV AND VI.

A thesis presented to the Physics Department at the Faculty of Sciences and Engineering at the University 08 Mai 1945 in partial fulfilment of the requirements for the degree of ‘’Doctorat en Sciences’’ in Physics.

By

Ali HAMIDANI

Examining board:

President:	*Ahmed BOUFELFEL*	Prof.	University of Guelma
Supervisor:	*Badis BENNECER*	Prof.	University of Guelma
Examiners:	*Abdelhamid LAYADI*	Prof.	University of Setif
	Bachir BOUHAFS	Prof.	University of SBA

2010

ABSTRACT

We have studied the different properties of two kinds of materials; the first one is composed of two transition metals and one non-metallic *sp* element and the second contains one transition metal and two non-metallic elements. In this thesis we focused on the electronic, optical, magnetic and magneto-optical properties of the Pd based compounds PdMnSb, Pd_2MnSb, PdX_2 and PdPX where (X=S and Se). We are also investigate the structural, electronic and magneto-optical properties of the IrMnZ, with (Z=Al, Sn and Sb). The calculations are based on the total-energy calculations within the full-potential augmented plane-wave plus local orbitals (FP-LAPW + LO) method. We have used both the local density approximation (LDA) and generalized gradient approximation (GGA) for the exchange and correlation potential with and without including the spin-orbit effect. In order to investigate the importance of correlation, we have used the (LSDA+U) and (GGA+U). The structural properties are determined through the total energy minimization and interatomic forces calculations.

The results exhibit that IrMnZ are ferromagnetic and they are mechanically stable at zero pressure. The local spin density approximation (LSDA) predicts that the IrMnSb is a half metallic and the IrMnAl compound has negligible magnetic moment. Furthermore, the LSDA+U and the GGA+U predict a large magnetic moment. Furthermore, the GGA gives good values compared with the experimental ones. Our results show that the highest Kerr rotation arises in the IrMnSb compound, while weak values are found in IrMnAl with all the approximations used.

We have also investigated the electronic and magneto-optical properties of the Heusler compounds PdMnSb and Pd_2MnSb. Our LSDA calculations reveal a gap at E_F, predicting a half metallic nature in PdMnSb, but the LSDA+U and the GGA+U destroy this gap. We show also that the LSDA+U can produce accurately the optical properties, while the magneto-optical properties are well reproduced with the LSDA. Furthermore, we found that the magnetic and magneto-optical properties are sensitive to the change of the U parameter.

The structural and electronic properties of PdX_2 (X=P, S and Se) are investigated. Our results show that the studied compounds exhibit a metallic character with LDA. Furthermore, the LDA+U predicts that PdS_2 compound is a semiconductor with a narrow gap. The calculated anisotropic frequency dependent dielectric functions, reflectivity, refractive index and absorption spectra are obtained and discussed for PdPX where(X=S and Se).

RESUME

Nous avons étudié les différentes propriétés de deux types de matériaux, le premier est composé de deux métaux de transition et un élément non métallique *sp* et le second contient un élément de transition et deux éléments non-métalliques. Dans cette thèse nous avons focalisé sur l'étude des propriétés l'électronique, optiques, magnéto-optiques des composés à base de Pd; Pd_2MnSb, PdMnSb, PdX_2 et PdPX où X = S et Se, nous avons également étudié les propriétés des composés IrMnZ, avec Z = Al , Sn et Sb. Le calcul a été effectué en utilisant la méthode linéaire des ondes planes augmentées à potentiel total plus les orbitales locales (FP-LAPW + LO). Nous avons utilisé l'approximation de la densité locale (LDA) et l'approximation du gradient généralisé (GGA) pour le potentiel d'échange et de corrélation, avec et sans l'inclusion de l'effet de spin-orbite. En outre on a étudié l'effet de la corrélation, nous avons utilisé l'approximation de la densité de spin locale plus le paramètre de Hubbard U (LSDA + U) et l'approximation du gradient généralisé de la densité plus le paramètre de Hubbard U (GGA + U)

Les résultats montrent que les composés IrMnZ sont ferromagnétiques et ils sont mécaniquement stable à pression nulle. L'approximation de la densité de spin locale (LSDA) prédit que la IrMnSb est un semi-métal et le composé IrMnAl possède un moment magnétique négligeable. En outre, LSDA+U (GGA+U) donnent un moment magnétique important. Alors que les valeurs obtenues avec la GGA sont proches de celles mesurées. Nos résultats montrent que le composé IrMnSb possède une grande valeur de rotation de Kerr, par contre celle de IrMnAl est la plus petite avec toutes les approximations utilisées.

Nous avons également étudié les propriétés électroniques et magnéto-optiques des composés de Heusler PbMnSb et Pb_2MnSb. Nos calculs LSDA révèlent un gap à E_F, donnant ainsi la nature semi-métallique de PbMnSb, mais la LSDA+U et la GGA+U détruisent ce gap. Nous avons aussi montré que la LSDA+U produit des propriétés optiques précises, tandis que les propriétés magnéto-optiques sont bien reproduites avec la LSDA. En outre, nos résultats montrent que les propriétés magnétiques et magnéto-optiques sont sensibles à la variation du paramètre U.

Les propriétés structurales et électroniques des composés PdX_2 (X = P, S et Se) sont étudiées. Nos résultats montrent que les composés étudiés présentent un caractère métallique avec la LDA, par contre PdS_2 devient un semi-conducteurs LDA+U. Finalement, les structures de bande, les éléments du tenseur diélectrique, la réflectivité, l'indice de réfraction et les spectres d'absorption sont obtenues et analysées pour les composés ternaires PdPX (X = S et Se).

ملخص

قمنا بدراسة مختلف الخصائص لنوعين من المركبات. الأولى تحتوي على عنصرين من العناصر الإنتقالية و الآخر من العناصر الغير معدنية أما النوع الثاني يحتوي على عنصرين من العناصر الغير معدنية و الآخر معدني. في هذه الأطروحة ركزنا على دراسة الخصائص الإلكترونية, الضوئية المغناطيسية و الضوئية الممغنطة, باستعمال حسابات المبدأ الأول ,للمركبات التي تحتوي على عنصر البالديوم وهي المركبات Pd_2MnSb, PdMnSb PdX_2 و PdPX حيث ان (X=S, Se) إضافة إلى دلك قمنا بدراسة خصائص المركبات IrMnZ حيث ان (Sb و Z=Al, Sn) و ذلك بإستعمال الطريقة FP-LAPW+LO كما تم استعمال تقريب الكثافة المحلية LDA و تقريب التدرج العام GGA لتحديد كمون التبادل و التعالق. من أجل التحقق من أهمية الترابط, قمنا بإستعمال تقريب الكثافة المحلية و تقريب التدرج العام مضاف إليه ثابت هيبارد (*GGA*)+U و*LSDA*(*LDA*)+U.مع إدخال الفعل سبين-مدار spin-orbit. الخواص البنيوية تم تحديدها عن طريق التقليل من الطاقة الكلية للمركب و القوى المؤثرة على الذرات. بالنسبة للخواص الضوئية؛ الانعكاسية، معامل الانكسار وأطياف الامتصاص تم الحصول عليها ومناقشتها

النتائج بينت ان IrMnZ مغناطيسي حديدي ferromagnetic وميكانيكيا مُسْتَقِرّ في إنعدام الضغط. من جهة اخرى بينت LDA ان العزم المغناطيسي مهمل و ان IrMnSb نصف ناقل half metallic. LSDA+U (GGA+U) تعطي عزم مغناطيسي كبيرعكس GGA التي اعطت قيم متوافقة مع التجريبي.

بالنسبة للمركبات PbMnSb وPb_2MnSb فإن LDA تنبأت بأن PbMnSb نصف ناقل half metallic لكن(LSDA+U (GGA+U بينت انه معدني. كما ان هده الأخيرة اعطت نتائج جيدة بالنسبة للخواص الضوئية إضافة إلى دلك أن الخصائص المغناطيسية والضوئية الممغنطة ، حساسة لتغيير ثابت هيبارد.

في هده الأطروحة قمنا بدراسة الخصائص البنيوية والإلكترونية للمركبات PdX_2 و PdPX حيث ان (X=S و Se) وعلاوة على ذلك نجد أن PdS_2 من أشباه الموصلات على عكس النتائج التي تنبأت بها LDA و GGA.

To my parents, my wife, my daughter and my all family for their support

ACKNOWLEDGMENTS

First I would like to express my gratitude to my supervisor, Professor Badis BENNECER (Department of Physics, University 8 Mai 1945 Guelma) for his guidance and support at all stages during the preparation of this thesis. His vast experience and insight into condensed matter physics, and in particular his high level for written and spoken expression has greatly contributed to my professional development. He has taught me to find my own path in my research.

I would like to thank Professor *Ahmed BOUFELFEL (*Department of Physics, University 8 Mai 1945 Guelma)*)* who has accepted reading and commenting on the thesis and presiding the examining board.

It is difficult to find sufficient words to thank the member of jury Prof. *Abdelhamid LAYADI* (Department of Physics, University Abbas Ferhat Setif) and *Prof. Bachir BOUHAFS* (Department of Physics, University Djilali Liabes Sidi BelAbbes) who have accepted reading and commenting on my work.

One more thing needs to be added, I would like to express my deepest gratitude to Prof. A. Boufelfel (head of the Guelma Physics Laboratory) and Prof. Bennecer (head of computational group) who gave me the opportunity to fulfill this work and to enjoy my stay at Guelma Physics Laboratory.

The Computational Quantum Theory Group, Technical University, Vienna is acknowledged for providing us the software code WIEN2K used in these calculations.

A special thank to my friends for their support and encouragement. Finally, I would like to thank my family for their constant support and encouragement.

LIST OF FIGURES

LIST OF TABLES

CONTENTS

INTRODUCTION

Transition metals comprise roughly half of the periodic table of elements; they are found between the group *IIA* elements and the Group *IIB* elements in the periodic table. The group *IIB* is sometimes considered transition elements. This class of elements is also known as the d-block elements, because the outermost main levels have incompletely filled d sub-orbitals. Transition Metals are rarely applied in their pure state; they are most often put in use in the form of alloys that exploit or strengthen desirable properties and overcome characteristics that limit performance. These elements readily form alloys with each other [1] or with other non-metals elements [2].

Over the past two decades, considerable progress has been made in the synthesis and characterization of compounds containing transition metals. Furthermore, various types of alloys containing transition metals exhibit special physical, chemical and mechanical properties that result from choice of the metal and/or manipulation of composition and manufacturing processes.

In the past few years several compounds with XYZ phase (where one or more elements are transition elements) have been studied and their crystal structure, electronic and magnetic properties have been reported in a large number of papers [3,4]. The interest in these phases represents a normal development of research from binary to ternary alloys. Since the XY_2 compounds form the most numerous family in the binary systems, and new structures are found with the replacement of a partner atom Y by another partner Z. In most cases the ternary compounds have ordered structures. When a ternary phase crystallizes with a disordered structure and the Y and Z atoms are statistically distributed on the same sites, this is a structure already found in binary systems [5,6]. Moreover, many alloys which are established from the mixtures of transition metal and non-metallic element have gained great scientific and technological interest recently, due to their use in different areas.

Among this class of materials we find the Heusler alloys. These alloys have two distinct families; one of which crystallizes in the $L2_1$ structure. This family is known as the full-Heusler alloy and possesses an X_2YZ formula [7]. The second family is the half-Heusler alloy with XYZ formula [8], we will treat it in detail in the next chapter, and their electronic structure can range from metallic to semi-metallic or semiconducting behaviour [9]. The Heusler alloys are particularly interesting due to their very high Curie temperature [10,11] and some of them are already in use as

elements in multilayered magneto-electronic devices such as magnetic tunnel junctions and also as giant magnetoresistance spin valves [12]. Several papers have been devoted to the calculation of the structural, electronic and magnetic properties of these alloys and recently there has been an increased interest in thin films of this material both experimentally [13-15] and using first-principles calculations [16,17]. The Mn-based Heusler alloys (XMnZ) belong to a class with interesting magnetic properties, exhibiting ferromagnetic features like magneto-optical effects and giant magneto-resistance, a comprehensive study of Mn based compounds have been performed by Brown et al. [18] and Plogmann et al. [19].

For the other application, the technical development effort directed at layered transition metal chalcogenides (LTMCs) and their intercalation compounds. This in part is due to the structural and physical properties of these two-dimensional (2D) inorganic materials [20-23]. In the general case, these structures consist of infinite metal chalcogenide layers; within each layer the atoms are bound by strong covalent interactions, but the layers themselves interact only by weaker van der Waals forces. Transition-metal chalcogenides, in terms of composition, provide a wide variety of compounds which crystallize in different structure and many of the chemical and physical properties of these materials derive from this anisotropic layered structure.
Moreover, these compounds can be used as substrate for other materials and one of the interesting properties of these materials is the formation of intercalation complexes with foreign atoms or molecules, organic or inorganic, between the layers [24-25], because this offers perspectives for the realization of new materials especially those that can combine different properties in a single material.
Optical recording in general and magneto-optical recording in particular is the subject of great significance in optical data storage. In this thesis we focused on the effect of the metal and non-metal elements on the different properties; electronic, optical and magneto optical properties, using the FPLAPW method within the local spin density approximation (LSDA) and the generalized gradient approximation (GGA) and with the on-site Coulomb correction GGA+U and LSDA+U.

This thesis is organized as follows; we briefly review in chapter 1 some of the most basic understandings of the Heusler alloys and transition metal chalcogenide compounds and their crystalline structure. In Chapter 2, the formalism of Density Functional Theory is presented including the essential of the methods and the approximations for the practical calculations such as the Kohn-Sham-LDA scheme,

which is used in this work. Furthermore, the linearized augmented plane wave method used throughout this thesis is discussed in chapter 3. The results of this thesis are divided essentially into two parts which have been mainly devoted to the calculations of the different properties and the relationship between structural, electronic, optical and magneto-optical properties in different structures. In Chapter 4 the results of the ab initio calculations for Heusler alloys IrMnZ (Z=Al, Sn and Sb) are presented. In chapter 5 the electronic and magneto-optical properties and the influence of the electron-electron interaction and the double-counting corrections on these properties of the PdMnSb and Pd_2MnSb compounds are presented. The last two chapters (6 and 7) are devoted to the layered transition metal chalcogenides; the sixth chapter gives the structural and electronic properties of the pseudo-binary compounds PdX_2 (X= P, S and Se), while in the chapter 7 we present the electronic and optical properties of the orthorhombic compounds PdPX (X= S and Se). Finally, we provide a summary of the ideas presented here and their discussion.

REFERENCE

1- S. Mechler, M.-P. Macht, G. Schumacher, I. Zizak, and N. Wanderka Phys. Rev. B 81, (2010) 180101.

2- S.-H. Baek, M. J. Graf, A. V. Balatsky, E. D. Bauer, J. C. Cooley, J. L. Smith, and N. J. Curro

3- P. Klaer, M. Kallmayer, C. G. F. Blum, T. Graf, J. Barth, B. Balke, G. H. Fecher, C. Felser, and H. J. Elmers Phys. Rev. B 80, (2009) 144405.

4- G. W. Lee, A. K. Gangopadhyay, R. W. Hyers, T. J. Rathz, J. R. Rogers, D. S. Robinson, A. I. Goldman, and K. F. Kelton Phys. Rev. B 77, (2008) 184102.

5- K. Ishikawa, R. Kainuma, I. Ohnuma, K. Aoki, K. Ishida Acta Materialia 50 (2002) 2233.

6- H. Kawai, Y. Kaneno, M. Yoshida, T. Takasugi Intermetallics 11 (2003) 467.

7- R.A. de Groot, F.M. Mueller, P.G. van Engen, K.H.J. Buschow, Phys. Rev. Lett. 50 (1983) 2024.

8- R.B. Helmholdt, R.A. de Groot, F.M. Mueller, P.G. Van Engen, K.H.J. Buschow, J. Magn. Magn. Mater. 43 (1984) 249.

9- L. Offernes, P. Ravindran, A. Kjekshus, J. Alloys Compd. 439 (2007) 37.

10- P. Bach, A.S. Bader, C. Rüster, C. Gould, C.R. Becker, G. Schmidt, L.W. Molenkamp, , W.Weigand, C. Kumpf, E. Umbach, R. Urban, G.Woltersdorf, B. Heinrich, Appl. Phys. Lett. 83 (2003) 521.

11- K. Aoshima, N. Funabashi, K. Machida, Y. Miyamoto, K. Kuga, N. Kawamura, J. Magn. Magn. Mater. 310 (2007) 2018.

12- L.J. Singh, C.W. Leung, C. Bell, J.L. Prieto, Z.H. Barber, J. Appl. Phys. 100 (2006) 13910.

13- P. Turban, S. Andrieu, B. Kierren, E. Snoeck, C. Teodorescu, A. Traverse, Phys. Rev. B 65 (2002) 134417.

14- J. Giapintzakis, C. Grigorescu, A. Klini, A. Manousaki, V. Zorba, J. Androulakis, Appl. Phys. Lett. 80 (2002) 2716.

15- K.E.H.M. Hanssen, P.E. Mijnarends, Phys. Rev. B 34 (1986) 5009.

16- I. Galanakis, J. Phys. Condens. Matter 14 (2002) 6329.

17- G.A. deWijs, R.A. de Groot, Phys. Rev. B 64 (2001) 20402.

18- D. Brown, M.D. Crapper, K.H. Bedwell, M.T. Butterfield, S.J. Guilfoyle, A.E.R. Malins, M. Petty, Phys. Rev. B 57 (1998) 1563.

19- S. Plogmann, T. Schlatholter, J. Braun, M. Neumann, Yu.M. Yarmoshenko, M.V. Yablonskikh, E.I. Shreder, E.Z. Kurmaev, A. Wrona, A. Slebarski, Phys. Rev. B 60 (1999) 6428.

20- L. Charron, D. Dumchenko, E. Fortin, C. Gherman, L. Kulyuk Journal of Luminescence 112 (2005) 45.

21- Gaojun An, Liu Chenguang, Yuandong Hou, Xiaoling Zhang, Yunqi Liu Materials Letters 62 (2008) 2643.

22- Ming-Zhe Xue, Zheng-Wen Fu Electrochemistry Communications 8 (2006) 1855.

23- Kaye S. Savage, Daniela Stefan, Stephen W. Lehner Applied Geochemistry 23 (2008) 103.

24- E. Coronado, J.R. Galan-Mascaros, C.J. Gomez-Garcia and V. Laukhin: Nature 408, (2000) 470

25- W. Bensch, T. Bredow, H. Ebert, P. Heitjans, S. Indris, S. Mankovsky, M. Wilkening Progress in Solid State Chemistry 37 (2009) 206.

Chapter 01

LITERATURE SURVEY

1. HEUSLER ALLOYS

The Heusler alloys have been the subject of many investigations ever, since the discovery by Heusler [1] that some alloys of copper-manganese bronze and B subgroup elements, such as tin, were ferromagnetic although the constituents were themselves non ferromagnetic. These alloys are a superstructure, at the stoichiometric composition X_2YZ, named after its original discoverer and which are now defined as ternary intermetallic compounds. The first Heusler alloys studied were crystallizing in the $L2_1$ structure which consists of 4 fcc sublattices. Afterwards, it was discovered that it is possible to leave one of the four sublattices unoccupied to form the Cl_b. structure. Later, Bradley and Rodgers investigated an alloy near the composition Cu_2InAl which was ferromagnetic when quenched, but practically nonmagnetic when slow-cooled and were able to show that the changes in magnetic properties were related to an almost complete change in chemical structure. In 1983 De Groot et al.[2] predicted some of the X_2YZ type Heusler alloys, where X is a high valent transition metal atom, Y is a low valent transition metal atom, and Z is an *sp* element, to be half-metallic. These classes share simultaneously the property of an energy gap between valence and conduction bands for electrons of one spin polarization and the property of continuous bands for the electrons of the other spin polarization. This asymmetric band character reflects the character of the $C1_b$ structure itself; the minority spin electrons are semiconducting while the majority-spin electrons keep their normal metallic character. As a consequence, we have the remarkable situation here that the conduction electrons at the Fermi level are 100% spin polarized.

Moreover, these compounds are structurally matching with substrate materials and have a crystal structure compatible with the industrially used zinc blend semiconductors and possess a high Curie temperature to allow the applications in the devices operating at room temperature. Consequently, and due to these properties which have been confirmed experimentally, Heusler alloys are promising materials for technological applications [3-13] and become one of the major research interests in the spintronics community as key materials to develop spin polarized current sources for spintronics devices due to the possibility to study in the same family of alloys a series of interesting diverse magnetic phenomena like itinerant and localized magnetism, antiferromagnetism, helimagnetism, Pauli paramagnetism or heavy-fermionic behavior. The half-metallicity of a Heusler alloy was most convincingly demonstrated by the high tunneling magnetoresistance (TMR) value [14]

1.1 CRYSTALLINE STRUCTURE AND COMPOSITION

A comprehensive crystallographic investigation of the structure of this alloy has been carried out by Bradley and Rodgers on Cu_2MnAl [15]. The Heusler alloys are generally ternary alloys of stoichiometric composition bearing the general formula, X_2YZ which have the $L2_1$, structure (Fig. 1.1). In this class of alloys, X and Y are transition elements like Ni, Co, Pd, Pt, Fe,…etc and Z is an *sp*-element like Si, Al, Ge,….etc. Although the elements X, Y, and Z, when combined, may form a single phase structure but there are in principle several ways of distributing the atoms amongst the four sublattices, where in all cases the chemical order is preserved. The non-metal Z-coordination of X and Y are of tetrahedral and octahedral types, respectively, with the shortest metal–metal distances not so much expanded in comparison with those existing in the pure metals. More generally, these elements can be denoted by *A, B, C* and *D* giving an alloy of the formula *ABCD*. The unit cell (Fig. 1.1) is comprised of four interpenetrating free sublattices *A, B, C* and *D* with origins at (0 0 0), (l/4 l/4 l/4), (l/2 l/2 l/2) and (¾ ¾ ¾). Since these structures are verified experimentally [16].

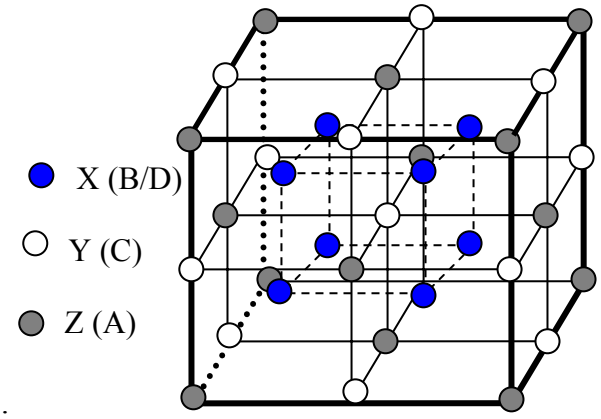

Figure 1.1 The atom position in Heusler alloys ($L2_1$ structure).

Furthermore, the Heusler alloys are structurally similar to the zinc blende lattice as shown in figure 1.2. Zinc blende structures, being composed of two interpenetrating face centered cubic *fcc* sublattices, have a considerable volume of open space. Heusler alloys fill up these voids with additional *fcc* sublattice. The so called half-Heusler alloys, such as XYZ, contain three *fcc* sublattices. While the full Heusler alloys, such as X_2YZ, where X≡(B,D), Y≡C and Z≡A, contain four *fcc* sublattices which fill up the voids (figure 1.3). In addition to the structural similarity of Heusler alloys with zincblende structure, some of them have similar lattice constants. This makes them good candidates for synthesizing single epitaxial layers. Moreover, several Heusler alloys have been grown on the zinc blende structure [17].

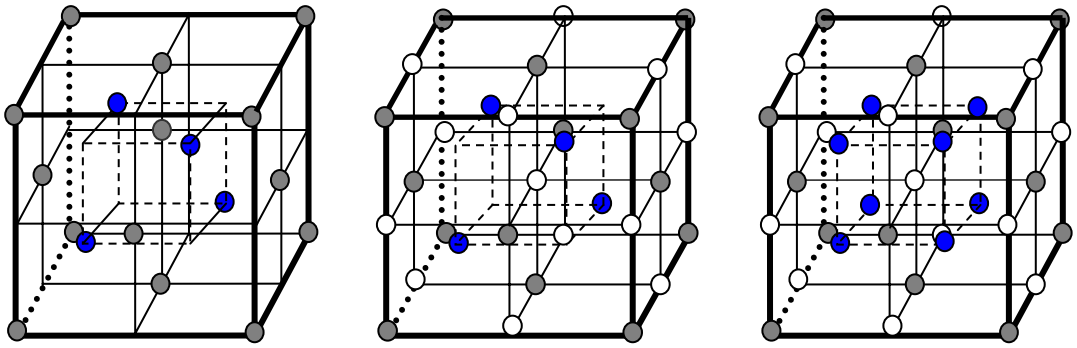

Zinc blende
XY

Half-Heusler
XYZ

Full-Heusler
X_2YZ

Figure 1.2 The different ways of filling the four sublattices in the Zinc blende structure, half-Heusler and full-Heusler alloys

In addition, there are seven well-known principal possible ordered structures, formed from four interpenetrating *fcc* sub-lattices *A, B, C* and *D*. figure 1.4 show the principal ordered structures; A_2: All lattices identically filled; B_2: A filled as C, B filled as D; B_{32}: A filled as B, C filled as D; L_2: B filled as D; $D0_3$,: B, C, and D identically filled; *C1*: A filled as C, D void; Cl_b: D void. In this later, i.e., half Heusler alloys, very different types of behaviour were observed, from semiconductor to metal from constant paramagnetism to Curie-Weiss behaviour, from weak ferromagnet to strong half metallic ferromagnet. Since adding three metals can be give rise to a semiconducting compound when the valence electron concentration by formula (EC) is 18. Adding (subtracting) one electron on (from) one crystallographic site gives rise to a metal.

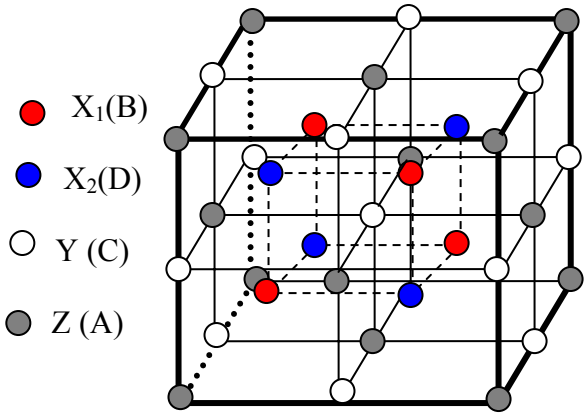

Figure 1.3 The four sublatices in the Heusler alloys ($L2_1$ structure).

Although it is not often possible uniquely to determine the proportion of each element on each of the four sub-lattices, an indication of the existing order may be deduced from the

measurement of X-ray and neutron structure factors. The extent to which the sites as a whole are filled, or have vacancies, can be ascertained from accurate measurements of the density of the alloy. In another way several Heusler systems exhibit a martensitic phase transition, including Ni_2MnGa [18].

1.2 ORDER-DISORDER PROCESS

The phenomenon of the ordering of atoms in alloys has been well known for a long time and it has been investigated experimentally as well as theoretically [19-22]. Its essence may be defined most generally as the differentiation of the occupation probabilities of various lattice points by atoms of various alloying components. Thus, a crystal of an alloy is in the state of order of atoms if such differentiation occurs. It is often connected with the division of the crystalline lattice into sublattices. In such a situation there may occur a difference between the occupation probabilities of the lattice points of various sublattices by atoms of various elements. The state of atomic disorder occurs in a crystal if all lattice points are occupied randomly by all kinds of atoms. The process of the ordering of atoms in an alloy is a complicate phenomenon and its detailed description is very difficult and complicated.

A general theory of order in the ternary alloys has been given by Wojciechowski [23,24]. It is consider the whole crystal, divide the crystalline lattice into sublattices and investigate the possibilities of the occupation of their lattice points by various kinds of atoms. In the more general case of these alloys there are considerable ways of arranging the atoms in these sublattices.

Owing to the infinite possibilities for the ordering of alloys of the X_2YZ type Pauly et *al.* (1968) chose to consider initially only these arrangements in which each superlattice is filled either solely by one element or by equal amounts of two elements. In effect, the 13 such ordering possibilities which they found sample ordering space at discrete points, namely those points at which the occupation parameters have the discrete values 0, ½ and 1. Although the elements X, Y, and Z, when combined, may form a single phase structure there is in principle an infinite number of ways of distributing the atoms amongst the four sub lattices. In another way, some Heusler structure is formed essentially from the ordered combination of two binary B_2 compounds *XY* and *XZ*, each of which may have the CsCl structure, for example CoTi and CoAl yields Co_2TiAl. Thus the possibility of forming a new Heusler alloy may be indicated by the ability of the components to form the B_2 structure.

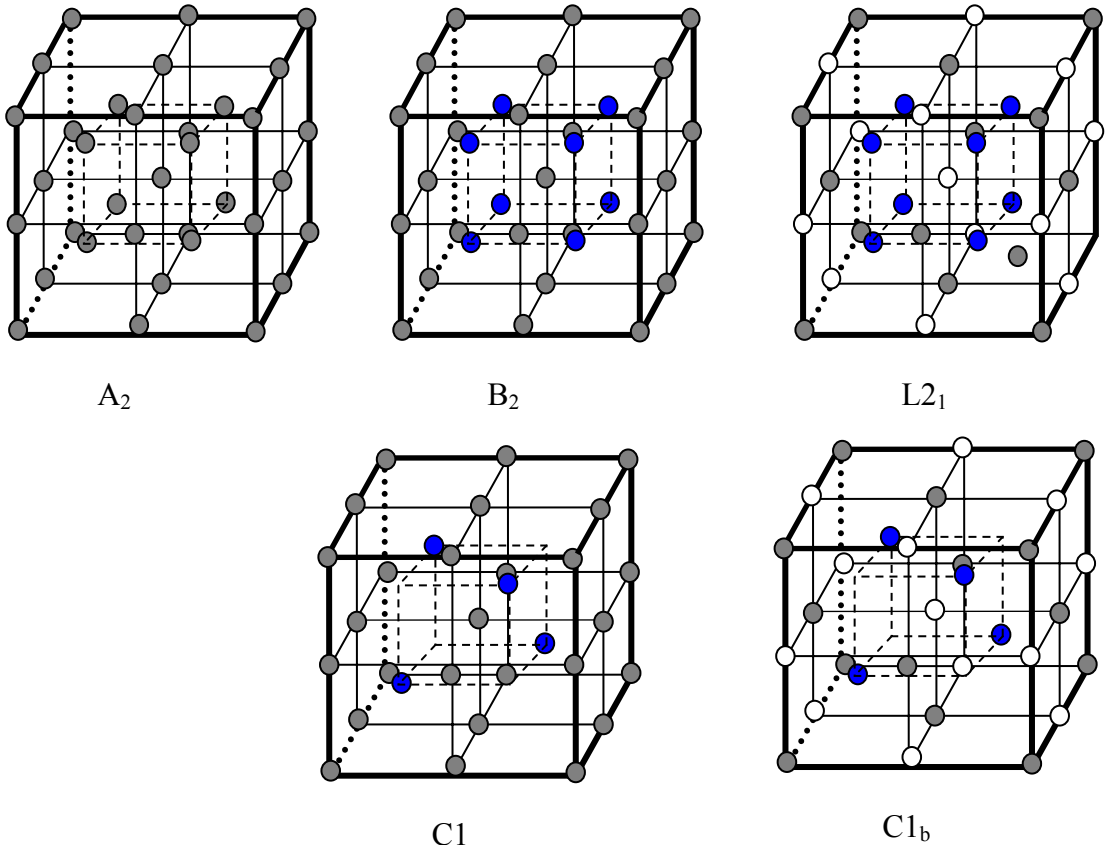

Figure 1.4 The principal ordered structures in Heusler alloys.

The effects of the temperature on the processes order-disorder of atoms in the some Heusler alloys have been investigated in which the $L2_1 \rightarrow B_2 \rightarrow A_2$ type of disorder is prevalent. The critical temperatures for $A_2 \rightarrow B_2$ and $B_2 \rightarrow L2_1$ order have been obtained from measurements of relative intensities of superlattice reflections [25] and the results have been analysed using a Bragg-Williams model for order-disorder transitions assuming a Lennard-Jones pair potential [26]. These studies indicated that the transitions proceed according to the following scheme: $L2_1 \rightarrow B_2 \rightarrow A_2$, i.e. two transitions occur: from the structure $L2_1$ to B_2 and from the structure B_2 to A_2 but the possibility of one stage of the process $L2_1 \rightarrow A_2$ was excluded.

Moreover we can recapitulate the transition from the ordered to the most prominent disordered structures as will be explained in the following: If the Y and the Z atoms are evenly distributed, the 4*a* and 4*b* positions become equivalent. This leads to a CsCl-like structure, also known as B_2-type disorder. The symmetry is reduced and the resulting space group is $Pm\bar{3}m$. The random distribution of the X and the Y or the X and the Z atoms results in the BiF_3-type disorder (Space group no. 216: $Fm\bar{3}m$, DO_3). The NaTl-type structure is

observed very rarely. In this structure type the X-atoms, which occupy one fcc sub-lattice, are mixed with the *Y* atoms, whereas the X-atoms on the other sub-lattice are mixed with the Z atoms. This kind of disorder is also known as B_{32} a disorder (Space group no. 227, $Fd\bar{3}m$). The X-atoms are placed at the Wyckoff position 8*a* (0, 0, 0), the Y and Z randomly distributed at position 8b (1/2, 1/2, 1/2). In contrast to these partial disorder phenomena all positions become equivalent in the tungsten-type structure with a bcc lattice and reduced symmetry $Im\bar{3}m$ (A_2).

1.3 SPIN POLARIZATION AND HALF METALICITY

For both scientific and technological reasons it is useful to define the electron spin polarization at Fermi energy of a material, although it is difficult to measure it and must be calculated from an indirect measurement [27]. The spin polarization at E_F is given by

$$P = \frac{\rho_{\uparrow}(\varepsilon_F) - \rho_{\downarrow}(\varepsilon_F)}{\rho_{\uparrow}(\varepsilon_F) + \rho_{\downarrow}(\varepsilon_F)}$$

where $\rho\uparrow(\varepsilon_F)$ and $\rho\downarrow(\varepsilon_F)$ are the spin dependent density of states at the ε_F . The arrows ↑, and ↓, assign states of opposite spin that are majority and minority states, respectively. *P* vanishes for paramagnetic or in anti-ferromagnetic materials even below the magnetic transition temperature. However, it has a finite value in ferromagnetic or ferrimagnetic materials below the Curie temperature. The electrons at ε_F are fully spin polarized (*P*=100%) when either $\rho\uparrow(\varepsilon_F)$ or $\rho\downarrow(\varepsilon_F)$ equals zero. A magnetic material in this case is labelled as "half-metallic" since one spin band exhibits metallic behavior while the other spin band acts as a semiconductor but most importantly both bands exist in a single material. Simply, half-metallic ferromagnets are materials that possess conduction electrons being 100% spin polarized at the Fermi energy.

1.4 HALF METALLIC HEUSLER ALLOYS

There are many ferromagnetic materials that are predicted to be half metallic like the CrO_2, Fe_3O_4,…etc [28]. Of these materials, the oxides require considerable effort to fabricate in thin film form. Furthermore some binary compounds have a Curie temperature around room temperature, making it difficult to realize the use of these materials in a thermally stable device application [29,30]. In contrast to the Heusler alloys which prove that it very preferment half metallic material with a height Curie temperature. Since, as we notice before, several combinations of elements occupying the X, Y, and Z sites are possible and in all cases chemical order is preserved. For the Y-element Heusler alloys usually contain Mn, the X element, for example, can be X=Fe, Co, Ni, Cu, Pd, or Rh and Z a pnictide or stannide ion

(Sb,Sn) or *sp* in general case. Mn-based Heusler alloys, where the Manganese considered one of the strangest of the 3d metals and has many features that are not well understood, have been found at most in a ferromagnetic ground state. They offer the unique possibility to study manganese compounds where the Mn atom has only other transition X metals as nearest neighbours ($L2_1$) and non transition Z elements group III-V in the second coordination sphere. Webster et al.[31,32], have investigated the crystal structure of these alloys in detail. In addition a variety of mutual substitutions of atoms in the corresponding sublattices has been studied by the same authors. Furthermore, it has been shown that some disorder [33] is often appearing in Mn-based Heusler alloys and that in total up to 10% of the Mn atoms change places with elements from a different sublattice. Nevertheless, the neighbourhood of Mn atoms is mainly built by X and Z elements. Mn-based Heusler alloys have a magnetic moment of about $2.5\mu_B$–$4.4\mu_B$ localized at the Mn site. Traditionally they are considered as ideal systems with local magnetic moments and many compounds are known experimentally to be ferromagnets with high Curie temperatures ranging between 500 and 700K such as for the Co, Ni, Pd, and Pt compounds.

1.5 THE MAGNETO-OPTICAL EFFECTS

M. Faraday [34] and J. Kerr [35] were the first to study the influence of magnetized media on the polarization of transmitted and reflected light respectively. When linearly polarized light is transmitted through a magnetized medium, the polarization of the transmitted light rotates by an angle θ. This is named the Magneto-Optic Faraday Effect (MOFE); when linearly polarized light is reflected from the surface of a magnetized medium, the reflected light becomes elliptically polarized with a rotation of the polarization plane. This rotation can be understood in term of a difference of the refractive indices for the left and right circularly polarized components, produced by the interaction of light with the magnetic field, since a linearly polarized beam of light can be decomposed into a sum of left and right circularly polarized light. These two magneto-optic effects are due to the interaction between light and the magnetized medium, and give the information on

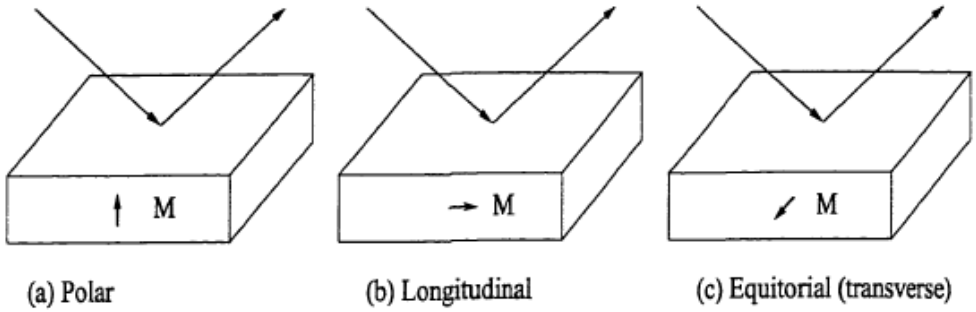

Figure 1.5 Geometry for longitudinal, equatorial and polar Kerr effects

the electronic and magnetic structure of the medium. For metallic systems magneto-optical studies made by means of the Kerr effect have a certain number of advantages relative to studies by means of the Faraday Effect. This latter effect can be studied only on sufficiently thin films.

Depending on the orientation of the magnetization vector relative to the sample surface, the Kerr effect can be classified into three types: longitudinal (meridional), and transverse (equatorial) effects and polar Kerr effects. The three geometries relevant to the Kerr effect are illustrated in Figure (1.5);

1) Polar MOKE (see Fig. 1.5(a)): the magnetization direction is perpendicular to the surface of the medium and parallel to the plane of incidence;

2) Longitudinal MOKE (see Fig. 1.5(b)): the magnetization is parallel to the surface of the medium and parallel to the plane of light incidence;

3) 'Transverse MOKE (see Fig. 1.5(c)): the magnetization lies in the surface of the medium and is normal to the plane of incidence.

For the rest of this thesis, it will be referred to as just the "Kerr effect". The polar Kerr effect can conveniently be described in terms of the dielectric tensor (or conductivity tensor) [36]. In materials for which the net magnetization M is aligned parallel to an axis of three-fold or higher-symmetry, the dielectric tensor can be written as

$$\epsilon = \begin{pmatrix} \epsilon_{xx} & \epsilon_{xy} & 0 \\ -\epsilon_{xy} & \epsilon_{yy} & 0 \\ 0 & 0 & \epsilon_{zz} \end{pmatrix}$$

Here the magnetization direction is parallel to the z direction. The off-diagonal terms represent the magneto-optical Kerr effect contribution to ε. The diagonal components have an

even powered dependence on the magnetization. The various elements $\varepsilon_{\alpha\beta}$ are composed of real and imaginary parts, which may be represented by the relations

$\varepsilon_{\alpha\beta}=\varepsilon^{1}_{\alpha\beta}+i\varepsilon^{2}_{\alpha\beta}$

where α, β≡x,y,z, $\varepsilon_{xx}=(n+ik)^2$, n and k are refractive index and extinction coefficient, respectively. The optical conductivity tensor $\sigma_{\alpha\beta}=\sigma^{1}_{\alpha\beta}+i\sigma^{2}_{\alpha\beta}$ is related to the dielectric tensor $\varepsilon_{\alpha\beta}$ through the equation

$$\varepsilon_{\alpha\beta}=\delta_{\alpha\beta}+\frac{4\pi i}{\omega}\sigma_{\alpha\beta}(\omega)$$

where δ is the Kronecker's symbol.

A complete description of MO effects in this formalism is given by the four non-zero elements of the dielectric tensor or, equivalently, by the complex refractive index N(ω) where the refractive indices are related to the dielectric tensor elements by:

$$n_{\pm}=\sqrt{\varepsilon_{xx}\pm i\varepsilon_{xy}}$$

$$=\sqrt{\varepsilon_{xx}}\sqrt{1\pm i\frac{\varepsilon_{xy}}{\varepsilon_{xx}}}$$

$$\approx\sqrt{\varepsilon_{xx}}\left(1\pm i\frac{1}{2}\frac{\varepsilon_{xy}}{\varepsilon_{xx}}\right)$$

So we have $n_{-}-n_{+}=-i\frac{\varepsilon_{xy}}{\varepsilon_{xx}}$ and $n_{+}n_{-}=\left(1+\frac{1}{4}\left(\frac{\varepsilon_{xy}}{\varepsilon_{xx}}\right)^2\right)\varepsilon_{xx}$, since $\left(\frac{\varepsilon_{xy}}{\varepsilon_{xx}}\right)^2$ ππ 1.

With this approximation and in terms of the conductivity ($\varepsilon_{xx}=1+i\frac{4\pi\sigma_{xx}}{\omega}$ and $\varepsilon_{xy}=1+i\frac{4\pi\sigma_{xy}}{\omega}$) the complex Kerr angle, ϕ, is given by[37]: $\varphi=\theta_k+i\varepsilon_k=\frac{-\sigma_{xy}}{\sigma_{xx}\sqrt{1+i\frac{4\pi\sigma_{xx}}{\omega}}}$,

the real part θ_k is the rotation of polarization plane while the imaginary part ε_k gives the ellipticity of the reflected light.

2. TRANSITION-METAL CHALCOGENIDES

Transition-metal chalcogenides, in terms of composition, provide a wide variety of compounds which crystallize in the pyrite structure [38], in its ternary ordered versions (cobaltite, ullmannite) [39], and in the marcasite and distorted marcasite (arsenopyrite) one [40]. These layer-type materials, with their interesting quasi-two dimensional structures, can be used as a substrate for other materials [41] and for the formation of intercalated complexes with foreign atoms or molecules, organic or inorganic, between the layers offering the possibility of combining different properties in a single material [42]. These compounds have attracted considerable attention for their magnetic [43] and optical properties [44,45]. They have shown a wide applicability in many technologically important areas such as hydrodesulfurization catalysts [46], solid state lubricant [47] and photoactive materials [48].

2.1 CRYSTALLINE STRUCTURE AND COMPOSITION

The transition metal dichalcogenides compounds form a structurally and chemically well-defined family and about two-third of this family assume layer structures. The basic structure of loosely coupled *Ch-TM-Ch* sheets makes such materials extremely interesting. Within a layer, the bonds are strong, while between adjacent layers they are remarkably weak.

The crystal structures of the layered chalcogenides of formal stoichiometry $TMCh_2$ (TM=metal, Ch=chalcogen) are shown in Figure 1.6. They are characterized by two-dimensional sandwich units of *Ch-TM-Ch* atomic layers along the crystallographic a-axis (the chalcogenides are close-packed). Along the crystallographic c-direction the sandwich units are separated from each other by the so-called van der Waals gap. The close-packed and chemically saturated chalcogenide atoms form the inner surfaces. The bonding interaction within the sandwich units is very strong and is based on covalent bonds with some ionic contribution depending on the ionicity of the *TM-Ch* bonds.

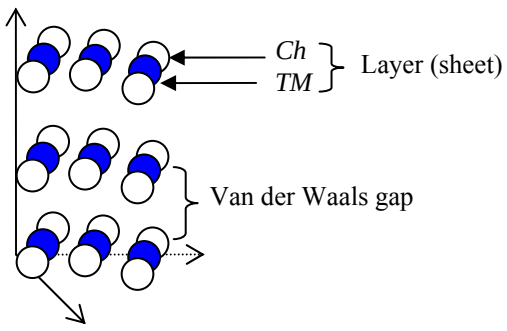

Figure 1.6 The crystal structures of the layered transition metal chalcogenides

The *$TMCh_2$* structures fall into two classes: layered and non-layered; the non-layered members are found in groups VII and VIII; they are $MnCh_2$. $FeCh_2$, $RuCh_2$. $OsCh_2$, $CoCh_2$, $RhCh_2$, IrS_2, $IrSe_2$, NiS_2 and $NiSe_2$, The ditellurides of Co and Rh can also adopt a CdI_2-type of structure, the others occur in one or more of the following structure types: pyrite, marcasite, $IrSe_2$ and the PdS_2-type.

In many cases the same compound forms different phases (polytypes) which may deviate from each other by a different metal coordination and/or by a different stacking of the sandwich units. The polytypes are labeled according to the number of repeating units along the c axis (normal to the layer) In which the compound formula is preceded by a number denoting how many slabs are in the unit cell and a capital letter giving the overall symmetry of the structure (T: trigonal. H: hexagonal, R: rhombohedral), for example 2H-MoS_2 and 2R-MoS_2. Small Letters distinguish between different stacking sequences in the same structural family.

Depending on the relative orientation of the sheets, two different coordinations are obtained around each metal ion, one approximately octahedral where the metal atom is surrounded octahedrally by the chalcogen and another where the metal atom is surrounded in a trigonal prismatic which found in the MoS_2-type of structure. Both of these are shown in Figure 1.7, The metals are found in a trigonal prismatic coordination for more covalent bound chalcogenides to optimize the covalent overlap, whereas more ionic compounds prefer octahedral coordination minimizing the electrostatic repulsion. Although a mixture of the two is sometimes found, whereas the 'mixtures' contain alternatingly prismatic and octahedral coordinated layers.

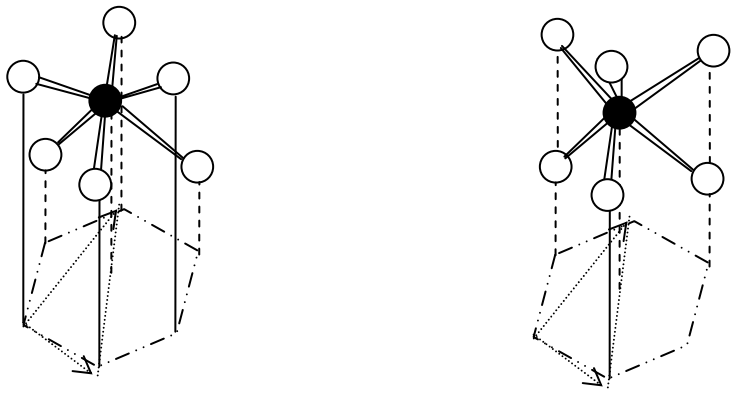

Figure 1.7 The different coordinations around each metal ion.

2.2 PREFERRED STRUCTURE

The three-dimensional framework structure of the transition metal chalcogenides compounds is converted first into a slab structure and then into a sheet structure due to the population of d orbital, the main d-electron configurations that we consider. The first cases are d^0, d^5-high spin, and d^{10} ions, such as V^{5+} (d^0) high-spin Fe^{+3}(d^5), and Cu^+ and Zn^{+2} (both d^{10}). These three configurations give symmetrical noble-gas-like cations that prefer the highly symmetric coordination of a tetrahedron of anions.

ZnS occurs as sphalerite or wurtzite, both of which have tetrahedral coordination of the Zn^{2+} (d^{10}) ion. Zn, Cd. and Hg all occur in at least one polymorph of their mono-sulphides with tetrahedral metal coordination; Fe^{3+} is almost always tetrahedrally coordinated in its sulphides. Cu^+ is often found in tetrahedral holes of a sulphur lattice, but it sometimes displays more complicated coordination, as does Ag^+.

Other configurations are d^3, d^6-low spin, and d^8. For octahedral coordination geometry, these three cases will give evenly filled orbitals, and thereby allow for undistorted ligand environments. Examples include Cr_2S_3, which is derived from the NiAs structure and has an octahedral surrounding for the d^3; Cr^{3+} ions; pyrite, FeS_2 which also has an octahedral environment for the d6 Fe^{2+} ions; and high-temperature NiS, which again has octahedral metal coordination for the (high-spin) d^8 Ni^{2+} ion. Because these metal ions have evenly filled t_{2g} or e_g orbitals, their compounds are all semiconducting.

d^8 configurations can also give rise to square-planar coordination geometry, as in cooperate (PtS), PdS, and PdS_2 [49]. Square-planar ligand fields result in a four below-one splitting of the d-orbitals, so all the d-electrons are paired and relatively low in energy for a fit ling of eight electrons. The rationale for why nickel does not resemble its congeners in assuming this geometry is that the pairing energy is too high; it prefers the high-spin configuration allowed by the eg orbitals of an octahedral ligand field. Whereas octahedral coordination is the most popular geometry for six coordinations, a few important sulphides instead have trigonal-prismatic coordination. This occurs only for low d-electron count (d^1 to d^2), and is found in, for example, NbS_2 (d^l) and MoS_2 (d^2).

A1though there is a relationship between the different binary and ternary transition metal chalcogenide structures, only a few are unique; most of the others can be viewed as derivatives of these classified derivative structures as occurring by four main mechanisms:

i) Substitution of one atom for another;

ii) Ordered omission of atoms;

iii) Addition of atoms to previously unoccupied sites; and distortion of an array.

2.3 INTERCALATION

particularly important of these material is the discoveries, the so-called intercalation, that many atoms and molecules can be inserted between the adjacent layers, thus forming intercalation compounds, due to the weak interlayer forces which allowed extra ions and even fairly large organic molecules inside. Since, recently, much interest has focused on the inorganic organic hybrid compounds because this offers perspectives for the realization of molecular-based materials, especially those that can combine different properties such as metal-like conductivity and bulk ferromagnetic property in a single material [50]. Intercalation of organic species into layered inorganic solids represents one of the useful approaches to create the ordered molecular-based materials with some novel properties [51].

REFERENCE

1- F. Heusler, Verh. Dtsch. Phys. Ges. 5, (1903) 219

2- R.A. de Groot, F.M. Mueller, P.G. van Engen, K.H.J. Buschow, Phys. Rev. Lett. 50 (1983) 2024.

3- J. Q. Xie, J. W. Dong, J. Lu, C. J. Palmstrøm, and S. McKernan, Appl. Phys. Lett. 79, (2001) 1003.

4- M. Kurfiss and R. Anton, J. Alloy. Compd. 361, (2003) 17

5- M. N. Kirillova, A. A. Makhnev, E. I. Shreder, V. P. Dyakina, and N. B. Gorina, Phys. Stat. Solidi B 187, (1995) 231

6- K. E. H. M. Hanssen and P. E. Mijnarends, Phys. Rev. B 34, (1986) 5009.

7- K. E. H. M. Hanssen, P. E. Mijnarends, L. P. L. M. Rabou, and K. H. J. Buschow, Phys. Rev. B. 42, (1990) 1533.

8- S. Kämmerer, A. Thomas, A. Hütten, and G. Reiss, Appl. Phys. Lett. 85, (2004) 79.

9- S. Okamura, R. Goto, S. Sugimoto and K. Inomata, J. Appl. Phys. 96, (2004) 6561.

10- E. Girgis, P. Bach, C. Rüster, C. Gould, G. Schmidt, and L. W.Molenkamp, Appl. Phys. Lett. 86, (2005) 142503.

11- B. Balke, G. H. Fecher, H. C. Kandpal, C. Felser, K. Kobayashi, E. Ikenaga, J.-J. Kim, and S. Ueda, Phys. Rev. B 74, (2006) 104405.

12- H. C. Kandpal, G. H. Fecher and G. Schönhense, Phys. Rev. B 73, (2006) 094422.

13- S. Wurmehl, G. H. Fecher, H. C. Kandpal, V. Ksenofontov, C. Felser, and H. J. Lin, Appl. Phys. Lett. 88, (2006) 032503.

14- Y. Sakuraba, M. Hattori, M. Oogane, Y. Ando, H. Kato, A. Sakuma, T.Miyazaki, and H. Kubota, Appl. Phys. Lett. 88, (2006) 192508.

15- A. J. Bradley and J.W. Rodgers, Proc Roy Soc A144, (1934) 340.

16- G.P. Felcher, J. W. Cable and M.K. Wilkinson, J. Phys. Chem Solids 24, (1963) 1663

17- W. H. Wang, M. Przybylsh, W. Kuch, L. I. Chelaru, J. Wang, Y. F. Lu Barthel H. L Meyer Hein and J. Kirschner Phys. Rev. B 71 (2005) 144416

18- R. D. James and M. Wuttig, Phil. Mag. A. 77, (1998) 1273

19- E. Jr. F. Jaumot and H. S. Charles Acta Metall. 2, (1954) 63.

20- J. Soltys, phys. stat. sol. (a) 63, (1981) 401

21- S.H. Wei, L. G. Ferreira, James E. Bernard, and A. Zunger, Phys. Rev. B 42 (1990) 9622.

22- R.P. McCormack, D. de Fontaine, and J.J. Hoyt J. Phas. Equi. 18, (1995) 580.

23- K. F. Wojciechowskit, Act. Metal. 6, (1958) 396

24- K. F. Wojciechowskit, Act. Metal. 7 (1959) 376

25- J. Soltys, phys. stat. sol. (a) 66, (1981) 485.

26- J. Soltys, R. Kozubski, Phys. Stat. Sol. (a) 63, (1981) 35.

27- R. J. Soulen Jr., J. M. Byers, M. S. Osofsky, B. Nadgorny, T. Ambrose, S. F. Cheng, P. R. Broussard, C. T. Tanaka, J. Nowak, J. S. Moodera, A. Barry, J. M. D. Coey, Science 282 (1998) 85.

28- W.H. Xie, Y.Q. Xu, B.G. Liu and G. Pettrifor, Phys. Rev. Lett. 91, (2003) 037204

29- K. Schwarz, J. Phys. F Met. Phys. 16, (1986) L211

30- Y.S. Dedkov, U. Rudiger, and G. Guntherodt: Phys. Rev. B 65, (2002) 64417

31- P. J. Webster, M. R. I. Ramadan, J. Magn. Magn. Mater. 5 (1977) 51

32- P.J. Webster and R.D. Tebble, J. Appl. Phys. 39 (1968) 471.

33- P. J. Webster and K. R. A. Ziebeck, in Alloys and Compounds of d-Elements with Main Group Elements. Part 2., edited by H. R. J. Wijn, Landolt-Boo¨rnstein, New Series, Group III, Vol. 19, Springer-Verlag, Berlin, pp. 75–184

34- M. Faraday, Phil. Trans. R. Soc. 136, (1846) 1

35- J. Kerr, Philos. Mag. 3 (1877) 321.

36- M. J. Freiser, IEEE Trans. Magn., MAG-4, (1968) 152.

37- V. Antonov, B. Harmon, and A. Yaresko, *Electronic Structure and Magneto-Optical Properties of Solids* (Kluwer Academic, Dordrecht, 2004).

38- D.W. Bullett, J. Phys. C: Solid State Phys. 15, (1982) 6163.

39- A.J. Foecker, W. Jeitschko, J. Solid State Chem. 162, (2001) 69.

40- S.L. Harmer, H.W. Nesbitt, Surf. Sci. 564, (2004) 38

41- A. Yamada, K.P. Ho, T. Maruyama, K. Akimoto, Appl. Phys. A 69, (1999) 89

42- R. Brec, G. Ouvrard, A. Louisy, J. Rouxel, Solid State Ion. 101-103, (1997) 9.

43- A. Olivas, I. Villalpando and O. Pérez, S. Fuentes, Mater. Lett. 61, (2007) 4336.

44- D. Dumcenco, Y.S. Huang, C.H. Liang, K.K. Tiong, J. Appl. Phys. 104, (2008) 063501.

45- D. Dumcenco, Y.S. Huang, J. Appl. Phys. 102, (2007) 083523

46- S.E. Skrabalak, k.S. Suslick, J. Am. Chem. Soc. 127, (2005) 9990

47- T.W. Scharf, S.V. Prasad, M.T. Dugger, P.G. Kotula, R.S. Goeke, R.K. Grubbs, Acta Mater. 54, (2006) 4731.

48- C. Ballif, M. Regula, F. levy, Sol. Energy. Mater. Sol. Cells 57, (1999) 189

49- A. Hamidani, B. Bennecer, K. Zanat, J. Phys. Chem. Solids 71, (2010) 42

50- E. Coronado, J.R. Galan-Mascaros, C.J. Gomez-Garcia and V. Laukhin: Nature, 408, (2000) 470.

51- R. Chollhorn, Chem. Mater. 8, (1996) 1747.

Chapter 02

THEORETICAL BACKGROUND

2.1 INTRODUCTION

A solid can be described as a many-atom system composed of electrons and nuclei which are interacting with each other. An exact mathematical treatment of the Schrödinger equation of this many-body-system is highly complex and virtually impossible. Nevertheless, suitable methods to derive a wide range of physical properties of material are available. In order to study many atom problems with moderate computational effort a range of approximations is introduced. We can cite the approximation which is called Born Oppenheimer (or adiabatic) approximation [1], which separate the calculation of the electronic structure from the ionic motion. The Hartree-Fock approximation [2,3] which provides an approximate solution to the many-body problem and uses a single Slater determinant to express the many electron wave functions. The so-called Hartree-Fock equation which has to be solved includes a Coulomb term (or Hartree term) and an exchange term (or Fock term), which arises from the antisymmetry of the wave function with respect to two-particle permutation, due to Pauli's exclusion principle. The effects of electron correlation, beyond that of exchange energy are completely neglected in this method. In contrast to the other methods, the Density Functional Theory (DFT) [4] provides an exact solution of the many-body problem. Furthermore, this method is proved to be a powerful way to determine the ground state energy of atoms, molecules, and extended systems with reducing the many-body-problem of interacting particles to a single-particle problem. An important part of the theory requires one to determine the kinetic energy of ground state of a system of N no interacting electrons in a general external field. Kohn and Sham [5] showed how this can be numerically calculated very accurately using a set of N orbitals. However this prevents the simple linear scaling in N that would arise if the kinetic energy could be directly expressed as a functional of the electron density, as it is done with other components of the total energy like the exchange correlation energy.

2.2 DENSITY-FUNCTIONAL THEORY

2.2.1 THE HOHENBERG-KOHN THEOREMS

Density functional theory (DFT) considers the particle density to be the fundamental variable to describe the state of a system in an external potential. Historically, the density functional approach initiated with the idea that locally the behavior of a collection of particles, the electron cloud, could be represented and approximated by that of a free electron gas of the same density at that point. The Thomas Fermi (TF) model [6] was in many aspects very successful and showed the basic steps to obtain the density functional for the total energy:

using standard quantum mechanics based on wave functions to obtain from a well defined model a direct relationship, functional, between the total energy, E, and the density ρ(r). The fundament of this concept was derived by Hohenberg and Kohn [4]. They proved that the following theorem holds exactly:

a) There is a universal functional $F[\rho(r)]$ of the electron density distribution ρ(r), that defines the total energy of the electronic system, given by:

$$E = \int V(r)\rho(r)dr + F[\rho(r)] \qquad (2.1)$$

b) The total energy E has a minimum when the charge density ρ(r) coincides with the true charge density in the external potential v(r). This theorem is exact if the ground state has no degeneracy. Thus the Hohenberg-Kohn theorem states that the ground state energy E is a universal functional of the charge density and that the ground state charge density can be obtained by applying the variation principle to the energy. If we note the Hamiltonian of the system H, the functional of the ground state energy is given by:

$$E[\rho(r)] = \min_{\rho(r)} \langle \psi | H | \psi \rangle \qquad (2.2)$$

under the constraint, that the wave functions used for variation reproduce the charge density distribution ρ(r)

$$\rho(r) = \left\langle \psi \left| \sum_i \delta(r - r') \right| \psi \right\rangle, \qquad (2.3)$$

this leads to the relation

$$E[\rho(r)] \geq E[\rho_0(r)] = E_0 \qquad (2.4)$$

At this point the exact form of the total energy functional remains undetermined, however the scheme used to derive electronic ground state properties can already be outlined here. First of all one has to find a suitable approximation of $E[\rho_0(r)]$ and then apply the variation principle to the total energy functional

$$\delta E[\rho(r)] = 0 \qquad (2.5)$$

under the constraint, that the number of particles is conserved

$$\int \rho(r)dr = N \qquad (2.6)$$

2.3 *KOHN-SHAM EQUATIONS*

In 1965, Kohn and Sham [5] proposed the idea of replacing the kinetic energy of the interacting electrons with that of an equivalent non-interacting system, because the latter can

be easily calculated. In this case and if the ground state is non-degenerate, the ground state charge density can be expressed in terms of single particle orbitals ϕ_i

$$\rho(r) = \sum_{i=1}^{N} |\phi_i(r)|^2 \quad , \tag{2.7}$$

and the kinetic energy functional $T_s(\rho(r))$ for the system is,

$$\begin{aligned} T_s[\rho(r)] &= \langle \psi_i | \sum_{i=1}^{N} -\frac{1}{2}\nabla_i^2 | \psi_i \rangle \\ &= \sum_{i=1}^{N} \langle \psi_i | -\frac{1}{2}\nabla^2 | \psi_i \rangle \end{aligned} \tag{2.8}$$

The universal functional $F(\rho(r))$ can be rewritten as

$$\begin{aligned} F(\rho(r)) &= T(\rho(r)) + V_{ee}(\rho(r)) \\ &= T_s(\rho(r)) + C(\rho(r)) + [T(\rho(r)) - T_s(\rho(r)) + V_{ee}(\rho(r)) + C(\rho(r))] \\ &= T_s(\rho(r)) + C(\rho(r)) + E_{XC}(\rho(r)) \end{aligned} \tag{2.9}$$

where $C(\rho(r))$ represents the classical electron Coulomb interaction,

$$C(\rho(r)) = \frac{1}{2}\int \frac{\rho(r)\rho(r')}{|r - r'|} dr dr' \tag{2.10}$$

and $E_{XC}(\rho(r))$ is the so called exchange-correlation energy, this term consists of two parts. The first part comes from the correction of the kinetic energy from the non-interacting fictitious system. The other part comes from the non-classical effects of the electron-electron interactions.

By applying the variational principle, Kohn-Sham effective potential $V_{eff}(r)$ is defined as

$$\begin{aligned} V_{eff}(r) &= v(r) + \frac{\delta C[\rho]}{\delta \rho(r)} + \frac{\delta E_{XC}[\rho]}{\delta \rho(r)} \\ &= v(r) + \int \frac{\rho(r')}{|r - r'|} dr' + v_{xc}(r) \end{aligned} \tag{2.11}$$

In the above equation, v(r) is the external Coulomb potential due to the nuclei. The second term,

$$\frac{\delta C[\rho(r)]}{\delta \rho(r)} = \int \frac{\rho(r')}{|r - r'|} dr' \tag{2.12}$$

is the potential resulted from the electron-electron Coulomb repulsion. The last term represent the exchange and correlation potential V_{xc} which given by:

$$v_{xc}(r) = \frac{\delta E_{XC}[\rho]}{\delta \rho(r)} \tag{2.13}$$

Writing out the total energy functional within this approximation and applying the variational principle, one generates a set of N single electron equations known as the KS equations.

$$\left(-\frac{1}{2}\nabla^2 + v_{eff}(r)\right)\phi_i(r) = \varepsilon_i \phi_i(r) \tag{2.14}$$

with

$$\rho_0(r) = \sum_{i=1}^{N} |\phi_i(r)|^2 \tag{2.15}$$

$$E_0 = \sum \varepsilon_i + E_{xc}[\rho(r)] - \int v_{xc}(r)\rho(r)dr - \frac{1}{2}\int \frac{\rho_0(r)\rho_0(r')}{|r - r'|} drdr' \tag{2.16}$$

These equations can be solved exactly using self-consistent methods. Such knowledge of E_{xc} is unavailable however, so approximations must necessarily be made.

2.4 *SELF-CONSISTENT ITERATION*

To solve the Kahn-Sham equations self consistently we start with a guess potential, $V_{in}^{0}(r)$, By using some approximate form for the functional dependence of E_{xc} on density, we must compute V_{xc} as a function of r. The set of Kohn-Sham equations are then solved to obtain an initial set of Kahn-Sham orbital. This set of orbital is then used to compute an improved density from Eqn. (2.15). From this solution, a new initial potential is generated, $V_{in}^{(n+1)}$, so that the sequence of $V_{in}^{(n)}$ and $V_{out}^{(n+1)}$ converges to the self-consistent potential V_{scf}, which is defined as the potential for which $V_{in} = V_{out}$ and the process is repeated until the density and exchange correlation energy converge to within some tolerance as shown in figure 3.1. One way to give better solutions is to mix input and output potentials linearly:

$$V_{in}^{(n+1)} = (1-\beta)V_{in}^{n} + \beta V_{out}^{n} \tag{2.17}$$

where β is set between 0-1 (usually β=0.7-0.9 but must be reduced where convergence is difficult to achieve). Another way is to use Anderson method:

$$V_{in}^{(n+1)} = (1-\beta)\left[(1-\theta_n)V_{in}^{n} + \theta_n V_{in}^{(n-1)}\right] + \beta\left[(1-\theta_n)V_{out}^{(n)} + \theta_n V_{out}^{(n-1)}\right] \tag{2.18}$$

$$\theta_n = \left\| (1-\theta_n)\left(V_{in}^{(n)} - V_{out}^{(n)}\right) + \theta_n \left(V_{in}^{(n-1)}\right)\right\|^2 \tag{2.19}$$

This method is usually used to handle difficult calculation for complex system consists of many atoms in the unit cell.

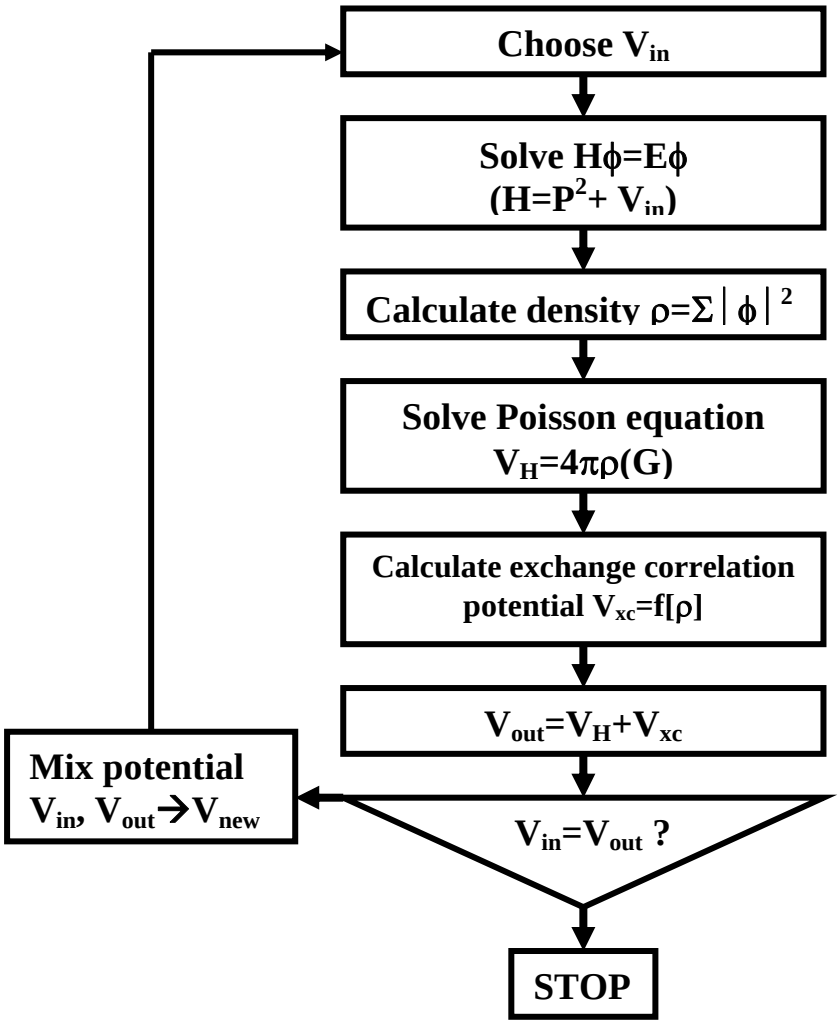

Figure 2.1 Steps of the self consistent calculation.

2.5 *LOCAL-DENSITY AND GENERALIZED GRADIENT APPROXIMATIONS*

The Kohn-Sham formulation of density functional theory is, to this point, still exact. All the complications arising from the many-body nature of the problem are contained in $E_{xc}[\rho(r)]$. The power of density functional theory is that approximate forms for E_{xc} are possible to construct which lead to an accurate description of real systems.

The most widely used and most simple approximation is the local density approximation (LDA). In their pioneering work Kohn and Sham pointed out that many solids are well approximated by a homogeneous electron gas, such that the exchange and correlation energy at *r* depends only on the electron density at r. They introduced the local density approximation that generalizes to the local spin density approximation (LSDA)

$$E_{xc}^{LSDA}\left[\rho(r)^{\uparrow},\rho(r)^{\downarrow}\right]=\int\rho(r)\varepsilon_{xc}^{\text{hom}}\left(\rho(r)^{\uparrow},\rho(r)^{\downarrow}\right)dr^{3} \qquad (2.20)$$

where ε^{hom}_{xc} is the spatially constant exchange-correlation density of the homogeneous gas. For unpolarized system, the LDA energy is given by the same formula with

$$\rho(r)^{\uparrow}=\rho(r)^{\downarrow}=\frac{\rho(r)}{2} \qquad (2.22)$$

The form of the potential is then given by

$$V_{xc}^{LDA}([\rho(r)])=\frac{\delta E_{xc}^{LDA}[\rho(r)]}{\delta\rho(r)}=\frac{\delta[\rho(r)\varepsilon_{xc}^{LDA}(r)]}{\delta\rho(r)} \qquad (2.21)$$

The simplest form of the LDA to the exchange-correlation potential has been proposed by Slater et al. [7], usually called X_α method, where V_{xc} becomes

$$V_{xc}(\rho)=-\left(\frac{3\alpha}{2}\right)\left(\frac{3\rho}{\pi}\right)^{\frac{1}{3}}$$

Other commonly used parameterization based on the results by Ceperley and Adler [9] has been proposed by Perdew and Zunger [10].

In addition, non local effects may be included by considering functionals that depend on the local gradient of the density in the exchange-correlation energy. This leads to a class of functionals known as “generalized gradient approximations” (GGA) [12,13].

The basic idea of GGA is to express the exchange-correlation energy in the following form

$$E_{xc}^{GGA}[\rho(r)]=\int\rho(r)\varepsilon_{xc}^{GGA}(\rho(r),\nabla\rho(r))dr \qquad (2.23)$$

2.6 LDA+U

The simulation of strongly correlated systems requires techniques beyond the LDA or GGA for this raison many researcher refine the LDA by introducing new scheme which so called ‘LDA+U’. The idea of this method is to include the Coulomb interaction between strongly localized d and f electrons in the spirit of a mean-field Hubbard model [14], whereas the interactions between the less localized s and p electrons are treated within the standard local spin density approximation. To achieve this, a Hubbard-like interaction term E_U, which depends on the occupation of the localized orbitals, is added to the LSDA total energy, and an additional double counting correction E_{dc} is introduced to subtract that part of the electron-electron interaction between the localized orbitals. In terms of this idea, we define the generalized LDA+U functional as follows:

$$E^{LDA+U}\left[\rho^{\sigma}(r),\{n^{\sigma}\}\right]=E^{LSDA}\left[\rho^{\sigma}(r)\right]+E^{U}\left[\{n^{\sigma}\}\right]-E_{dc}\left[\{n^{\sigma}\}\right] \qquad (2.24)$$

where $\rho^{\sigma}(r)$ is the charge density for spin-σ electrons and $E^{LSDA}\left[\rho^{\sigma}(r)\right]$ is the standard LSDA functional.

The Hubbard-like interaction term or the orbital polarizations are described by the mean-field (Hartree-Fock) type of theory:

$$E^{U}\left[\{n\}\right]=\frac{1}{2}\sum_{\{m\},\sigma}\left\{\begin{array}{l}\left\langle m,m^{''}\left|V_{ee}\right|m^{'},m^{'''}\right\rangle n^{\sigma}_{mm^{'}}n^{-\sigma}_{m^{''}m^{'''}}\\+\left(\left\langle m,m^{''}\left|V_{ee}\right|m^{'},m^{'''}\right\rangle-\left\langle m,m^{''}\left|V_{ee}\right|m^{'''},m^{''}\right\rangle\right)n^{\sigma}_{mm^{'}}n^{\sigma}_{m^{''}m^{'''}}\end{array}\right\} \quad (2.25)$$

where V_{ee} are the screened Coulomb interactions among the *nl* electrons. m and σ designate the orbital and spin, respectively. The last term in Eq. (2.25) corrects for double counting part E_{dc} which is diagonal in spin and it given by

$$E_{dc}=\frac{U}{2}n(n-\eta)-\frac{J}{2}\sum_{\sigma=\uparrow,\downarrow}n^{\sigma}\left(n^{\sigma}-\eta_{\sigma}\right) \quad (2.26)$$

$$n^{\sigma}=\sum_{m=-l}^{l}n^{\sigma\sigma}_{mm};\quad n=n^{\uparrow}+n^{\downarrow};\ \eta=\frac{1}{2}\left(\eta_{\uparrow}+\eta_{\downarrow}\right) \quad (2.27)$$

where U and J are screened Coulomb and exchange parameters [15]and η_{σ}=1 in the fully localized limit [16] while in around the mean field version [17] $\eta_{\sigma}=\langle n_{\sigma}\rangle$.

The potential are usually determined for the effective single-particle potentials which used in the effective single-particle Hamiltonian H

$$\begin{aligned}V^{\sigma}_{mm^{'}}&=\left\langle m,m^{''}\left|V_{ee}\right|m^{'},m^{'''}\right\rangle n^{-\sigma}_{m^{''}m^{'''}}\\&+\left(\left\langle m,m^{''}\left|V_{ee}\right|m^{'},m^{'''}\right\rangle-\left\langle m,m^{''}\left|V_{ee}\right|m^{'''},m^{''}\right\rangle\right)n^{\sigma}_{m^{''}m^{'''}}-U(n-\eta)+J\left(n^{\sigma}-\frac{\eta_{\sigma}}{2}\right)\end{aligned} \quad (2.28)$$

REFERENCE:

1- M. Born, and J. Oppenheimer, Ann. Phys. 84, (1927) 457.

2- D. Hartree, Proc. Cambridge Philos. Soc. 24, (1928) 89.

3- V. Z. Fock, Physik 61, (1930) 126.

4- H. Hohenberg and W. Kohn, Phys. Rev. 136 (1964) B864

5- W. Kohn and L. J. Sham, Phys. Rev. 140, (1965) A1133.

6- H. Elliott Lieb, Rev. Mod. Phys. 53 (1981) 603.

7- J. C. Slater, T. M. Wilson, and J. H. Wood, Phys. Rev. 179, (1969) 28.

8- K. Ohno, K. Esfarjani, and Kawazoe, Y. Computational Materials Science (Springer, 1999).

9- D. Ceperley and B. Alder, Phys. Rev. Lett. 45, (1980) 566.

10- J. P. Perdew, and A. Zunger, Phys. Rev. B 23, (1981) 5048.

11- O. Gunnarsson, M. Jonson, and B. I. Lundqvist, Phys. Rev. B 20, (1979) 3136.

12- J. P. Perdew and Yue, W. Phys. Rev. B 33, (1986) 8800.

13- J. P. Perdew, K. Burke and M. Ernzerhof, Phys. Rev. Lett. 77, (1996) 3865.

14- J. Hubbard, Proc. R. Soc. Lond. A 276, (1963) 238

15- V. I. Anisimov and O. Gunnarsson, Phys. Rev. B 43, (1991) 7570

16- V. I. Anisimov, I.V. Solovyev, M. A. Korotin, M.T. Cryzyk and Sawatzky, Phys. Rev. B 48 (1993) 16929.

17- M.T. Cryzyk and Sawatzky, Phys. Rev. B 49 (1993) 14211.

Chapter 03

THEORETICAL METHOD (FP-LAPW)

3.1 INTRODUCTION

During the past fifteen years the techniques for solving the band structure problem have reached the point at which, with the aid of large computers, an accurate solution may be obtained. Among these techniques we can site the augmented plane wave (APW) method, which has allowed the solution of the band-structure problem for a wide class of materials, which requires a computational effort. This is powerful also in the calculation of ground-state properties of compounds and magnetic crystals, where self-consistency is imperative, and in the calculation of excitation spectra, where matrix elements are needed. Furthermore, the APW method has the characteristics of numerical techniques, well suited for accurate calculations on particular crystals.

3.2 THE AUGMENTED PLANEWAVE METHOD

The augmented planewave (APW) method as originally formulated by Slater [1,2], expands a trial wave function in a set of energy-dependent basis functions :

$$\psi_k = \sum_n C_n \phi(k_n, \varepsilon_0) \qquad (3.1)$$

with $k_n = k + G_n$

Where k is a point in the first Brillouin zone, G_n is a reciprocal lattice vector, and ε is the energy used to construct the APW radial functions. The C_n are the plane wave expansion coefficients, which are determined by applying the standard Rayleigh-Ritz variational procedure [3,4]. The basis functions in this way satisfy the cellular boundary conditions and the connectivity conditions across the muffin-tin spheres. Thus the variation yields the simple secular problem [5]

$$\boldsymbol{H}C = E\boldsymbol{S}C \qquad (3.2)$$

where H and S are the Hamiltonian and overlap matrices for a given basis set ϕ_k

with:

$$H_{nm} = \langle \phi(G_n) | H | \phi(G_m) \rangle \qquad (3.3)$$

$$S_{nm} = \langle \phi(G_n) | \phi(G_m) \rangle \qquad (3.4)$$

denoting Hamilton and overlap matrix, respectively,

In this method, the unit cell is partitioned into an interstitial region (I) and non-overlapping muffin-tin spheres (labelled α) centred on the atomic nuclei (Fig. 3.1). In the latter region, potential, density and wave functions are strongly varying, i.e., similar to the situation in an atom, therefore atomic-like basis functions are an appropriate choice.

However, the same quantities are much smoother in the interstitial region and can be well described by plane waves which are the basis functions in the interstitial region. Within the APW method, the corresponding basis functions are defined as,

$$\phi_{k+G}(r) = \frac{1}{\sqrt{\Omega}} e^{i(k+G).r} \qquad r \in I \quad (3.5)$$

and

$$\phi_{k+G}(r) = \sum_{lm} A_{lm}^{\alpha}(k+G) u_l^{\alpha}(r,E) Y_{lm}(\hat{r}), \qquad r \in \alpha \qquad (3.6)$$

where $Y_{lm}(\hat{r})$ are the spherical harmonics. The radial function $u_l^{\alpha}(r,E)$ is the regular solution of the equation:

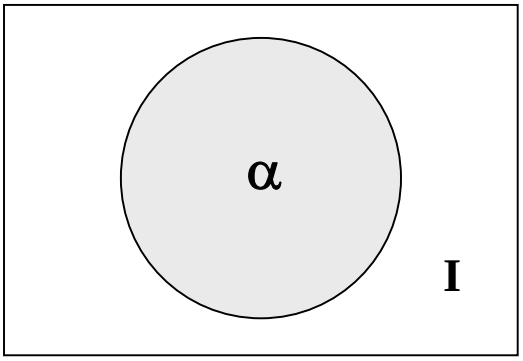

Figure 3.1 Partitioning of the unit-cell volume into atomic spheres and the interstitial region.

$$\left\{ -\frac{d^2}{dr^2} + \frac{l(l+1)}{r^2} + V^{\alpha}(r) - E \right\} r\, {}_l^{\alpha}u(r,E) = 0 \qquad (3.7)$$

with $V^{\alpha}(r)$, being the radial symmetric part of the potential in the atomic sphere. Provided that E is equal to the eigenvalue, $u_l^{\alpha}(r,E)$ is the solution of Schrödinger's equation in the spherical potential, while plane waves are solutions for a constant potential. Therefore, this choice of basis functions is in particular well suited for the so-called muffin-tin (*MT*) approximation, where such a shape approximation, spherical symmetric inside the spheres and constant outside, is assumed for the potential. Indeed most of the APW codes still make use of this approximation which is, however, only good for closed packed structures. The reason is that it is quite complicated to extend the scheme to a general potential inside the atomic spheres [6]. A general potential outside the spheres, however, can be more easily achieved.

The coefficient $A_{lm}^{\alpha}(k+G)$ is determined for each atom by imposing the requirement that the values of the planewave (3.5) and the atomic-orbital like function (3.6) have to match each other on the sphere boundary.

$$A_{lm} = \frac{4\pi i^{l}}{\Omega^{\frac{1}{2}} u_{l}(R)} \sum_{G} c_{G}\, j_{l}(|k+G|) Y_{lm}^{*}(k+G) \qquad (3.8)$$

It depends on *E* which is a variational parameter in this scheme. Therefore, the APWs as defined in Eq. (3.6) are not simply a basis set, but give rise to severe complications: Most important, *E* has to be set equal to the band energy. This requirement makes the basis functions energy-dependent and thus the solution of the secular equation does not correspond to a linear eigenvalues problem. It has to be solved by finding the roots of the secular determinant which is a very time-consuming procedure. Since the APWs are not orthogonal they lead to an overlap matrix in Eq. (3.2) which is not the unity matrix, a fact which is common to all APW-related methods.

In general there are two major computational difficulties connected with the standard augmented plane wave (APW) method originally proposed by Slater (1937); the first is the energy dependence of the secular equation resulting from the nonlinear energy parameter used in setting up the radial solutions inside the muffin-tin spheres. The second is the singular behaviour of the secular equation which occurs when a node of the radial solution falls at the muffin-tin-sphere boundary (the so called asymptotes). This makes it necessary to use more sophisticated methods.

An overview over further difficulties and related numerical problems, as well as respective modifications of the APW method can be found in Ref. [7,8]. Koelling et al. [9] demonstrated that an APW constructed with a linear combination of the radial function and its energy derivative eliminates the older numerical problems which encounter this method.

3.3 LINEARIZED AUGMENTED PLANE-WAVE METHOD (LAPW)

There were several attempts to improve the energy dependence of the secular equations but the first really successful one was the linearization by Andersen [10-13]. This work led to the first implementation of the linearized augmented plane-wave (LAPW) method. In the LAPW method the energy dependence of the radial functions inside each sphere is removed by using a fixed set of suitable muffin tin radial functions. Within Andersen's approach, inside each atomic sphere,

the radial solutions of the Kohn-Sham equation at fixed energies E_l and their energy derivatives are used as basis functions.

The derivate quantity is used to make the continuity of the wave function on the boundary, which distinguishes this approach from the APW method and there is no need for explicit core state orthogonalizations, because the radial solutions and their energy derivatives are exactly orthogonal to the core states of the muffin tin. The wave function in the interstitial region is expressed in the form of equ. 3.5 and the solution of the Schrödinger equation is a linear combination of these bases (Equ. 3.1) where the coefficients c_n are determined by the variational principle. The linear APW (LAPW) method has all the advantages of the OPW method often used for semiconductor.

3.3.1 *THE LAPW BASIS*

The LAPW and APW bases differ only within the spherical regions. Thus in the LAPW and inside atomic sphere α of radius R_α, each ϕ is a linear combination of radial functions times spherical harmonics $Y_{lm}(r)$

$$\phi_{k+G} = \sum_{lm} \left(A_{lm}^{\alpha}(k+G) u_l^{\alpha}(r,E) + B_{lm}^{\alpha}(k+G) \dot{u}_l^{\alpha}(r,E) \right) Y_{lm}(\hat{r}), \qquad (3.9)$$

where $u_l^{\alpha}(r,E)$) is (as in APW) the regular solution of the radial Schrödinger equation for the spherical part of the potential in sphere α, but now for fixed energy E_l. The second set of radial functions, which appears in the LAPW but not the APW, consists of the energy derivatives, $\dot{u}_l^{\alpha}(r,E)$ which given by

$$\dot{u}_l(r,E_l) = \frac{\partial u_l(r,E_l)}{\partial E}\Big|_{E_l} \qquad (3.10)$$

As with the original APW basis, the radial functions, $u_l^{\alpha}(r,E)$ and $\dot{u}_l^{\alpha}(r,E)$ are obtained by numerical integration on a radial mesh inside each sphere. However, the E_l parameter in the LAPW is not required to match the Kohn-Sham eigenvalue ε_{ik}^{0} but is fixed instead to an expected value, for example, to be roughly in the middle of the occupied eigenvalues which are predominantly of angular momentum type *l*.

The coefficients $A_{lm}^{\alpha}(k+G)$ and $B_{lm}^{\alpha}(k+G)$ are determined by requiring that value and slope of the basis functions are continuous at the surface of the muffin tin sphere (sphere boundaries); by expanding each plane-wave into Bessel functions j_l at the muffin tin spheres.

Here, the *G* denotes the reciprocal lattice vectors and *k* a vector within the first Brillouin zone. Note that $Y_{lm}(\hat{r})$ represents a complex spherical harmonic with $Y_{l-m}(\hat{r}) = (-1)^m Y_{lm}^*(\hat{r})$. The radial functions $u_l^\alpha(r,\varepsilon_l)$ and $\dot{u}_l^\alpha(r,\varepsilon_l)$ are solutions of the equations

$$H^{sph} u_l^\alpha(r,\varepsilon_l) = \varepsilon_l u_l^\alpha(r,\varepsilon_l) \tag{3.11}$$

$$H^{sph} \dot{u}_l^\alpha(r,\varepsilon_l) = \left[\varepsilon_l \dot{u}_l^\alpha(r,\varepsilon_l) + u_l^\alpha(r,\varepsilon_l)\right] \tag{3.12}$$

The operator H^{sph} contains only the spherical average, i.e. the *l=0* component, of the effective potential within the muffin tin. The E_l should be chosen near the center of the energy band with the corresponding *l*-character.

The full-potential LAPW method generally expands the potential and the charge density in a Fourier representation

$$V(r) = \begin{cases} \sum_{lm} V_{lm} Y_{lm}(\hat{r}) & inside\,the\,sphere \\ \sum_{k+G} V_{k+G} e^{i(k+G)r} & outside\,the\,sphere \end{cases} \tag{3.13}$$

Thus, no shape approximation is introduced. The quality of this full-potential description is controlled by the wave function cut-off G^{wf} limits the number of the G vectors and thus the size of the basis set and the size of the (*l*,*m*) representation inside muffin tins.

3.3.2 ROLE OF THE LINEARIZATION ENERGIES

In LAPW method and inside the spheres the LAPWs have more variational freedom than APWs. This is because, if E_l differs slightly from the band energy, ε, a linear combination, will reproduce the APW radial function constructed at the band energy.

$$u_l(\varepsilon,r) = u_l(E_l,r) + (\varepsilon - E_l)\dot{u}_l(\varepsilon,r) + \Theta\left((\varepsilon - E_l)^2\right) \tag{3.14}$$

where $\Theta\left((\varepsilon - E_l)^2\right)$ denotes errors that are quadratic in this energy difference. For a converged planewave set and a muffin-tin potential, the APW method yields exactly the correct wave function. In this case, going to the LAPW method introduces errors of order $(\varepsilon - E_l)^2$ in the wave function; this, combined with the variational principle, yields errors of order $(\varepsilon - E_l)^4$ in the band energy. Thus it would seem that one needs simply to set the E_l near the centers of the bands of interest to be assured of reasonable results, and one could in fact optimize the choice by computing the appropriate moments of the density of states and using the known order of the

errors to optimize the E_l. Alternatively, one could envisage computing the total energy for several reasonable choices of E_l and selecting the set that gave the lowest energy. However, these strategies work well in many cases but they fail miserably in many others. The reason for this failure is related to the presence of the semi-core states in many elements, particularly, the alkali metals, the rare earths, the early transition metals and the actinides.

3.3.3 REPRESENTATIONS OF POTENTIAL AND CHARGE DENSITY

Charge density can be constructed by summing over the occupied states:

$$\rho(r) = \sum_{k,l} \psi^*_{k,l} \psi_{k,l} \qquad (3.15)$$

The sum it should be carried out over the full Brillouin zone (BZ). But in practice we work in an irreducible wedge of the BZ (IBZ). However the charge density is not so behaved and therefore the density obtained from the irreducible zone does not necessarily have the full symmetry of the lattice. To obtain the properly symmetrized density it is necessary to using the space group operators. $S = \{R|t\}$

where R is a rotation and t a translation.

In order to treat the charge density correctly, we follow a variant of the scheme used by Weinert [14]. This scheme is based on the fact that to use a dual representation for the charge as well as the wave functions: the interstitial charge is smooth and hence amenable to a Fourier expansion and that in the spheres to be in a spherical harmonic representation, which is the natural representation near an atomic site.

$$\rho(r) = \rho_I(r)\theta(r \in I) + \sum_{spheres} \rho_\alpha(r)\theta \qquad (r \in S_\alpha) \qquad (3.16)$$

However, because of the rapid variation of the charge density near the nuclei, the charge density given by (3.16) will have a slowly convergent Fourier expansion, whereas the interstitial charge density can be continued into the spheres in such a way that it has a rapidly convergent Fourier expansion. We can make use of this observation and solve the problem of obtaining the Coulomb potential in two steps; obtain the potential in the interstitial and then solve the boundary value problem inside the sphere. Since the potential outside the muffin-tin spheres does not depend on the real shape of the charge density inside the spheres but only on the multipole moments of this charge. Hence, we can replace the true rapidly varying charge inside the MT spheres by another,

smoother charge without changing the potential outside the spheres if the full pseudo-charge-density is required to have the correct multi-pole moments.

$$\rho(r) \to \tilde{\rho}(r) = \rho_I(r)\theta\,(r \in I) + \sum_{spheres} \tilde{\rho}_\alpha(r)\theta \qquad (r \in S_\alpha) \tag{3.17}$$

The replacement of the original charge density by a smooth pseudocharge inside the spheres is done in two steps:

(I) The expansion of the charge density in the interstitial region, $\rho^{PW}(r)$, is extended into the muffin-tin spheres.

(II) The difference charge density $\Delta\rho(r) = \rho(r) - \rho^{PW}(r)$ for r inside sphere is replaced by a smooth charge density $\Delta\tilde{\rho}(r)$ (the difference pseudo-charge-density), which has the same multipole moments as $\Delta\rho(r)$.

This pseudocharge density will give the correct interstitial potential, but not the correct potential in the spheres

3.4 THE LAPW+LO BASIS SET

Sometimes, it is necessary to extend the LAPW basis set with so-called local orbitals (LO), as introduced by Singh [6]. The local orbital extension to the LAPW basis is directed a better description of the so called semi-core states, low-lying valence states which cannot be treated as part of the core states, i.e., they can have some charge leaking out of the atomic spheres. As the computation of Eq. (3.9) gives good results only for energy values near the linearization energy E_l we need to add another basis to threat these semi core states. This LO scheme avoids the problem of non-orthogonality that can occur in calculations in which the semi-core states are either frozen or treated in a separate energy windows. An LO is chosen such that it vanishes in values and slope at the muffin tin radius and includes an additional radial function. This procedure is done only in the atomic sphere region. The local orbital expansion when $x \in \alpha$ is given by

$$\phi_{LO}(S_\alpha + r) = \sum_{lm} \left[A_{lm}^{\alpha}(k+G)u_l^{\alpha}(r,E) + B_{lm}^{\alpha}(k+G)u_l^{\alpha}(r,E) + C_{lm}^{\alpha}(k+G)u_l^{\alpha}(r,E_{lo})\right] Y_{lm}(\hat{r}), \tag{3.18}$$

where A^{α}_{lm}, B^{α}_{lm} and C^{α}_{lm} are determined by requiring that the local orbitals have zero value and slope at the atomic sphere boundary. Local orbitals are not required to match the basis functions in the interstitial as a result they do not have k + G dependence. The inclusion of local orbitals results in just a small increase of the size of the basis and it allows the proper treatment of

localized semicore states. Compared to other schemes within the local density approximation, the FLAPW can be applied to a wide range of systems due to the use of mixed basis sets by including core electrons.

2.5 WIEN2K CODE

the linearized-augmented-plane-wave (LAPW) method is one among the most precise schemes to solve the so-called Kohn–Sham (KS) equations it has proven to be one of the most accurate methods for the computation of the electronic structure of solids, in general (metals, insulators, semiconductors, minerals, etc.), within density functional theory. This method is employed in many computer codes like FLEUR, WIEN2k [15] to study crystal properties on the atomic scale (see www.wien2k.at). This later code which called WIEN in the first copyrighted version has reached a high level of sophistication in the newest versions this progress led to a significant improvement in the possibilities of simulating relatively large systems.

The *WIEN2k* package consists of several independent programs, written in FORTRAN 90, which are linked via C-SHELL SCRIPTS and requires a UNIX operating system. The flow and usage of the different programs is illustrated in the following diagram (Fig. 3.2).

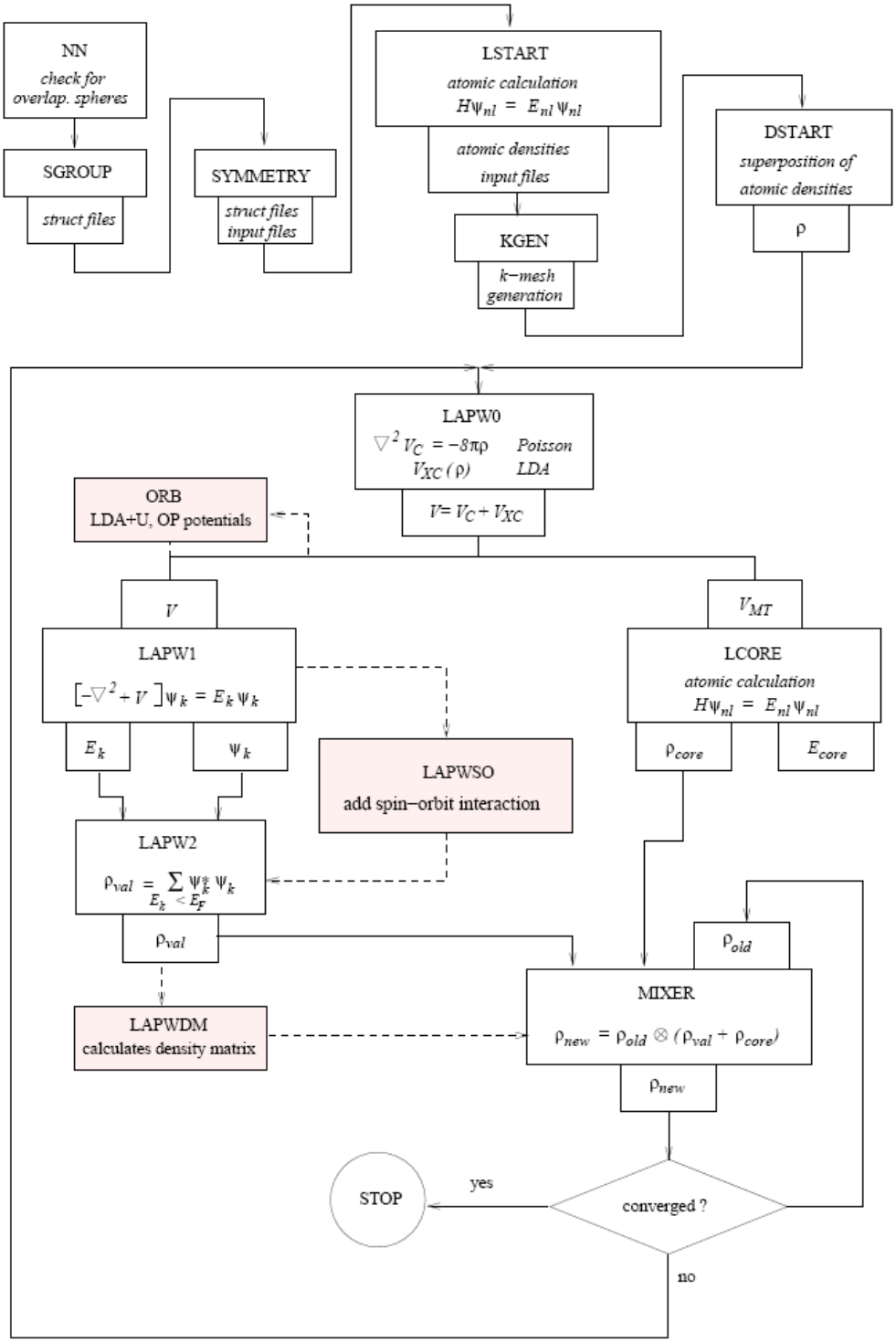

Figure 3.2 Program flow in WIEN2K as illustrated in the user guide of this code

3.6. CALCULATION OF THE PROPERTIES

3.6 .1. Total energy

Within wien2k code, the ground state total energy is given by the minimum of a total energy functional with respect to the electron density n(r),

$$E_0 = \sum \varepsilon_i + E_{xc}[\rho(r)] - \int v_{xc}(r)\rho(r)dr - \frac{1}{2}\int \frac{\rho_0(r)\rho_0(r')}{|r-r'|} drdr' \qquad (3.19)$$

3.6 .2. ELASTIC PROPERTIES

The cubic crystal has three independent elastic constant c_{11}, c_{12}, and c_{44}. To determine these constant three equations are needed. This means three types of strain must be applied; calculating the bulk modulus, performing volume conservative tetragonal strain and applying rhombohedral distortion. Then, from the expression of the energy as function of the strain the elastic constants are derived.

Using the individual elastic constants, we have estimated the following parameters:

The shear anisotropy factor [16].

$$A = \frac{2c_{44}}{c_{11} - c_{12}} \qquad (3.20)$$

The Voigt's shear modulus (G_V) [17] and the Reuss's one G_R[18] for the cubic polycristals are given by:

$$G_V = \frac{1}{5}(c_{11} - c_{12} + 3c_{44}) \qquad (3.21)$$

and

$$G_R = \frac{5c_{44}(c_{11} - c_{12})}{4c_{44} + 3(c_{11} - c_{12})} \qquad (3.22)$$

According to Hill [19], the Voigt's and Reuss's expressions represent the upper and lower limit for the polycrystalline crystals, respectively. The estimate value is given by the average of these values:

$$G = \frac{1}{2}(G_v + G_R) \qquad (3.23)$$

The Young's modulus, *E*, and Poisson's ratio, ν, are given by the following relations:

$$E = \frac{9BG}{3B + G} \qquad (3.24)$$

and

$$\nu = \frac{3B - 2G}{2(3B + G)} \tag{3.25}$$

The average sound velocity, v_m, by the following equation [20]:

$$\theta_D = \frac{h}{k}\left[\frac{3n}{4\pi}\left(\frac{N_A \rho}{M}\right)\right]^{1/3} \nu_m \tag{3.26}$$

where h is Plank's constant, k the Boltzman's constant, N_A the Avogadro nomber's, ρ the density, M the molecular weight and n is the number of atoms in the molecule. The average sound velocity is given by

$$\nu_m = \left[\frac{1}{3}\left(\frac{2}{v_t^3} + \frac{1}{v_l^3}\right)\right]^{-\frac{1}{3}} \tag{3.27}$$

where v_l and v_t are the longitudinal and transverse sound velocity, respectively, which are given by

$$v_l = \sqrt{\frac{3B + 4G}{3\rho}} \tag{3.28}$$

and

$$v_t = \sqrt{\frac{G}{\rho}} \tag{3.29}$$

3.6 .3. OPTICAL PROPERTIES

The linear optical properties in solids are described by the dielectric tensor, the interband contribution to the imaginary part of its elements are calculated by summing transitions from occupied to unoccupied states over the BZ, weighted with the appropriate momentum matrix elements as given in reference [21]:

$$\varepsilon_2(\omega)_{\alpha\beta} = \frac{4\pi^2 e^2}{m^2 \omega^2} \sum_{i,f} \int \langle f | P_\alpha | i \rangle \langle i | P_\beta | f \rangle \times W_i (1 - W_f) \delta(E_f - E_i - \eta\omega) d^3k \tag{3.30}$$

in this expression, $\langle f | p_\alpha | i \rangle$ and $\langle i | p_\beta | f \rangle$ are the dipole matrix elements corresponding to the α and β directions of the crystal (x, y or z), and f, i are the final and initial states, respectively. W_n is the Fermi distribution function for the nth state, and E_n is the electron energy in the nth state. The real part of the elements of the dielectric tensor is obtained using the Kramer-Kronig relation:

$$\varepsilon_1(\omega)_{\alpha\alpha} = 1 + \frac{2}{\pi} P \int_0^{\infty} \frac{\omega' \varepsilon_2(\omega')_{\alpha\alpha}}{\omega'^2 - \omega^2} d\omega' \qquad (3.31)$$

where *P* is the principal value of the integral. With the knowledge of the complex dielectric tensor components all other frequency dependent optical constants can be obtained. The most often used ones are the coefficient of the absorption α (ω) which is defined as:

$$\alpha(\omega)_{\alpha\alpha} = \frac{2\omega}{c}\left(\frac{-\mathrm{Re}\left[\varepsilon(\omega)_{\alpha\alpha} + \left|\varepsilon(\omega)_{\alpha\alpha}\right|\right]}{2}\right)^{\frac{1}{2}} \qquad (3.32)$$

and the reflectivity R(ω) as

$$R(\omega)_{\alpha\alpha} = \left|\frac{1 - \hat{n}(\omega)_{\alpha\alpha}}{1 + \hat{n}(\omega)_{\alpha\alpha}}\right|, \qquad (3.33)$$

where $\hat{n}(\omega)$ is the complex refraction index which is given by the expression:

$$\hat{n}(\omega)_{\alpha\alpha} = n(\omega)_{\alpha\alpha} + ik(\omega)_{\alpha\alpha} \qquad (3.34)$$

with n(ω) is the ordinary refraction index and k(ω) is the coefficient of extinction, obtained from

$$\left[\hat{n}(\omega)_{\alpha\alpha}\right]^2 = \varepsilon_1(\omega)_{\alpha\alpha} + i\varepsilon_2(\omega)_{\alpha\alpha} \qquad (3.35)$$

3.6 .4 MAGNETO-OPTICAL PROPERTIES

The complex Kerr angle ϕ is calculated by using the relation [24]

$$\phi = \theta_k + i\varepsilon_k = \frac{-\sigma_{xy}}{\sigma_{xx}\sqrt{1 + i\frac{4\pi\sigma_{xx}}{\omega}}}, \qquad (3.36)$$

where σ_{xx} and σ_{xy} are the diagonal and the off diagonal elements of the optical conductivity tensor, respectively, ω is the photon frequency and θ_k and ε_k are the Kerr rotation and ellipticity respectively.

REFERENCES

1- J. C. Slater Phys. Rev. **92**, 603 (1953)

2- M. M. Saffren and J. C. Slater Phys. Rev. **92**, 1126 (1953)

3- W. Kohn, *Phys. Rev.* **71** 9024 1947

4- Phys. Rev 7.4 1763-72 1948

5- D. D. Koelling and G. O. Arbman J. Phys. F: Metal Phys 5 2041 (1975)

6- David J. Singh, Planewaves, Pseudopotentials and the LAPW Method, Kluwer Academic 7-Publishers, Boston/Dordrecht/London, 1994

7- D. D. Koelling phys Rev. B 2, (1970) 290.

8- D. D. Koelling, Solid State Commun. 9 (1971) 523.

9- D. D. Koelling, G. O. Arbman, J. Phys. F 5, (1975) 2041.

10- O. K. Andersen, Phys Rev B 12, (1975) 3060.

11- D. D. Koelling, G. O. Arbman, J. Phys. F 5, (1975) 2041.

12- D.R. Hamann, Phys. Rev. Lett. 42, (1979) 662.

13- E. Wimmer, H. Krakauer, M. Weinert and A.J. Freeman, Phys. Rev. B 24, (1981) 864.

14- M. Weinert, J. Math. Phys. 22, (1981) 2433.

15- P. Blaha, K. Schwarz, P. Sorantin, and S. B. Trickey, in Comput. Phys. Commun. 59, (1990) 399.

18- Z. Suna, S. Li, R. Ahujab, J.M. Schneider, Solid State Commun. 129 (2004) 589.

19- W. Voigt, Lehrbuch der kristallphysik, Taubner, Leipzig, 1928.

20- A. Reuss, Z. Angew. Math. Mech. 9 (1929) 55.

21- R. Hill, Proc. Phys. Soc. Lond. 65 (1953) 909.

22- Y.-J. Hao, X.-R. Chen, H.-L. Cui, Y.-L. Bai, Physica B 382 (2006) 118.

23- C. Ambrosch-Draxl, J.O. Sofo, Comput. Phys. Commun. 175 (2006) 1.

24- M. Kumar, T. Nautiyal and S. Auluck, J. Phys. Condens. Matter 21, (2009) 196003.

Chapter: 04

Results and Discussion

HALF HEUSLER ALLOYS IrMnZ (Z=Al, Sn AND Sb)

4.1. INTRODUCTION

As we have mentioned previously, the Heusler alloys are particularly interesting due to their very high Curie temperature [1,2] and some of them are already in use as elements in multilayered magnetoelectronic devices such as magnetic tunnel junctions and also as giant magnetoresistance spin valves [3,4]. Several papers have been devoted to the calculation of the structural, electronic and magnetic properties of these alloys and recently there has been an increased interest in thin films of this material both experimentally [4-7] and using first-principle calculations [8,9]. The Mn-based Heusler alloys (XMnZ) belong to a class with interesting magnetic properties; exhibiting ferromagnetic features like magneto-optical effects and giant magneto-resistance, a comprehensive study of Mn based compounds have been performed by Brown et al. [10] and Plogmann et al. [11]. Among these, the half-Heusler alloys IrMnZ (Z = Al, Sn and Sb) for which few papers have been devoted to the calculation of the different properties. One of the old works on these alloys is of Masumoto and Watanabe [12], who determined their structural and magnetic properties. Krishnamurthy et al. [13], reported on the X-ray magnetic circular dichroism measurements, performed at the Ir $L_{2,3}$ edges at room temperature, in IrMnAl. Galanakis [14] has studied the orbital magnetism in IrMnSb using the Dirac formalism within the framework of the Korringa–Kohn–Rostoker Green's function method. More recently, Antonov et al. [15] have studied by means of the ab initio fully relativistic spin-polarized Dirac linear muffin-tin orbital method the electronic structure and XMCD spectra of IrMnAl at the Ir $L_{2,3}$ edge. However, the elastic constants and moduli which have not yet been calculated or measured for the studied compounds are of extreme interest in both condensed matter theory and technological fields. The elastic constants (cij) determine the response of the materials to the external forces and play an important role in determining the strength of the compounds, which is the key in high temperature and pressure applications. Therefore, knowledge of the elastic constants will be of great interest in understanding their behaviour under different constraints. In addition the knowledge of the fundamental structural and mechanical properties can be helpful to understand the electronic, optical, and magneto-optical behaviour. These two later properties have not yet been calculated theoretically.

Our aim in this chapter is to investigate the elastic, electronic and magneto-optical properties of the IrMnZ (Z = Al, Sn and Sb) in the $C1_b$ type ordered structure using the state of the art full potential linearized augmented plane wave method (FP-LAPW) [16,17], in the framework of the density functional theory (DFT) within the generalized gradient approximation [18–20].

4.2. CRYSTAL STRUCTURE AND DETAILS OF CALCULATIONS

The crystal structure used in the calculation for these half-Heusler compounds is of the AlLiSi type [21], space group $F\bar{4}3m$ (No. 216). In this structure, one discerns four types of sites $\tau_1(0, 0, 0)a$, $\tau_2(1/4, 1/4, 1/4)a$, $\tau_3(1/2, 1/2, 1/2)a$ and $\tau_4(3/4, 3/4, 3/4)a$, where a denotes the lattice parameter, occupied as follows: Ir at τ_1, Mn at τ_2 and Z at τ_4, while τ_3 is empty. Furthermore, this structure is similar to the β-phase of the Nowontny-Juza compounds [22]. Our calculations are performed using the full potential linearized augmented plane wave plus local orbitals method, FP-LAPW+LO [16,17] within the generalized gradient approximation GGA (GGA+U) and the local density approximation LSDA (LSDA+U) [20]. In this method the space is divided into non-overlapping muffin-tin (MT) spheres separated by an interstitial region. In this context, the basis functions are expanded in combinations of spherical harmonic functions inside the muffin-tin spheres and Fourier series in the interstitial region. In this work we treat the core electrons fully relativistically, and the valence electrons semi-relativistically. In the calculations, The muffin-tin radii are chosen to be 2.1 Bohr for Al and Mn and 2.3 Bohr for Ir, Sn and Sb. The basis functions are expanded up to $R_{mt} \times K_{max} = 8$ (where K_{max} is the plane wave cutoff and R_{mt} is the smallest of all MT sphere radii), and up to $l_{max}=10$ in the expansion of the non-spherical charge and potential. We use the Perdew, Burk and Ernzerhof scheme [20], for the exchange and correlation interaction. The integrations over the Brillouin zone are performed with 14×14×14 k mesh and the self-consistent calculations are considered to be converged when the total energy is stable within 0.1 mRy. The theoretical equilibrium total energy, lattice parameter a and bulk modulus B are determined by fitting the total energy as a function of volume for both the non magnetic and magnetic (spin polarized) phases to the Murnaghan's equation of state (eos) [23].

In crystals with the $C1_b$ structure the elastic tensor has only three independent elastic constants, namely c_{11}, c_{12} and c_{44}. Their determination requires knowledge of the

curvature of the energy as a function of strain for selected deformations of the unit cell, as mentioned in previous chapter.

The calculation of the optical and magneto-optical properties has been performed using 8000 k-points with 20×20×20 k mesh. In order to consider the effect of finite lifetimes, as well as of the experimental resolution, a Lorentzian broadening equal to δL= 0.7 eV was applied for both the interband and intraband contributions. Drude broadening equal to δ_D= 0.1 eV in the intraband contributions and we also added empirical intraband Drude conductivity, σ_0 to the calculated interband conductivity.

We have used the value of U calculated using the method of Anisimov [32]. The calculated values are given in table 4.1, and knowing that there are many methods to estimate this value. The only external parameter needed for LSDA+U (GGA+U) is the effective value of the on-site Coulomb parameter, U_{eff}, for each affected orbital. The effective parameter U_{eff} = U - J is adopted as an only input parameter, where U and J are the Coulomb and exchange parameters, respectively. In this work J has been assumptive set equal 0.

Table 4.1 *The calculated U (eV) values of Ir and Mn of IrMnZ (Z = Al, Sn and Sb).*

		GGA	LSDA
IrMnAl	Ir	0.28	0.30
	Mn	3.62	3.66
IrMnSn	Ir	0.24	0.23
	Mn	4.20	4.44
IrMnSb	Ir	0.3	0.3
	Mn	2.89	3.12

4.3. STRUCTURAL PROPERTIES

The calculated energy curves as a function of volume for the magnetic (spin-polarized) and non-magnetic configurations, using the generalized gradient approximation (GGA) of the three compounds are displayed in Fig. 4.1.

The obtained total energy differences $E_{non\text{-}magnetic} - E_{magnetic}$ (in meV per formula) using GGA are: 39, 100 and 128 mRy for IrMnAl, IrMnSn and IrMnSb, respectively, indicating that the magnetic phase is the energetically favourable one, and this result

agrees with the one reported by Offernes et al. [21]. As it is clear from Fig. 4.1, the rest of this chapter will be devoted to the magnetic phase only.

Table 4.2 *Calculated and experimental lattice constants of IrMnZ (Z =Al, Sn and Sb).*

	a (Å)				
	GGA	GGA+U	LSDA	LSDA+U	Expt.[a]
IrMnAl	5.669	5.956	5.566	5.806	5.992
IrMnSn	6.197	6.307	6.029	6.160	6.182
IrMnSb	6.155	6.258	6.012	6.115	6.164

[a]Ref [21]

Table 4.3 *Calculated bulk modulus of IrMnZ (Z = Al, Sn and Sb).*

	B(GPa)				
	GGA	GGA+U	LSDA	LSDA+U	Expt.[a]
IrMnAl	156.72	109.81	208.05	127.40	--
IrMnSn	112.74	106.18	141.47	136.45	--
IrMnSb	128.16	117.95	175.40	153.29	--

The equilibrium lattice constant and bulk modulus were calculated using both LSDA and GGA for these half-Heusler compounds in the cubic $C1_b$ structure; the results are compared with available experimental data in Table 4.2. A comparison between the equilibrium lattice constants predicted using LSDA and GGA for the exchange and correlation functional shows that GGA is reproduce well the equilibrium structural properties of these half-Heusler alloys. In fact, LSDA underestimates the equilibrium volume by about -7.17% -2.47% and -2.46% with respect to experiment, whereas the GGA error are −5.5%, −0.28% and +0.17% for IrMnAl, IrMnSn and IrMnSb, respectively. The obtained values follow the same trend as the measured ones. Thus leading to a better agreement with experiment compared to LSDA.

The prediction of some properties probably can not be reproduced by the GGA and LSDA methods. The standard LSDA does not consider the correlated behavior of electrons in the d shell. The modified LSDA (GGA), which is called LSDA+U (GGA+U), was used explicitly including the on site Coulomb interaction U in the conventional model Hamiltonian for the band states. The structural parameters are

also given in table 4.2 and 4.3. From these tables, it is clear that the GGA gives good results compared to the other approximations.

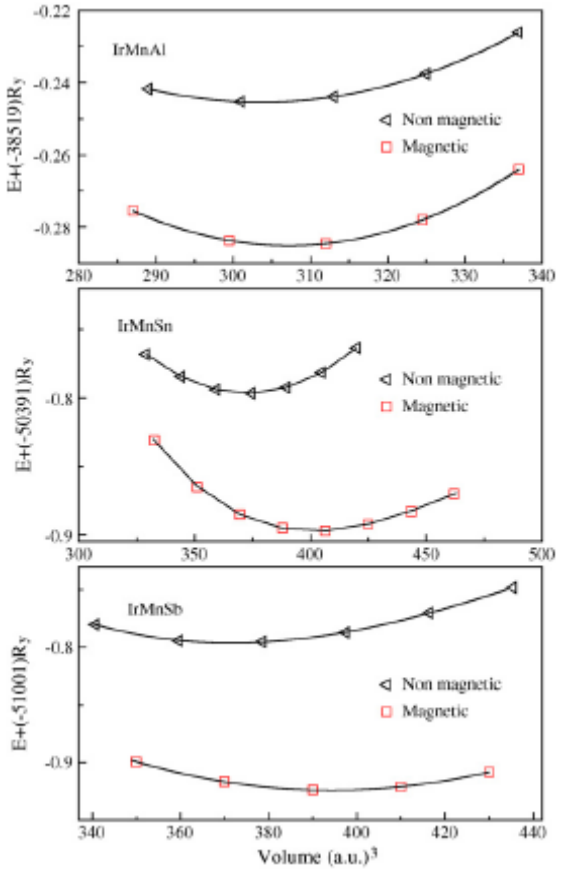

Figure 4.1 Total energy of the IrMnZ (Z=Al,Sn and Sb) compounds vs. volume per unit cell using the GGA.

4.4. ELASTIC PROPERTIES

The calculated elastic constants with the GGA are listed in Table 4.4. The bulk modulus calculated from the theoretical values of the elastic constants $B = \frac{1}{3}(c_{11} + 2c_{12})$ is also listed in this table, and it has nearly the same value as the one obtained from energy minimization (see Table 4.3 for comparison). This might be an estimate of the reliability of the predicted results for the studied materials.

Table 4.4. *Elastic constants (in GPa), the bulk modulus* $B = \frac{1}{3}(c_{11} + 2c_{12})$ *(in GPa) and the anisotropy factor A for the IrMnZ (Z=Al, Sn and Sb).*

Compound	C_{11} (GPa)	C_{12} (GPa)	C_{44} (GPa)	B (GPa)	A
IrMnAl	212.94	122.25	148.94	152.48	3.28
IrMnSn	134.06	103.46	43.45	113.65	2.84
IrMnSb	158.39	122.00	98.34	134.13	5.40

The requirement of mechanical stability in a cubic crystal leads to the following restrictions on the elastic constants [25,26]; $(c_{11}-c_{12})>0$, $c_{11}>0$, $c_{44}>0$, $B>0$. All the calculated elastic constants in Table 4.4 satisfy these mechanical stability criteria, including the fact that c_{12} must be smaller than c_{11}, which leads to a restriction on the magnitude of B; $c_{12} < B < c_{11}$.We have also listed in Table 4.4 the shear anisotropy factor [27], which is the ratio between the shear modulus for the {001} planes along the [100] direction ($G_{\{001\}}=c_{44}$) and the one for {110} planes along the direction [110] ($G_{\{110\}} = (1/2)(c_{11} - c_{12})$). The value of *A* is equal to one for an isotropic crystal, while any deviation from unity provides a measure of the degree of anisotropy of the electronic charge distribution [28]. From Table 4.4, the values of *A* for IrMnAl, IrMnSn and IrMnSb are 3.28, 2.84 and 5.40, respectively, which are greater than one (i.e., $G_{\{001\}}>G_{\{110\}}$) this is an indication that the studied compounds shear easier on the {110} rather than on the {001} planes. Furthermore, IrMnSb is characterized by a strong anisotropy for the shear planes described above compared to the other two compounds.

Table 4.5. *The calculated shear moduli* G_v G_R *and G and Young's modulus E (in GPa) and Poisson's ratio ν for the IrMnZ (Z=Al, Sn and Sb) compounds.*

Compound	G_v	G_R	G	E	ν
IrMnAl	107.502	77.82	92.66	231.15	0.247
IrMnSn	32.190	25.03	28.61	79.19	0.331
IrMnSb	66.282	35.61	50.94	135.65	0.383

4.4.1. ELASTIC PROPERTIES AND DEBYE TEMPERATURE FOR POLYCRYSTALS

Using the individual elastic constants, we have estimated the shear modulus (G) (Equ. 3.23) by the Voigt's approximation (Equ. 3.21) and the Reuss's one (Equ. 3.22). According to Hill [28], the Voigt's and Reuss's expressions represent the upper and lower limit for the polycrystalline crystals, respectively, and the arithmetic mean value can then be taken for estimation of the shear modulus (Equ. 3.23). We have estimated also The Young's modulus, *E* (Equ. 3.24), and Poisson's ratio, ν(Equ. 3.25) The calculated results are given in table 4.5. We show that all these parameters have the same trend and decrease with increasing the lattice parameter.

Debye temperature (θ_D) is a fundamental physical property and correlates with many physical properties of solids, such as specific heat and the thermal expansion coefficient [30]. It is used to distinguish between high and low temperature regions for a solid. If the temperature $T>\theta_D$, we expect all modes to have the energy of k_{BT}, and if $T<\theta_D$, one expects the high-frequency modes to be frozen [31], i.e. the vibrational excitations arise solely from the acoustic vibrations. We estimated the Debye temperature θ_D of the studied compounds IrMnZ using the relation (3.26).

Table 4.6. *The calculated density (ρ in g.cm^{-3}), the longitudinal, transverse and average sound velocities (v_l, v_T, v_m in ms^{-1}) and the Debye temperatures θ_D (in K) for the IrMnZ (Z=Al, Sn and Sb).*

Compound	ρ	v_l	v_T	v_m	θ_D
IrMnAl	09.993	5255.66	3045.09	3379.58	406.53
IrMnSn	10.210	3855.95	1673.96	1890.76	208.06
IrMnSb	10.507	4049.19	1650.11	1868.07	206.96

The calculated densities, longitudinal, transverse, average velocities and the Debye temperature are listed in Table 4.6. The IrMnAl has the largest value of θ_D, while IrMnSn and IrMnSb have almost the same value. Debye temperature is directly related to the elastic constants, (Equ. 3.32), via average wave velocity, and the decreasing of wave velocity causes the increase in Debye temperature. Unfortunately, as far as we know, there are no experimental data available related to this property in

the literature for the IrMnZ compounds, therefore our calculated values can be considered as prediction of these properties for the IrMnZ compounds.

4.5. ELECTRONIC PROPERTIES

Before starting this discussion we should mention that the generalized gradient approximation GGA and the local spin density approximation LSDA are used to calculate the different properties, but we have based our discussion on the GGA results and for a comparative study of our calculated results for electronic and magneto-optical properties we have presented our LSDA results in some cases only.

Our endeavor is to calculate the electronic properties with and without the inclusion of Coulomb interaction in the standard density functional formalism.

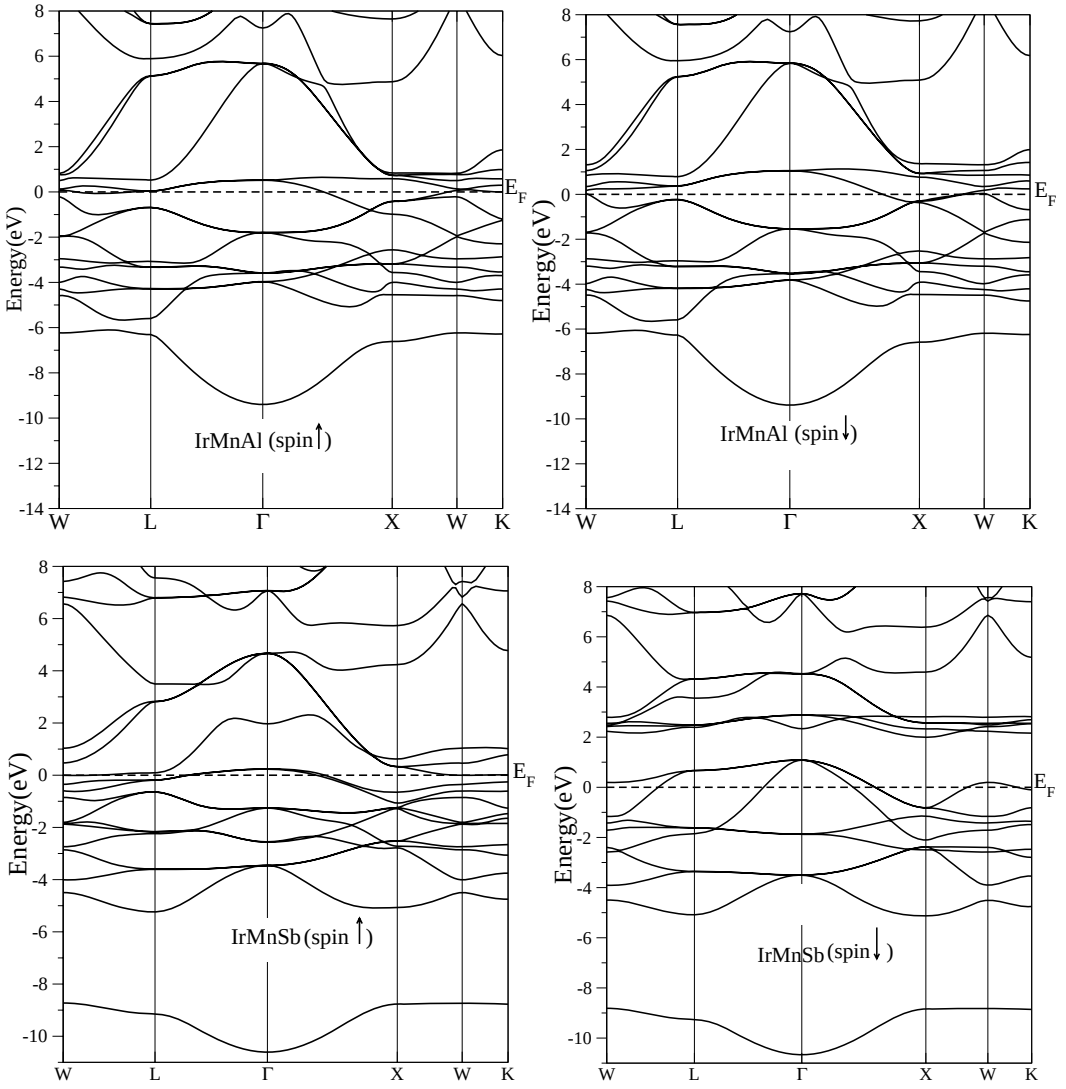

Figure 4.2a Band structure of the IrMnAl and IrMnSb along the high cubic symmetry lines without spin orbit effect.

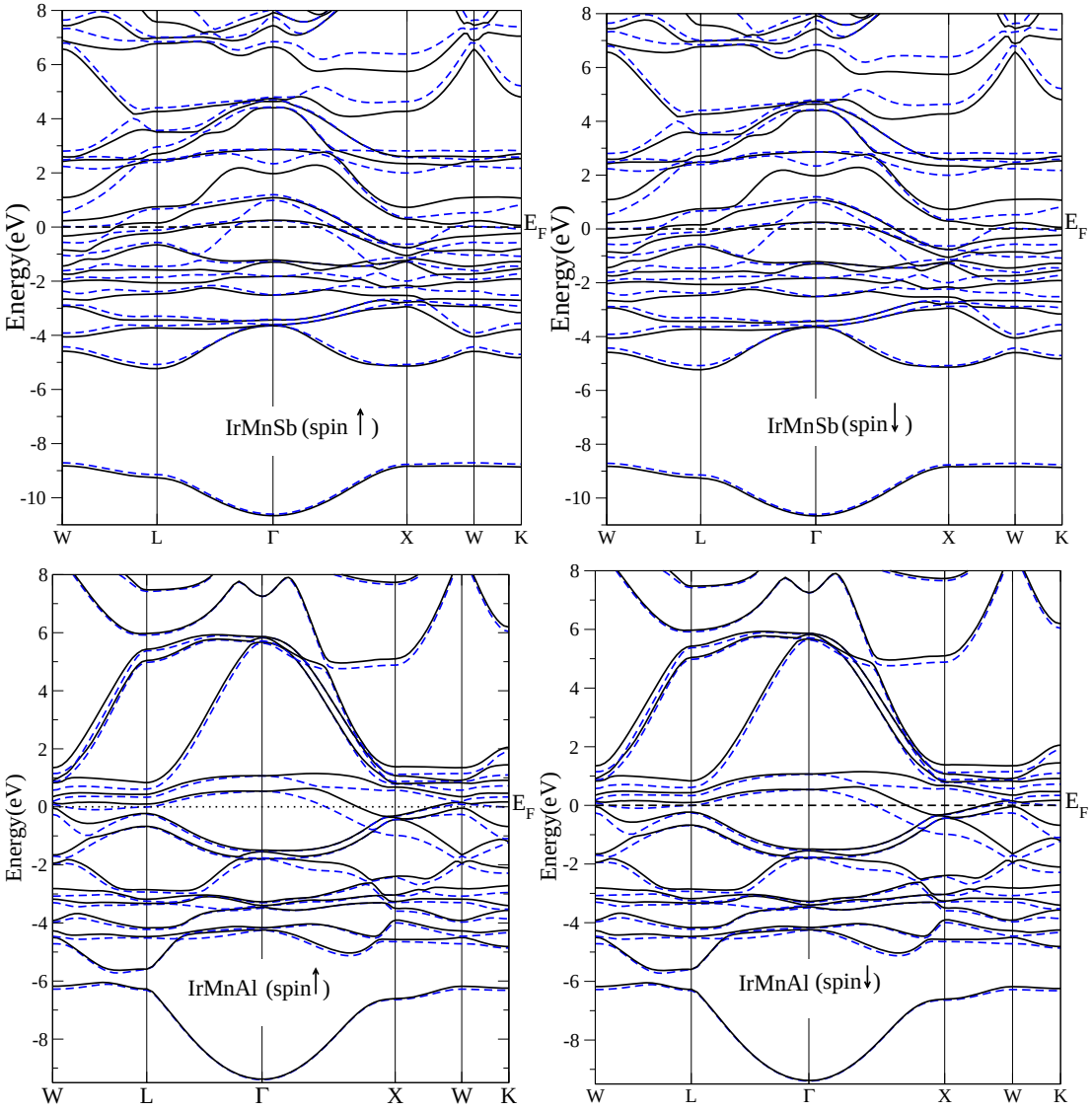

Figure 4.2b Band structure of the IrMnAl and IrMnSb compounds along the high cubic symmetry lines with spin orbit effect.

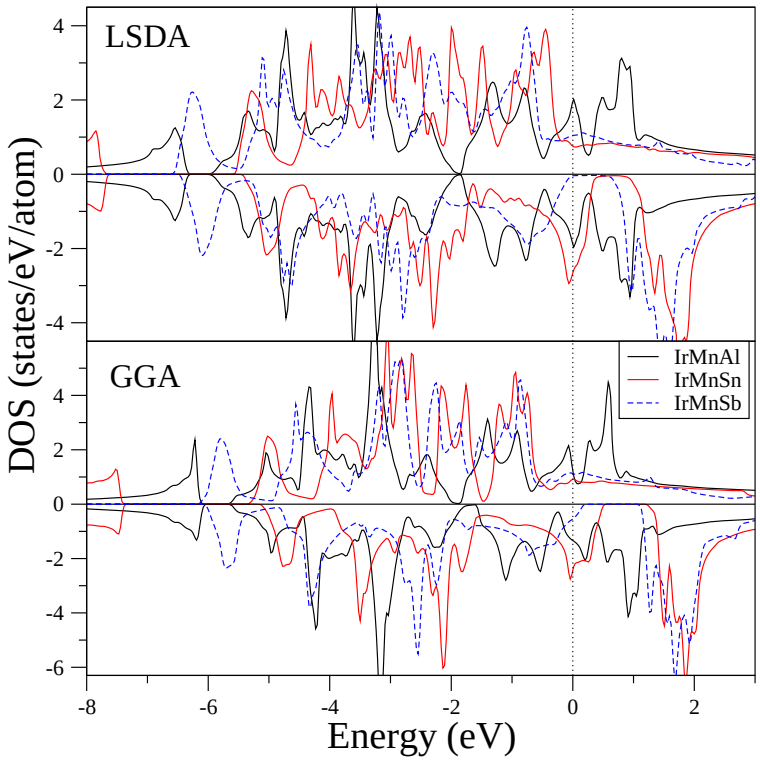

Figure 4.3 Total density of states, by LSDA and GGA, for the majority and the minority spins in half-Heusler alloys: IrMnZ (Z=Al, Sn, Sb). The vertical doted line at zero energy indicates the Fermi level.

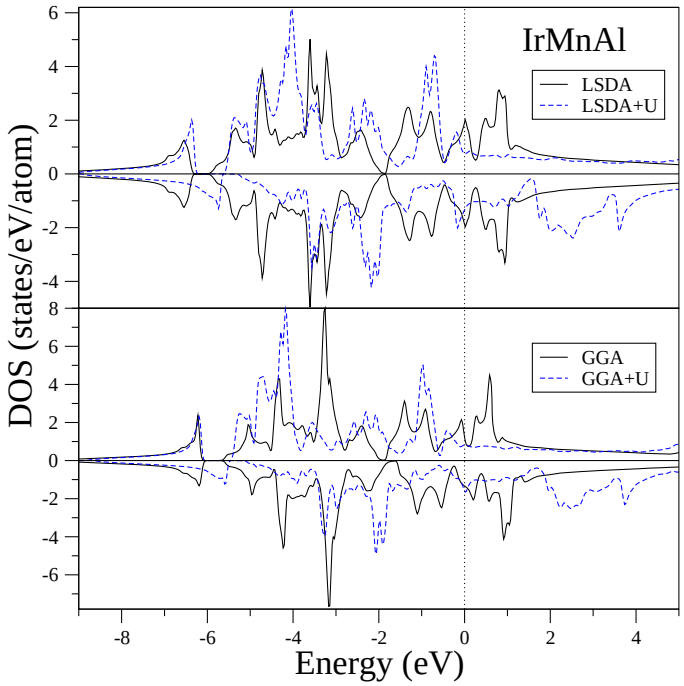

Figure 4.4 Comparison of the total density of state between the LSDA(LSDA+U) and GGA (GGA+U), for the majority and the minority spins in half-Heusler alloys IrMnAl. The vertical doted line at zero energy indicates the Fermi level.

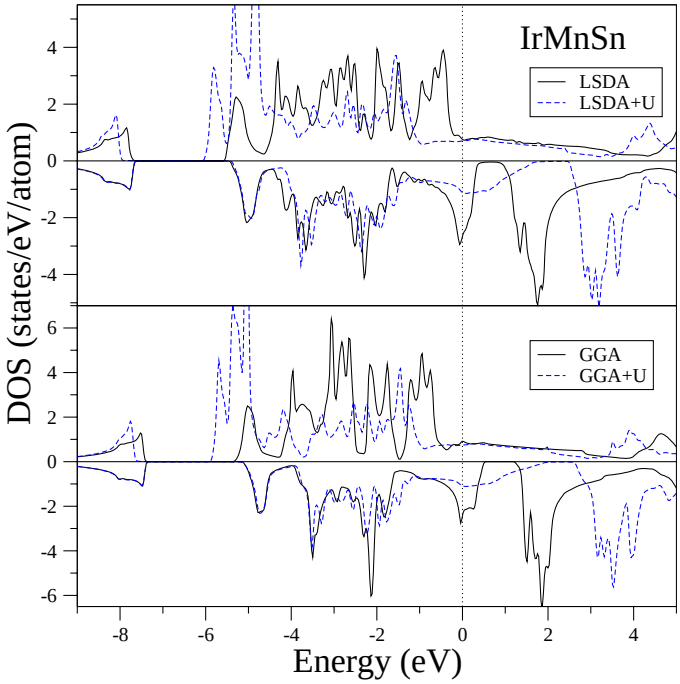

Figure 4.5. Same as in figure 4.4 but for IrMnSn

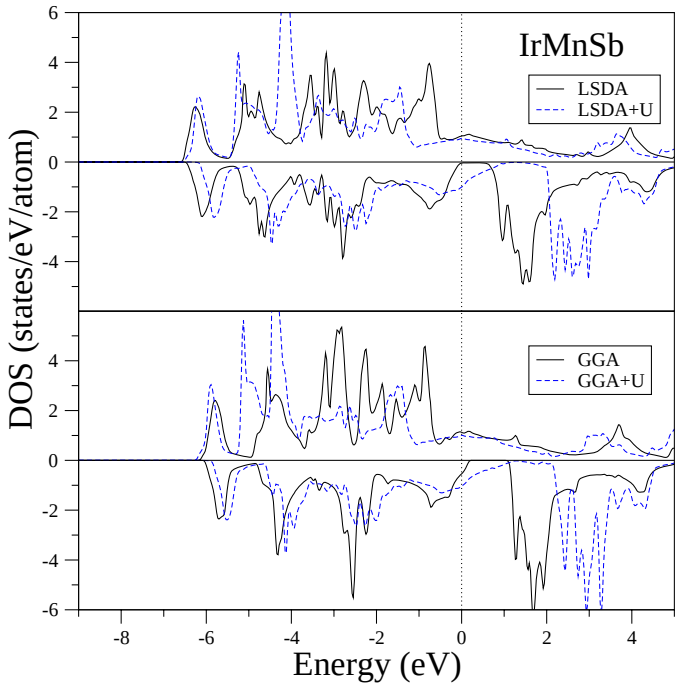

Figure 4.6. Same as in figure 4.4 but for IrMnSb

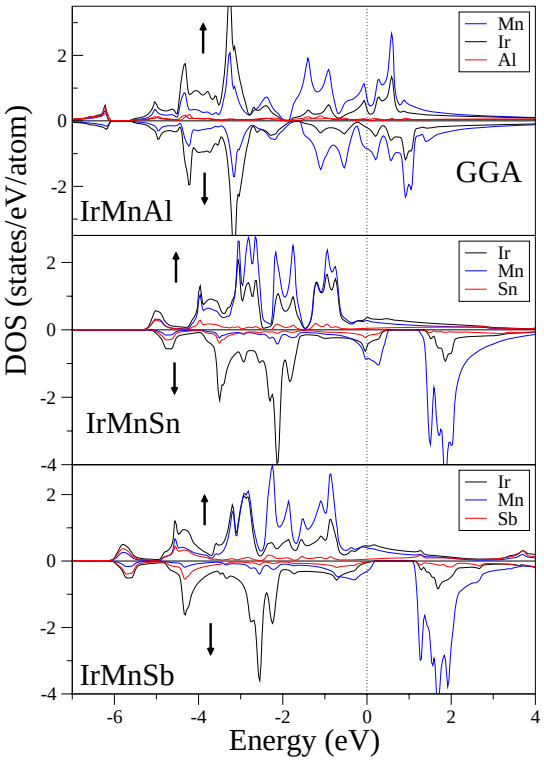

Figure 4.7. Total density of state of each element, by GGA, for the majority and the minority spins in half-Heusler alloys: IrMnZ (Z=Al, Sn, Sb).

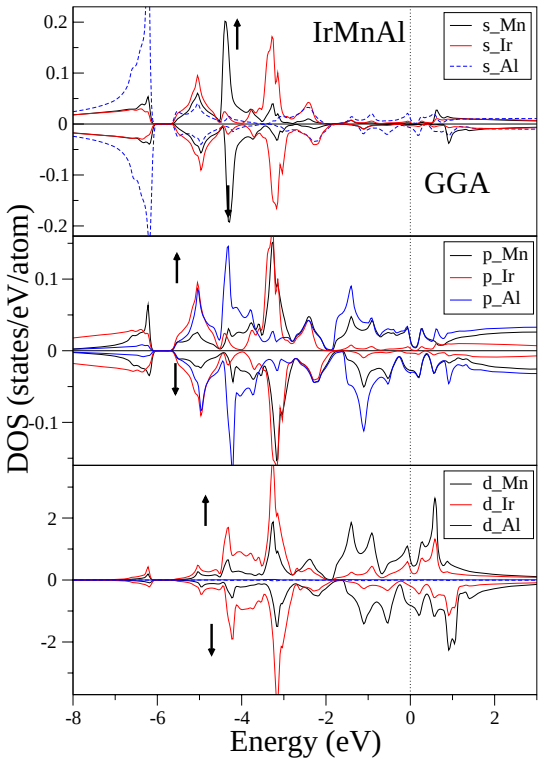

Figure 4.8. Partial density of state, by GGA, for the majority and the minority spins in half-Heusler alloys IrMnAl.

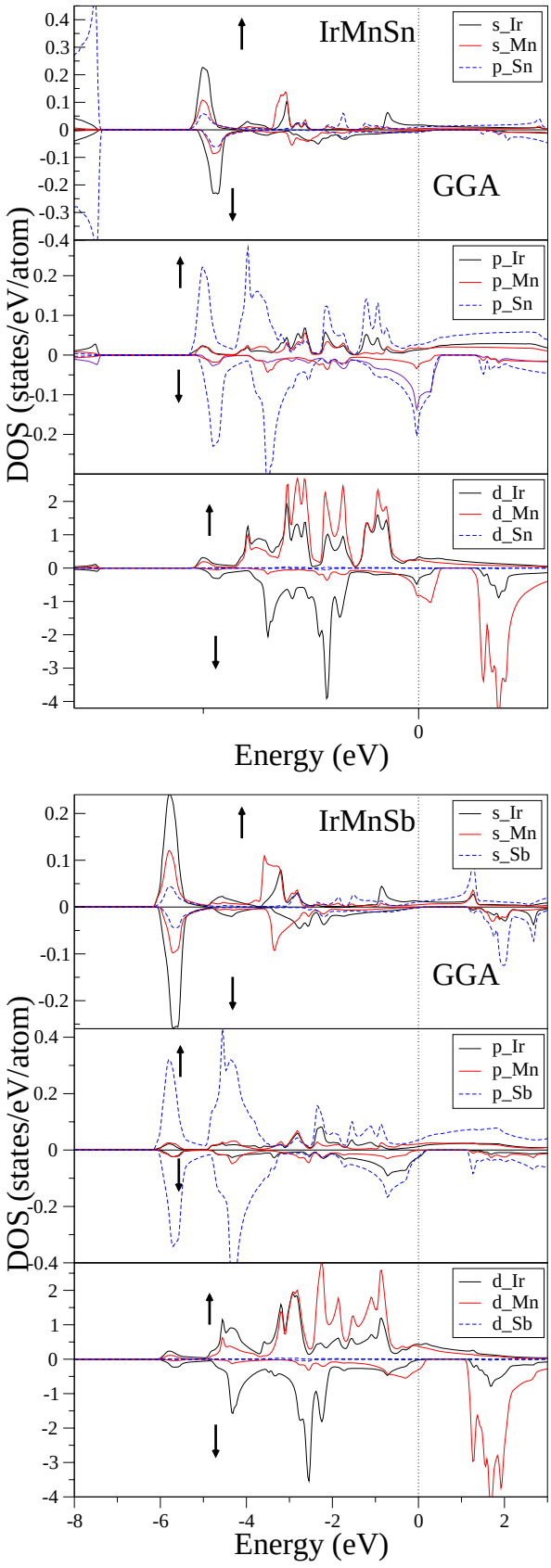

Figure 4.9. Same as in figure 4.8 but for IrMnSn and IrMnSb

Using the optimized structural parameters for half-Heusler IrMnZ compounds, the electronic structure, is calculated by the GGA. The energy band structures are calculated for these compounds along the high-symmetry lines in the fcc Brillouin zone for the majority and minority spins, where ↑ and ↓designate the majority-spin electrons and the minority-spin ones, respectively, as shown in figure 4.2. We note that the spin–orbit coupling is significant for these compounds, since it destroys the half-metallic band gap. The total density of states (TDOS) and the partial DOS (PDOS) are plotted in figures 4.3-9, where the vertical line is the Fermi level (E_F). From the figures, it can be seen that the spin-polarized calculation with the GGA shows that IrMnAl, IrMnSn and IrMnSb are not half-metallic; since IrMnAl IrMnSn show metallic behavior because of the magnitude N(E_F) of the density of states (see Table 4.7) at the Fermi level in both spins up and down. The IrMnSb alloy although it presents a spin-down gap, but it is not half-metallic, since E_F is slightly below the gap.

Table 4.7. *Calculated density of states at the Fermi level (states/eV/atoms) for the IrMnZ compounds.*

		IrMnAl	IrMnSn	IrMnSb
GGA	Up	1.069	0.925	1.114
	Down	1.355	2.315	0.522
GGA+U	Up	0.842	0.740	1.0
	Down	1.647	1.104	1.013
LSDA	Up	2.016	0.740	1.04
	Down	1.963	2.571	0
LSDA+U	Up	0.747	0.703	0.953
	Down	1.336	1.120	0.992

The Fermi level crosses both the majority and minority-spin energy bands, because in these compounds, the repulsive interaction with the non-metal band shifts this band to higher energies above the Fermi level. In contrast to the LSDA which predicts that the IrMnSb is a half-metallic ferromagnet, in this approximation, similar metallic electronic band structures were also predicted IrMnAl and IrMnSn and the DOS for the spin-up and spin down of IrMnAl are nearly identical with small polarization compared to the GGA. In this compound, figure 4.8, the DOS of Mn(Ir) d and Mn(Ir)

p states have nearly the same peaks. This means that there is a significant hybridization between d and p states. Furthermore at the vicinity of the Fermi level the characteristic feature of the electronic structure of IrMnAl alloy is the strong hybridization of Mn 3d and Ir 5d states, the latter being more delocalized due to the hybridization, the nonmagnetic Ir atom in IrMnAl becomes magnetic (see table 4.8).

Table 4.8. *Calculated magnetic moments in μ_B for the IrMnZ compounds.*

		IrMnAl	IrMnSn	IrMnSb
Expt.	Ir	0.015[a]	---	---
	Mn	0.4[b]	2.25 [b]	---
	Z	---	---	---
	Tot.	0.123[a]	---	3.1
GGA	Ir	0.04	0.008	-0.139
	Mn	0.529	3.527	3.337
	Z	-0.002	-0.046	-0.076
	Tot.	0.558	3.628	3.110
GGA+U	Ir	0.174	-0.027	-0.162
	Mn	3.901	4.324	4.210
	Z	-0.046	-0.028	-0.070
	Tot.	4.157	4.522	4.046
LSDA	Ir	-0.002	-0.007	-0.076
	Mn	0.006	3.275	3.161
	Z	0.000	-0.041	-0.051
	Tot.	0.004	3.215	3.010
LSDA+U	Ir	0.170	-0.004	-0.142
	Mn	3.620	4.211	4.020
	Z	-0.03	-0.028	-0.070
	Tot.	3.889	4.445	3.890

[a]Ref. [13], [b]Ref. [33],

As remarked, the density of states indicates that for the LSDA+U (GGA+U) these compounds are still gapless, i.e., metallic phase with a finite Fermi level density of states. The spin down gap in IrMnSb is shifted to higher energies compared to the

standard LSDA (GGA). From the figures 4.6-9, we show also that the d-DOS bonding state peak is shifting towards the lower energy side while the antibonding state peak is shifting towards the higher energy.

Table 4.7 shows the calculated values of the density of states at the Fermi level $N(E_F)$. The results display the same trend, i.e., values of $N(E_F)$ for the spin up and down, for all the approximations used. For IrMnSn, the value of $N(E_F)$ for spin down is larger than the one for spin up, while for the other tow compounds the inverse is observed.

The calculated magnetic moment, independently of the approximation used, is in agreement with the commonly accepted picture of the magnetism of the Mn based Heusler alloys, we obtain a strong localization of the magnetization on the Mn sublattice with a value of the Mn moment near to 4 μB. Table 4.8 summarises the calculated magnetic moments for a series IrMnZ a function of the Z constituent, where Z=Al, Sn and Sb. The induced moment of the Z element is positive in IrMnAl while is negative in IrMnSn and IrMnSb. The induced moments as a function of the Z constituent follow closely the behavior of the Mn moment (increase with increasing Mn moment).

We also find that for the IrMnSb compounds the total moment is about 3.11 μB. Here, the local moment of Mn is higher than the total moment by at most 0.22 μB. The reduction of the total moment is therefore accompanied by negative Ir and Sb spin moments, i.e., these atoms couple antiferromagnetically to the Mn moments. The magnetic moment of the Z atom can be neglected compared to Mn ones.

4.6. MAGNETO-OPTICAL PROPERTIES

The optical properties in the metallic system are generally due to both interband and intraband transitions. In the low-energy regime, the optical transitions can be ascribed to both inter band and intraband transitions. However, in the higher energy regime, the contributions from the interband dominate. For this reason and to give a good accuracy we have calculated both kinds of transitions.

The real and imaginary parts of the diagonal components of optical conductivity tensor, including the intra band contribution, of IrMnZ are presented in Figure 4.10 as a function of photon energy, The lower panels of the figure display the GGA+U results. From these results we note that, in GGA+U there is a dominant peak at almost

the same photon energy between 6 and 6.5eV for both IrMnSn and IrMnSb. This pronounced peak appeared in IrMnAl at about 4 eV in GGA or GGA+U.

Comparatively we note that the $\sigma_{1xx}(\omega)$ is larger than the $\sigma_{2xx}(\omega)$ part in the whole energy range.

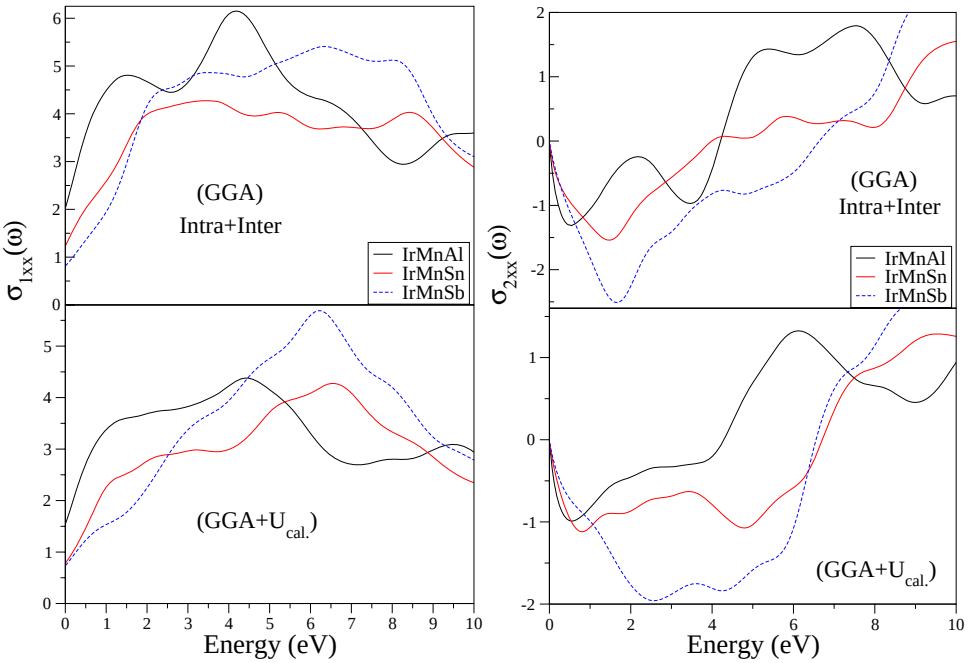

Figure 4.10 Absorptive and dispersive part of the optical conductivity of the diagonal component of the IrMnZ compounds

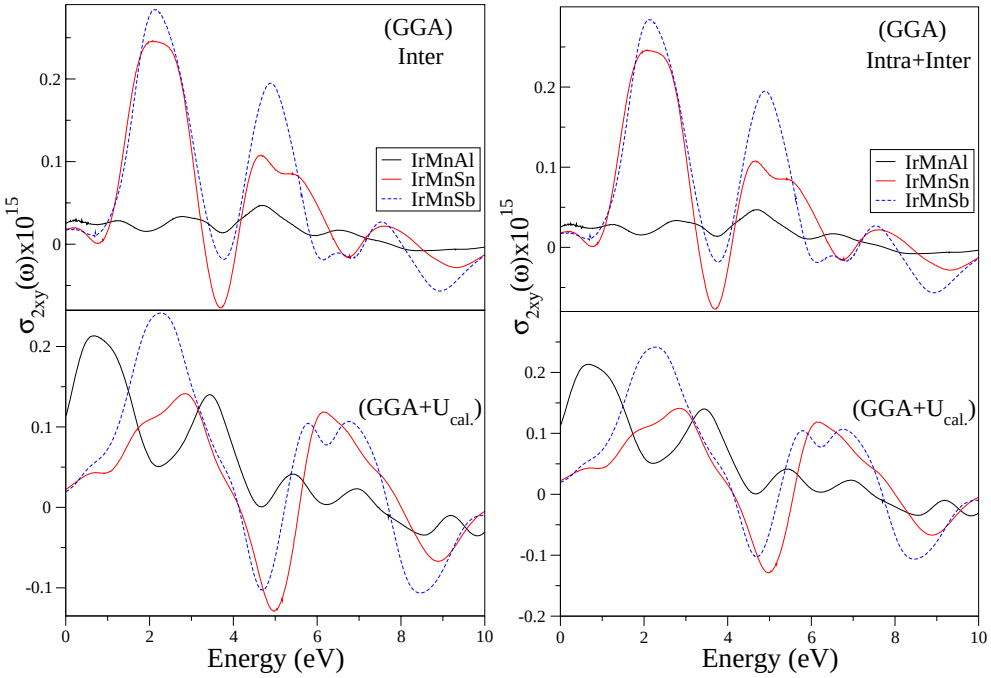

Figure 4.11 Off diagonal component of the conductivity tensor for IrMnZ compound with and without intraband contribution in GGA and GGA+U.

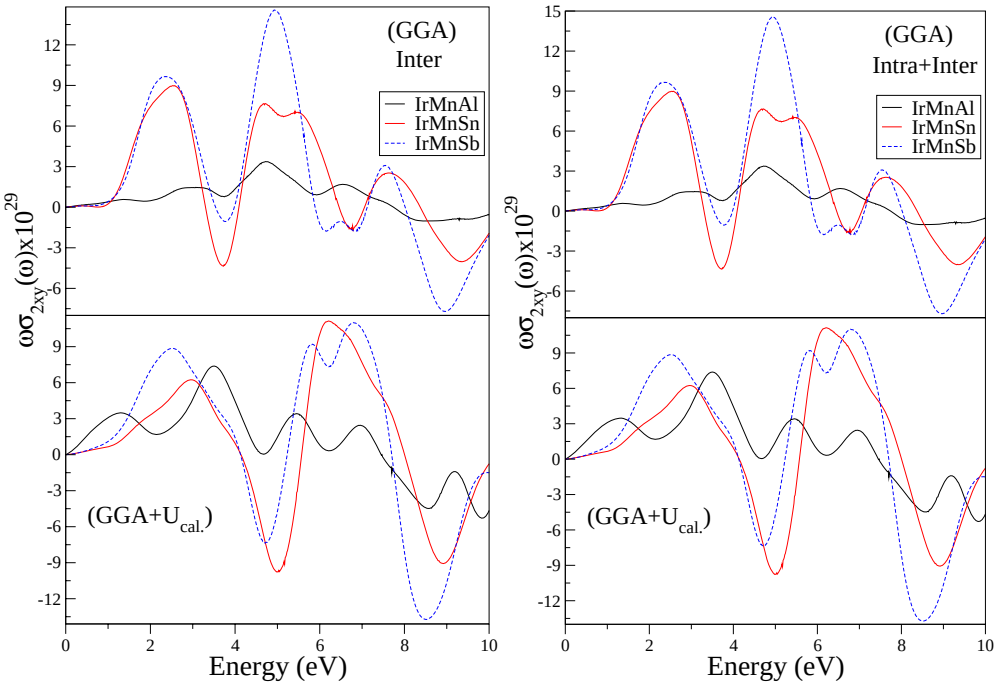

Figure 4.12 Off diagonal component of the conductivity tensor for IrMnZ compounds, multiplied by ω with and without intraband contribution in GGA and GGA+U.

The dispersive part, σ_{2xx} shows a first pronounced peak at 0.5 eV IrMnAl. The same peak can be seen in the IrMnSn and IrMnSb spectra at a slightly higher energy 1.7 and 1.8 eV respectively. This is the main peak observed in our spectral range. While in GGA+U this peak shift to lower energy in IrMnSn. In IrMnSb this peak turned to pronounced structure shifted to the higher energies. In GGA, σ_{2xx} increases above 2 eV with the appearance of the second pronounced peak at 4 eV, in IrMnAl. This peak vanishes in the GGA+U with arising of a pronounced peak at 5.7 eV.

The conductivity can be understood from the density of states. As can be seen from the figure 4.3-6 of the total density, the density of states of IrMnAl and IrMnSn for minority and majority electrons have a large structure above the Fermi energy. Thus the transitions into these unoccupied states from occupied states below the Fermi energy are responsible for structure of the conductivity at low energy which has the same contribution of both spin. While in IrMnSb the majority electron responsible to the transition in this region. Furthermore, in IrMnSn and IrMnSb the trend in the conductivity is almost the same because it has nearly the same electronic configuration. The slightly difference is due to the positions of occupied and unoccupied states. Inspection of the corresponding σ_{1xx} and σ_{2xy} curves shows that the

spin–orbit coupling influences the Kerr rotation spectrum nearly exclusively via σ_{2xy}. While the various curves described above have only a very minor impact of the σ_{1xx} spectrum

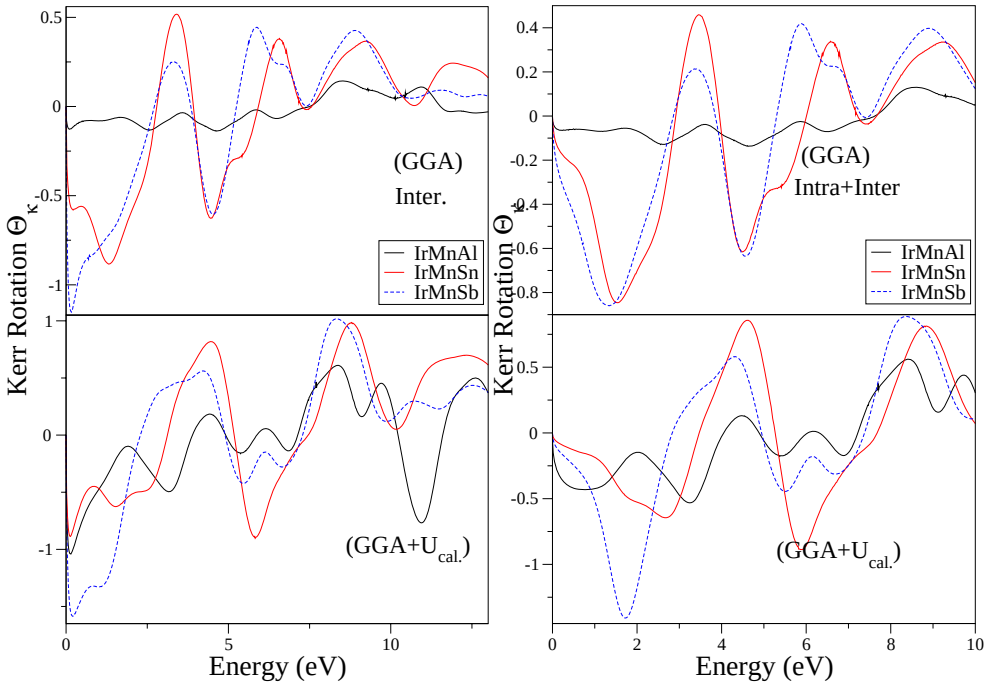

Figure 4.13 Kerr rotation of IrMnZ compounds with and without intraband contribution in GGA and GGA+U.

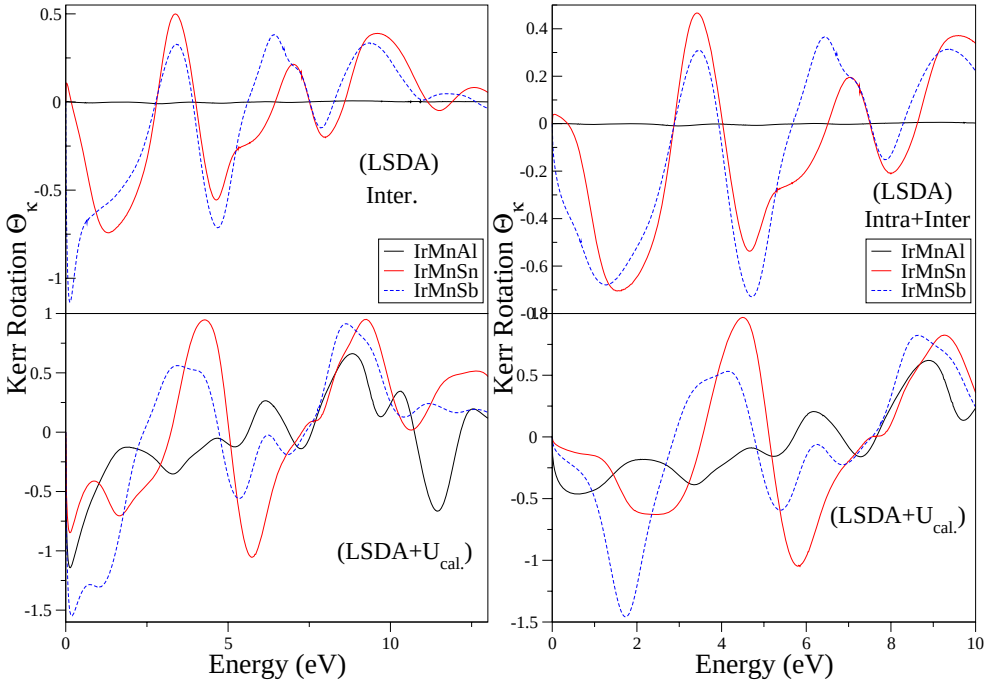

Figure 4.14 Kerr rotation of the IrMnZ compounds with and without intraband contribution with LSDA and LSDA+U.

The absorptive part of the off-diagonal optical conductivity, $\omega\sigma_{2xy}$, has a direct physical interpretation. It is proportional to the difference in absorption rate of left and right circularly polarized light. If we compare $\omega\sigma_{2xy}$ with σ_{1xx} we notice that the transition between 2-2.5 eV also appears in the off-diagonal conductivity. In IrMnSn and IrMnSb $\omega\sigma_{2xy}$ has a large value at 2.2 eV and 5 eV, as shown in figure 4.12, with one shoulder (negative peak) between them at around 4 eV which correlates well with the positive peak in the Kerr rotation spectrum. In contrast to this situation, there are in general some few weaker features found in the whole spectra of IrMnAl.

The polar Kerr rotation spectra are calculated for these compounds, and the results are shown in figure 4.13. We note that it is assumed that the Kerr rotation angle θ_K is directly proportional to the spin–orbit coupling strength and the magnetization or spin-polarization. The largest Kerr rotation is found in IrMnSb and the smallest rotation angle is observed for IrMnAl. This later, and as we have seen previously, has small magnetic moment this leads to a strong reduction of the Kerr rotation and changes in the shape of the spectrum. The magnitude of the Kerr effect is rather small using GGA, reaching a minimum rotation of nearly -0.15° at 8 eV. This value is increased to 0.55° when we use the GGA+U. For the other compounds the spectra for both are very similar, showing a negative Kerr rotation about 0.84° at 1.3 and 0.86 at 1.5 eV in IrMnSn and IrMnSb respectively but when we use GGA+U the amplitude of the Kerr rotation becomes more than twice in IrMnSb than that found in IrMnSn and we notice also a significant shift of the peaks in IrMnSn to the higher energies. Below 6 eV we have other weaker peaks in the Kerr rotation which can be identified as a shoulder in the ellipticity data. There is another weak minimum at 3.8 eV. At higher energies the Kerr rotation goes to zero.

In figures 4.15 and 4.16 it is seen that the calculated ellipticity spectra for IrMnSb and IrMnSn are very similarly to each other. It is clearly seen that when the Kerr ellipticity crosses the zero line, a peak always appears in the Kerr rotation spectra and vice versa due to the Kramers-Kronig relations.

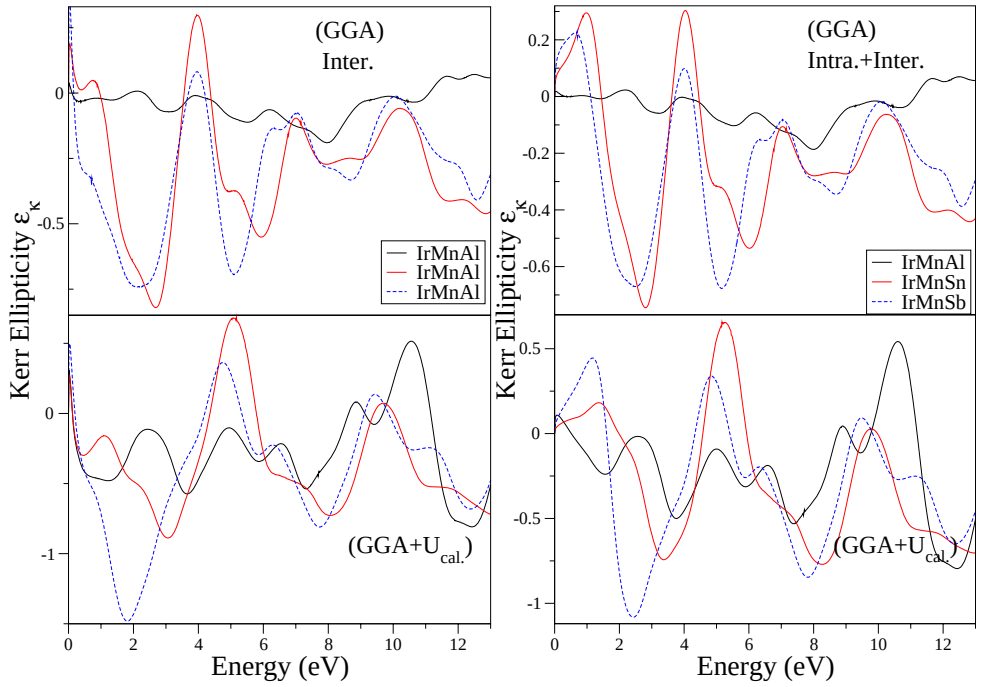

Figure 4.15 Kerr ellipticity of the IrMnZ compounds with and without intraband contribution in GGA and GGA+U.

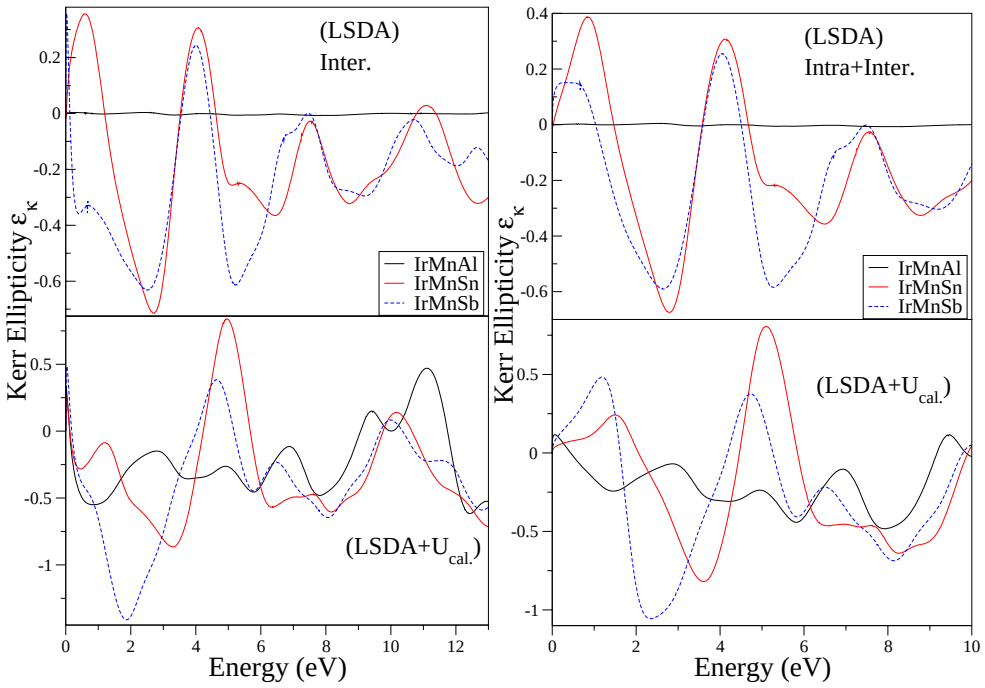

Figure 4.16 Kerr ellipticity of IrMnZ compounds with and without intraband contribution in LSDA and LSDA+U.

4.7. CONCLUSION

We have calculated the structural, elastic, electronic and magneto-optical properties of the half-Heusler compounds IrMnZ (Z = Al, Sn and Sb) by means of the full potential linearized augmented plane wave plus local orbitals, FP-LAPW+LO, method within the generalized gradient approximation. We have also calculated the shear modulus, Young's moduli, and Poisson's ratio, for polycrystalline IrMnZ. The results show that IrMnAl are metallic and ferromagnetic. They are mechanically stable at zero pressure and possess the highest bulk, shear and Young's modulus, the sound velocities and the Debye temperatures are derived for the IrMnZ compounds.
We have also applied the LSDA+U(GGA+U) functional as adapted to the linearized augmented plane wave method. The inclusion of Coulomb interaction in d states mainly changes the bottom of the conduction band by upward energy shifting from original position due to Hubbard U_d, i.e. shift unoccupied bands up and occupied bands down.

We also find that in these compounds, the local moment of Mn is higher than the total moment. The reduction of the total moment is therefore accompanied by negative in Ir or in Z elements or in both, i.e., these atoms couple antiferromagnetically to the Mn moments. The hybridization between Ir and Mn is considerably larger.

The local spin density approximation (LSDA) predict that the IrMnAl have negligible magnetic moment. Furthermore, they predict that IrMnSb is a half metallic. While the LSDA+U (GGA+U) predict a large magnetic moment comparing to the experimental ones. Our results predict that the spin–orbit coupling is significant for these compounds, since they destroy the half-metallic band gap.

We found the highest Kerr rotation at IrMnSb compound with weak values in IrMnAl in all the approximations used. The quite large Kerr rotation near 2.0 eV, in IrMnSb compound, would find possible applications of this compound in the infrared laser light magneto-optical effect devices.

REFERENCE

1- P. Bach, A.S. Bader, C. Rüster, C. Gould, C.R. Becker, G. Schmidt, L.W. Molenkamp, W.Weigand, C. Kumpf, E. Umbach, R. Urban, G.Woltersdorf, B. Heinrich, Appl. Phys. Lett. 83, (2003) 521.

2- K. Aoshima, N. Funabashi, K. Machida, Y. Miyamoto, K. Kuga, N. Kawamura, J. Magn. Magn. Mater. 310, (2007) 2018.

3- L.J. Singh, C.W. Leung, C. Bell, J.L. Prieto, Z.H. Barber, J. Appl. Phys. 100, (2006) 13910.

4- R.B. Helmholdt, R.A. de Groot, F.M. Mueller, P.G. Van Engen, K.H.J. Buschow, J. Magn. Magn. Mater. 43, (1984) 249

5- P. Turban, S. Andrieu, B. Kierren, E. Snoeck, C. Teodorescu, A. Traverse, Phys. Rev. B 65, (2002) 134417.

6- J. Giapintzakis, C. Grigorescu, A. Klini, A. Manousaki, V. Zorba, J. Androulakis, Appl. Phys. Lett. 80, (2002) 2716.

7- K.E.H.M. Hanssen, P.E. Mijnarends, Phys. Rev. B 34 (1986) 5009.

8- I. Galanakis, J. Phys. Condens. Matter 14, (2002) 6329.

9- G.A. deWijs, R.A. de Groot, Phys. Rev. B 64, (2001) 20402.

10- D. Brown, M.D. Crapper, K.H. Bedwell, M.T. Butterfield, S.J. Guilfoyle, A.E.R. Malins, M. Petty, Phys. Rev. B 57, (1998) 1563.

11- S. Plogmann, T. Schlatholter, J. Braun, M. Neumann, Yu.M. Yarmoshenko, M.V. Yablonskikh, E.I. Shreder, E.Z. Kurmaev, A. Wrona, A. Slebarski, Phys. Rev. B 60, (1999) 6428.

12- H. Masumoto, K.Watanabe, J. Phys. Soc. Jpn. 32, (1972) 281.

13- V.V. Krishnamurthy, N. Kawamura, M. Suzuki, T. Ishikawa, G.J. Mankey, P. Raj, A. Sathyamoorthy, A.G. Joshi, S.K. Malik, Phys. Rev. B 68, (2003) 214413.

14- I. Galanakis, Phys. Rev. B 71, (2005) 12413.

15- V.N. Antonov, B.N. Harmon, A.N. Yaresko, L.V. Bekenov, A.P. Shpak, Phys. Rev. B 73, (2006) 94445.

16- D.J. Singh, Planes Waves, Pseudo-potentials and the LAPW Method, Kluwer Academic Publishers, Boston, Dortrecht, London, 1994.

17- P. Blaha, K. Schwarz, G.K.H. Madsen, D. Hvasnicka, J. Luitz, WIEN2k, An Augmented PlaneWave+Local Orbitals Program for Calculating Crystal

Properties, Karlheinz Schwarz, Techn. Universit Wien, Austria, 2001, ISBN: 3-9501031-1-2.

18- P. Hohenberg,W. Kohn, Phys. Rev. 136, (1964) 864.

19- W. Kohn, L.J. Sham, Phys. Rev. 140, (1965) 1113.

20- J.P. Perdew, S. Burke, M. Ernzerhof, Phys. Rev. Lett. 77, (1996) 3865.

21- S.-H.Wei, Phys. Rev. Lett. 56, (1986) 528.

22- L. Offernes, P. Ravindran, A. Kjekshus, J. Alloys Compd. 439, (2007) 37.

23- S.-H.Wei, Phys. Rev. Lett. 56, (1986) 528.

24- F.D. Murnaghan, Proc. Natl. Acad. Sci. U.S.A. 30, (1944) 244.

25- B.B. Karki, G.J. Ackland, J. Crain, J. Phys. Condens. Matter 9 (1997) 8579.

26- O. Beckstein, J.E. Klepeis, G.L.W. Hart, O. Pankratov, Phys. Rev. B 63, (2001) 134112.

27- Z. Suna, S. Li, R. Ahujab, J.M. Schneider, Solid State Commun. 129, (2004) 589.

28- D. Iotova, N. Kioussis, J.B. Lanco, S.P. Lim, R. Wu, in: A. Gonis, A. Meike, P.E.A. Turchi (Eds.), Properties of Complex Inorganic Solids, Plenum Press, New York, 1997.

29- R. Hill, Proc. Phys. Soc. Lond. 65, (1953) 909.

30- Y.-J. Hao, X.-R. Chen, H.-L. Cui, Y.-L. Bai, Physica B 382 (2006) 118.

31- Y.O. Ciftci, K. Colakoglu, E. Deligoz, H. Ozissk, Mater. Chem. Phys. 108 (2008) 120.

32- V. I. Anisimov, F. Aryasetiawan, and A. Lichtenstein, J. Phys. Condens. Matter 9, (1997) 767

33- H. Masumoto, K.Watanabe, J. Phys. Soc. Jpn. 32, (1972) 281.

Chapter: 05

Results and Discussion

HEUSLER ALLOYS PdMnSb and Pd_2MnSb

5.1. INTRODUCTION

Mn-based Heusler alloys of the formula XMnSb, belong to a class with interesting magnetic properties, exhibiting ferromagnetic features like magneto-optical effects and giant magneto-resistance. Their electronic structure can range from metallic to half metallic. The electronic structure, magnetic and magneto optical properties of various XMnSb compounds have been reported [1-3] and showing that many of them can be used in technological applications such as magnetic tunnel junctions [4] and also as giant magneto resistance spin valves [5].

For XMnSb (X = Pt. Pd, Ni) and especially PdMnSb, there are several works on these compounds. Kang et al.[6] have investigated the electronic structures of the valence band and Sb 4d core levels of these Heusler alloys using photoemission spectroscopy (PES) and self-consistent spin-polarized band structure calculations (LMTO band calculations). Moreover the magneto-optical properties have been investigated experimentally and theoretically [7-8]. The compact structure of this compound is the full Heusler alloy Pd_2MnSb. The magnetic and crystallographic structure of this alloy was investigated in detail by Webster and Tebble [9] and recently the complex impedance measurements on polycrystalline samples of Pd_2MnSb were reported as function of temperature and external magnetic field [10]. Furthermore, the hyperfine field at the antimony site in Pd_2MnSb is one of the largest [11,12]

5.2. *DETAILS OF CALCULATIONS*

The crystal structure of (half Heusler) PdMnSb alloys is a $C1_b$ structure, space group $F\bar{4}3m$ (No. 116). The Pd_2MnSb (full Heusler) compound has a cubic $L2_1$ structure with the space group $Fm3m$ (No. 225). This is a close packed complex face-centred cubic structure.

The lack of information on the electronic structure of these compounds has motivated us to perform first-principles calculations of the magneto-optical properties by using the full-potential linearized augmented plane wave plus local orbitals method (FP-LAPW+LO). Wave functions, charge density, and potential are expanded in spherical harmonics within non-overlapping atomic spheres of radius R_{MT} and in plane waves in the remaining space of the unit cell (interstitial region). The basis set is split into core and valence parts. Local orbitals were used, as implemented in the WIEN2k package, to treat some semi-core states with the valence states in a single-energy window.

The Kohn-Sham equations were solved within the local-spin-density approximation (LSDA) [13], and also within the generalized-gradient approximation (GGA) [14]. The relativistic effects were treated within the scalar relativistic approximation but we have

checked the influence of spin–orbit coupling. The spin-orbit coupling (SOC) is taken into account by using the second-variation method self-consistently [15-17], without including the $p_{1/2}$ local orbital corrections. In our calculations, the magnetization is taken along (001) direction for the structures when the SOC is included. For the Brillouin zone (BZ) integration, a modified tetrahedron method [18] with 403 special k points in the irreducible wedge (IW) (3000 k points in the full BZ) was used in constructing the charge density in each self-consistency step. We have carefully checked that with these parameters the calculations converge.

The correlated d-electron states of Pd and Mn are taken into account by using the LSDA+U (GGA+U) methods with self-interaction correction method (SIC) to account the double-counting corrections. The meaning of the U parameter was discussed by Anisimov and Gunnarsson [19]. In this work we take, the polar Kerr effect which is given by the well-known formula for the complex Kerr angle (see chapter 1)

The calculation of the optical and magneto-optical properties has been performed using 8000 k-points with 20×20×20 k mesh. In order to consider the effect of finite lifetimes, as well as of the experimental resolution, a Lorentzian broadening equal to δ_L= 0.7 eV was applied for both the interband and intraband contributions and Drude broadening equal to δ_D= 0.1 eV in the intraband contributions. We have used also Lorentzian broadening equal to δ_L= 0.1 eV in some cases to distinguished between the spin up and spin down contributions.

5.3. STRUCTURAL PROPERTIES

The optimized lattice constant *a* (Å), the bulk modulus B (GPa) and the corresponding experimental data are listed in Table 5.1 using the different approximations. The calculated values of U for Pd and Mn atoms are displayed in table 5.2. The results show that the GGA gives closed parameters compared to experiment and the LSDA+U provides a better estimate of the lattice constants than the LSDA. Furthermore, the lattice constant is severely over estimated by GGA+U. The value of bulk modulus is inversely proportional to the lattice parameter one (volume effect) and there are no experimental data to compare our predicted results with them. But, one can conclude that the GGA describes more accurately the structural properties than the other approximations as far as the lattice parameter is concerned. The calculated values of U are obtained using the method of Anisimov, but there are other methods to estimate the value of U. These facts stimulated us to take into account the correlation effects of the d electrons for different values of U. The results used for U varying from 1 to 6 eV, the latter value is probably an upper limit for Mn in an intermetallic compounds, are reported in table 5.3. It appears from the comparison of the calculated results with the experimental ones that the GGA+U (U=1) gives better results and the LSDA+U with U=6 but with a lesser extent.

Table 5.1 *Calculated and experimental lattice constants and bulk modulus of PdMnSb and Pd_2MnSb compounds.*

	LSDA		LSDA+$U_{cal.}$		GGA		GGA+$U_{cal.}$		$a_{Exp.}$
	a(A°)	*B*(GPa)	*a*(A°)	*B*(GPa)	*a*(A°)	*B*(GPa)	*a*(A°)	*B*(GPa)	
PdMnSb	6,06	129.29	6.165	114.26	6.247	93.78	6.35	89.16	6.28
Pd_2MnSb	6.304	166.7	6.373	149.22	6.465	136.43	6.532	123.65	6.42

Table 5.2 *Calculated U parameters for the PdMnSb and Pd_2MnSb compounds.*

	LSDA		GGA	
	U(Pd)	*U(Mn)*	*U(Pd)*	*U(Mn)*
PdMnSb	0.3	3.8	0.4	3.5
Pd_2MnSb	0.3	3.8	0.39	3.53

Table 5.3 *Dependence of the lattice parameter on the U parameter for the for the PdMnSb and Pd_2MnSb compounds.*

		U=1	U=2	U=3	U=4	U=5	U=6
GGA	PdMnSb	6.270	6.299	6.334	6.355	6.37	6.38
	Pd_2MnSb	6.482	6.504	6.522	6.54	6.55	6.563
LSDA	PdMnSb	6.08	6.119	6.146	6.168	6.186	6.2
	Pd_2MnSb	6.321	6.34	6.357	6.364	6.373	6.38

5.4. ELECTRONIC PROPERTIES

In this section, we present our calculated band structure for PdMnSb and Pd_2MnSb compounds using different approximations and taking into account the spin-orbit interaction. We also present our studies of the electronic structure for different values of U, due to its effects on the magnetic and magneto-optical properties. Furthermore, our discussion will be focussed on the LSDA results, but for comparison we present our GGA ones.

The band structures for spin up and down electrons at the high symmetry points as well as in the lines joining them in the Brillouin zone are shown in figures 5.1a and 5.1b for PdMnSb and Pd2MnSb using the LSDA and LSDA+$U_{cal.}$. The LSDA spin polarized calculations predict that PdMnSb is half metallic and Pd_2MnSb is metallic, while the LSDA+U_{cal} destroys the half metallicity for the first compound and gives the same nature as the LSDA for the second one.

The band structure calculation using the LSDA are very similar to those obtained using GGA, except around the Fermi level for the spin down electrons where smaller changes appear (see figure 5.2).

The band structure with spin-orbit coupling (SO) demonstrates that SO effect is significant for this compound, whereas the introduction of this effect split the bands and destroys the half-metallic band gap because the spin-orbit coupling introduce states in the half-metallic gap of the minority states (spin-down direction).

We find it very convenient for the comparison to present our results in the same figure. Figure 5.2 displays the spin polarized density of states (DOS) of the PdMnSb and Pd2MnSb compounds using different approximations, i.e., LSDA, GGA, LSDA+U_{cal} and GGA+U_{cal}. The difference between these results is a clear manifestation of the differences in the band structures using the different approximations.

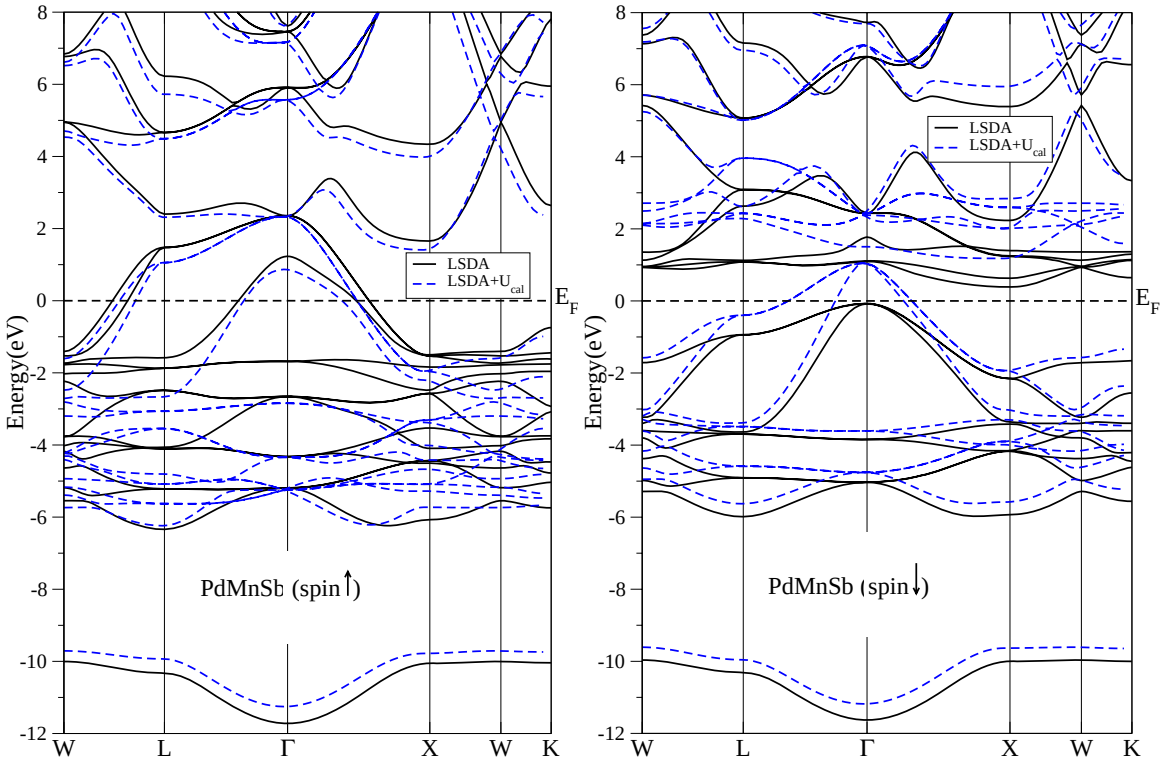

Figure 5.1a Band structure of PdMnSb along the high cubic symmetry lines in Brillouin zone using the LSDA and the LSDA+U.

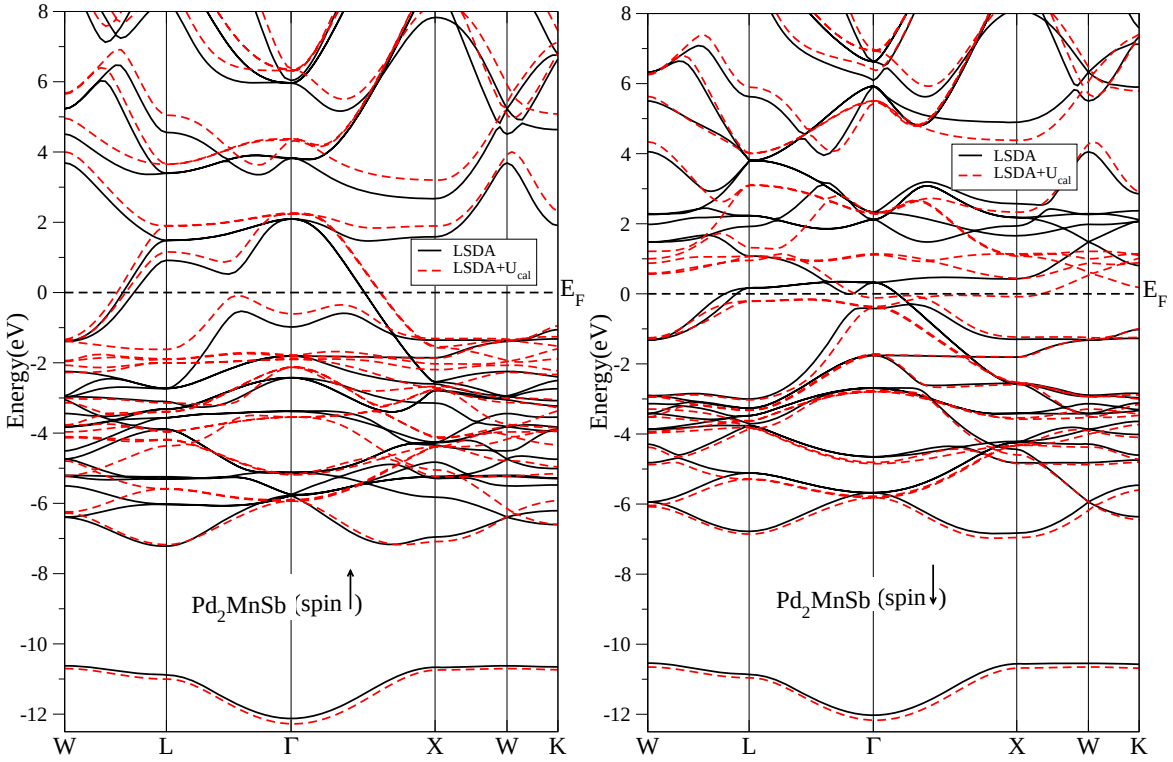

Figure 5.1b Band structure of Pd_2MnSb along the high cubic symmetry lines in Brillouin zone using the using the LSDA and the LSDA+U.

For PdMnSb (with LSDA), the Fermi level is very close to the edge of the gap (thus it is a half metal), in contrast to the LSDA+U where it is below the gap. The majority spin density of states has a metallic character, and the number of electronic states at the Fermi level is 0.68 sates/eV/cell. The minority spin present occupied and unoccupied states obviously separated by a gap.

The value of the gap in the minority band of PdMnSb is approximately 0.45 and 0.13 eV, for LSDA and LSDA+U, respectively, which is an indirect gap, with the maximum of the valence at the Γ points and the minimum of the conduction band at the X-point.

Figure 5.3, gives the projected density of states of the atoms. In the majority (spin ↑) band the Mn d states are shifted to lower energies and form a common d band with the Pd d states, while in the minority band (spin ↓) the Mn states are shifted to higher energies and are unoccupied, so that the band gap at E_F is formed separating the occupied d bonding from the unoccupied d-type antibonding states.

The projected densities of states (PDOS) shows that the Sb atom with the sp atomic configuration introduces a deep lying s band located at about -12 eV and the p-bands between 0-2 eV below the Fermi level.

The bonding hybrids are mostly a mixture of Pd and Mn character, while the antibounding empty ones have mostly Mn character with a small mixture of Pd states. In the LSDA+U the DOS peaks in the neighbourhood of E_F due the Mn atom in the majority spin, observed in the LSDA, are shifted to lower energies, resulting in the suppression of these peaks in the total DOS (see figure 5.2) while in the minority spin the structures located above the Fermi level are shifted to higher energies. Furthermore, in this case the bonding hybrids are mostly of Pd character with a small Mn mixture but for the antibonding states we have the same behaviour, i.e., the dominance of the Mn d states.

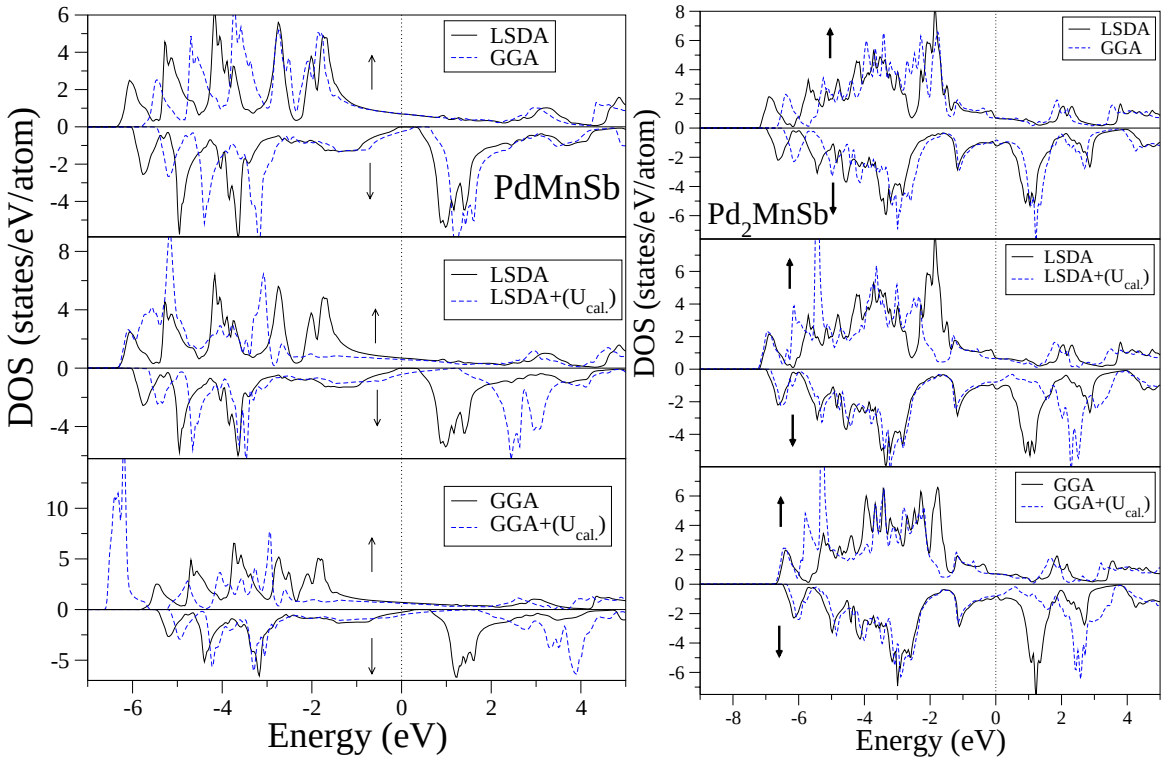

Figure 5.2 The total density of states DOS with LSDA (LSDA+U) and GGA (GGA+U) of the PdMnSb compound.

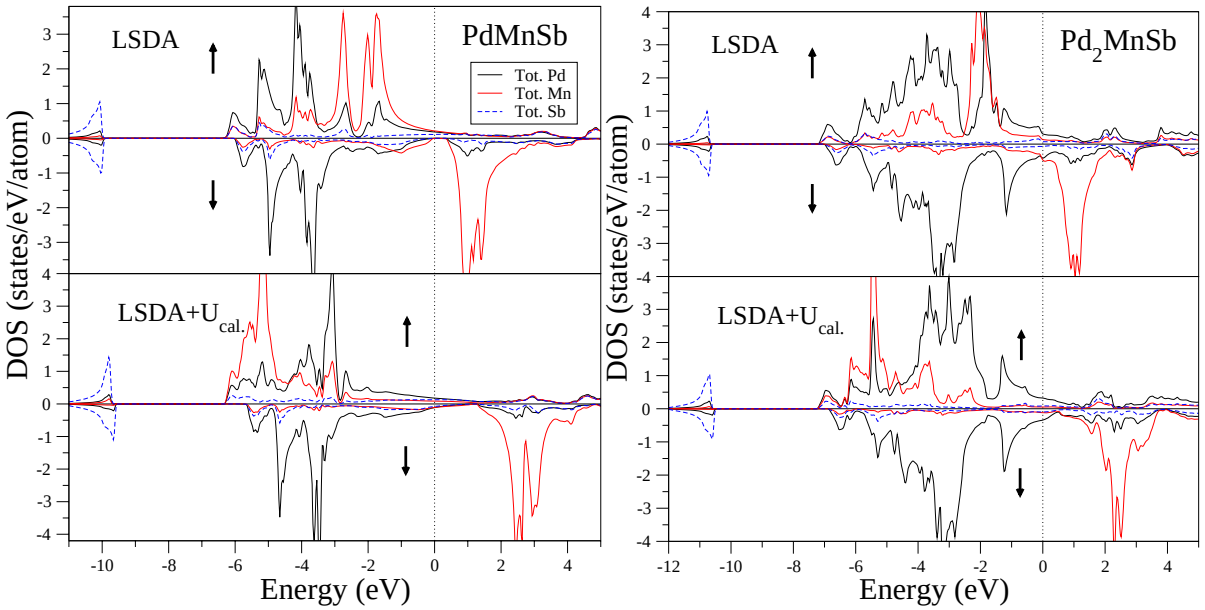

Figure 5.3 The total density of states (DOS) per atom of *Pd*, Mn and Sb species with LSDA and LSDA+U_{cal}.

As it is seen from the figure 5.4 the density of states depends strongly on the U used. The inclusion of Coulomb interaction in d states mainly changes the top of the valance density by shifting the peaks to lower energies from original position and the bottom of the conduction band by upward energy shifting from original position. We note that this effect is very strong in PdMnSb than Pd_2MnSb compounds.

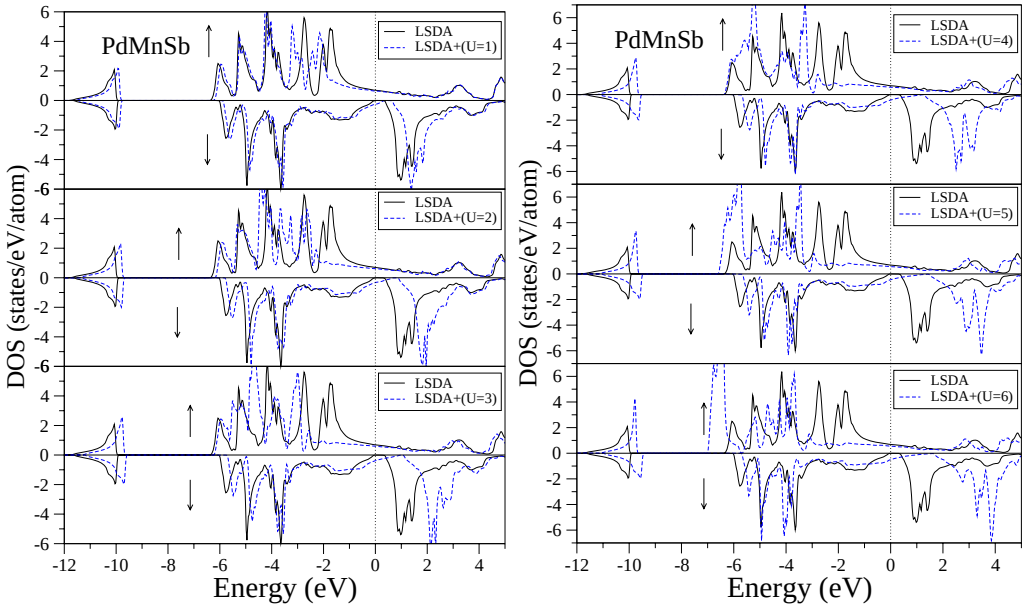

Figure 5.4a Dependence of the total density of states (DOS) on the value of U for PdMnSb.

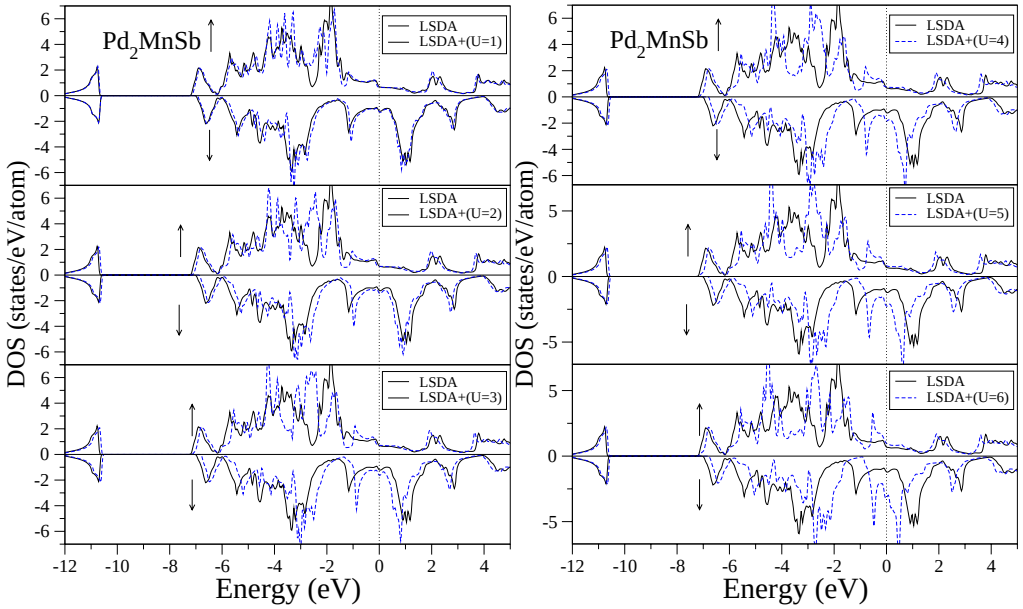

Figure 5.4b Dependence of the total density of states (DOS) on the value of U for Pd_2MnSb.

In agreement with the commonly accepted picture of the magnetism of the Mn based Heusler alloys, we obtain a strong localization of the magnetization on the Mn sublattice with a value of the Mn moment around $4\mu_B$. We find that the spin contribution of the Mn atom to the total magnetic moment is large. Table 5.4 summarises the calculated magnetic moments for the different approximations LSDA, GGA, LSDA+U and GGA+U for U calculated and when this parameter extends from 1 to 6 eV. The total magnetic moment per unit cell is located mostly at the Mn atom. The local moment of Mn is higher than the total moment by at most 0.01-0.05 μB. In contrast with IrMnZ compounds, see chapter 4, where the difference goes to more than 0.22 μ_B. The reduction of the total moment is therefore accompanied by negative Sb spin moments. This is induced by the hybridization of Sb-p states with Mn-3d states. Furthermore, the magnetic moment in Mn in Pd_2MnSb compound is lower than the total magnetic moment.

Table 5.4 *Dependence of the magnetic moment on the U parameter for the PdMnSb and Pd_2MnSb compounds. The values between brackets represent the magnetic moment in Mn atom.*

		SA	$U_{cal.}$	U=1	U=2	U=3	U=4	U=5	U=6	Exp
GGA	PdMnSb	4.086 (4.02)	4.637 (4.68)	4.202 (4.21)	4.358 (4.40)	4.461 (4.51)	4.517 (4.60)	4.632 (4.68)	4.66 (4.72)	4.0[a] (3.95)[b]
	Pd_2MnSb	4.316 (3.99)	4.664 (4.43)	4.442 (4.25)	4.544 (4.39)	4.617 (4.34)	4.722 (4.60)	4.767 (4.66)	4.784 (4.60)	4.4[c] (4.2)[c]
LSDA	PdMnSb	4.01 (3.78)	4.456 (4.46)	4.09 (3.99)	4.253 (4.18)	4.360 (4.33)	4.461 (4.44)	4.545 (4.52)	4.63 (4.64)	
	Pd_2MnSb	4.178 (3.79)	4.616 (4.35)	4.333 (4.00)	4.462 (4.16)	4.563 (4.29)	4.644 (4.39)	4.682 (4.46)	4.752 (4.62)	

[a] Ref. [20]; [b] Ref. [21], [c] Ref. [22]

SA: standard approximation

5.5. OPTICAL AND MAGNETO-OPTECAL PROPERTIES

In this section we present first our calculated results for the optical and magneto optical properties for the half Heusler alloys PdMnSb for which the experimental data are available and reported in Ref. [23] and discuss them, then the predicted results for Pd2MnSb will be given.

The calculated imaginary part of the dielectric function which represents a way to assess how energy is taken when an electromagnetic wave interacts with a material medium, is shown in figure 5.5 using different approximations, together with the measured spectrum for PdMnSb. The calculated spectra are the sum of the both intra and inter contributions. In the Drude term, the phenomenological life time, δ, is 0.1 eV. First, the agreement between the two computational approaches is rather good. Second, the LSDA+U_{cal} gives better agreement with experimental, i.e., the experimental trend is reasonably reproduced.

In order to give a complete description of the origin of the different peaks and structures in the spectra, first we decompose ε_2 into spin up and spin down, with and without intraband

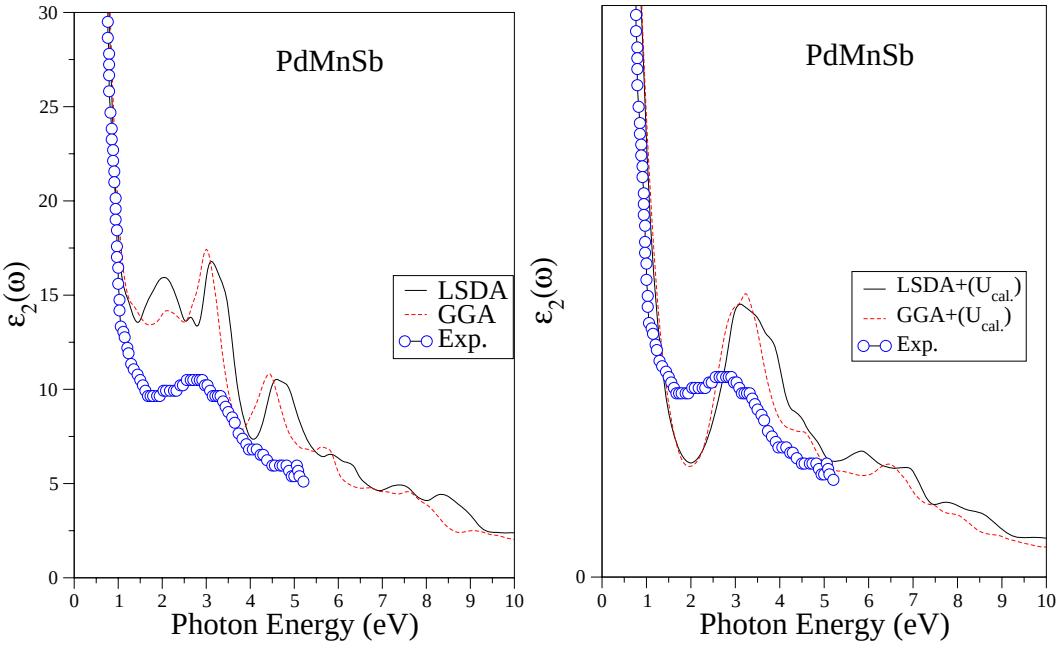

Figure 5.5 Calculated and experimental [23] imaginary part of the dielectric function of the PdMnSb compound. The Lorentzian broadening is equal to δ_L= 0.1 eV.

transitions, in doing so we neglect the spin orbit interaction and the results are given in figure 5.6. Secondly, we perform the decomposition of ε_2 into individual pair contribution in figure 5.7. The band structure for PdMnSb is displayed in figure 5.8.

From the interband curve of ε_2 (figure 5.6), it is clear that for $0<\eta\omega<1.1$ eV the spectrum closely resembles the contribution from the metallic channel and the peak at 0.4 eV is produced by the spin up transition. At higher energies the spectra follow the semiconducting channel. Furthermore, when the intraband contribution is added, it dominates the lower energy behaviour of the ε_2, but the same trend is conserved at higher energies. After the regular decrease due to the intra contribution, three prominent peaks follow at 1, 3.4 and 4.8

eV with minimum in between. The first peak is due to transitions 2-3 and 2-4 from spin down bands, the second is caused by the transition 1-6 with a contribution of the 4-5 one from the spin up and the third one results from transition from the band 2 to the band 8 of the spin down. In the LSDA+U_{cal}, the first minimum in the calculated spectra is located around 2 eV. The minimum in measured spectra is at lower energy, is due mainly to transition in the spin down channel and the main peak at 3.4 is caused by transition in the spin up channel.

We have also studied the influence of U on ε_2 for U varying from 1 to 6 eV and the results are given in figures 5.9. We note that the results for U= 3 are close to the experiment data. Bearing in mind that this values is close to the one calculated. The real part of dielectric function ε_1 is obtained from imaginary part by the Kramer-Kronig relation and is shown in figures 5.10.

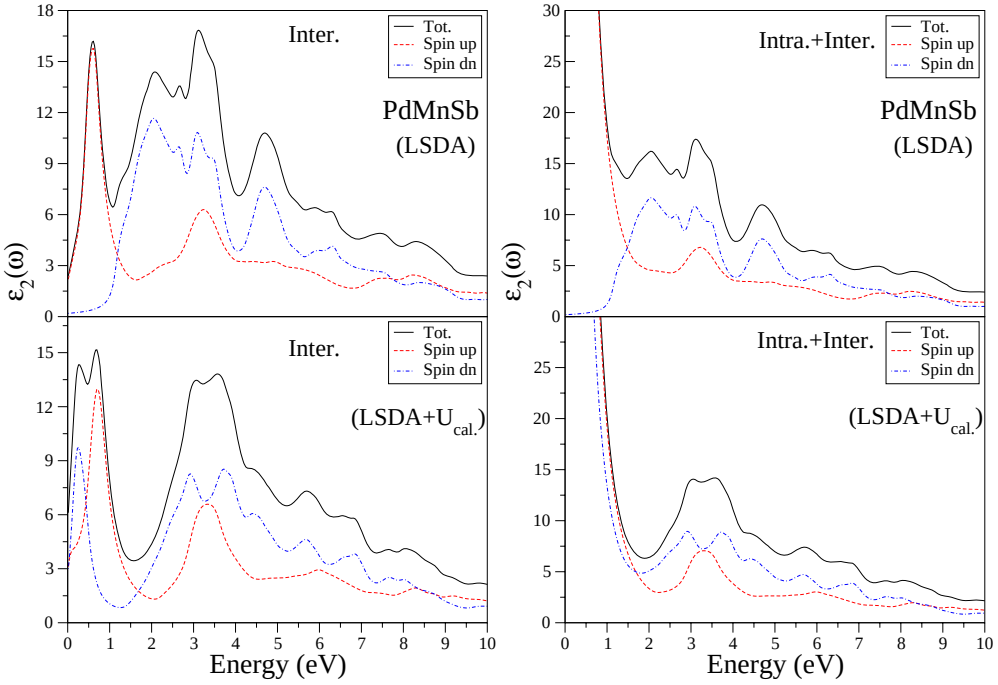

Figure 5.6 Spin decomposition of the imaginary part of the dielectric tensor of PdMnSb compound. The total dependence is shown by the solid line, spin-majority contribution by the dotted line (red color), and spin-minority contribution by the dashed line (bleu colour).

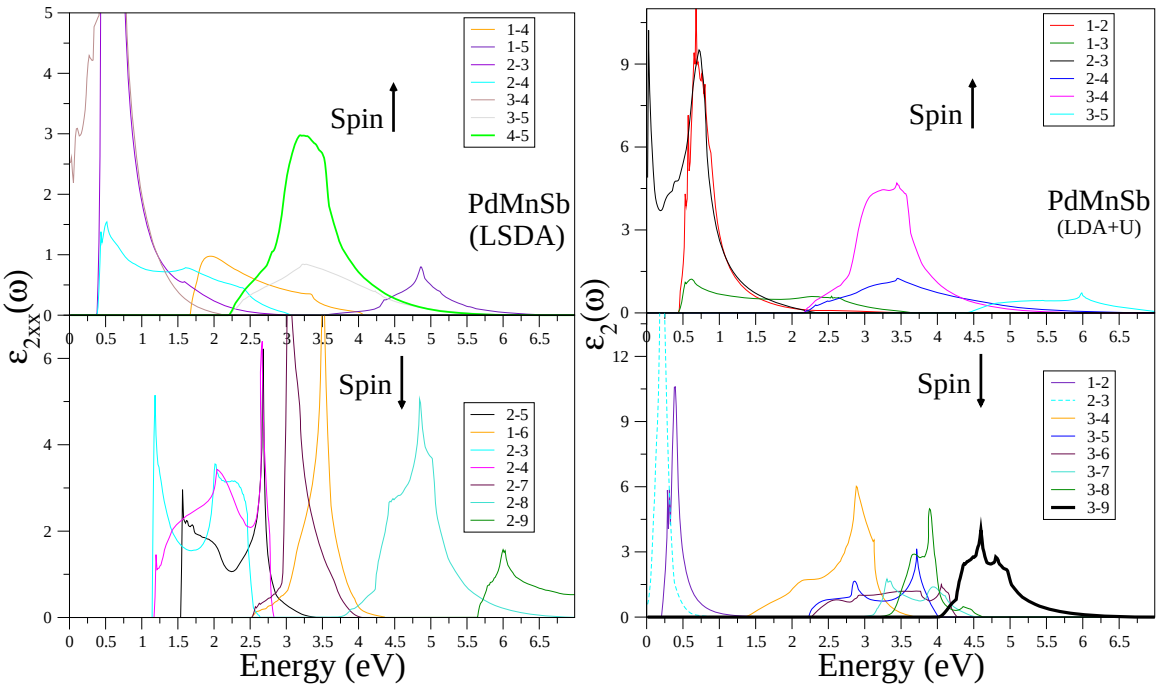

Figure 5.7 The decomposition of the imaginary part of the dielectric function of PdMnSb compound with LSDA and LSDA+U.

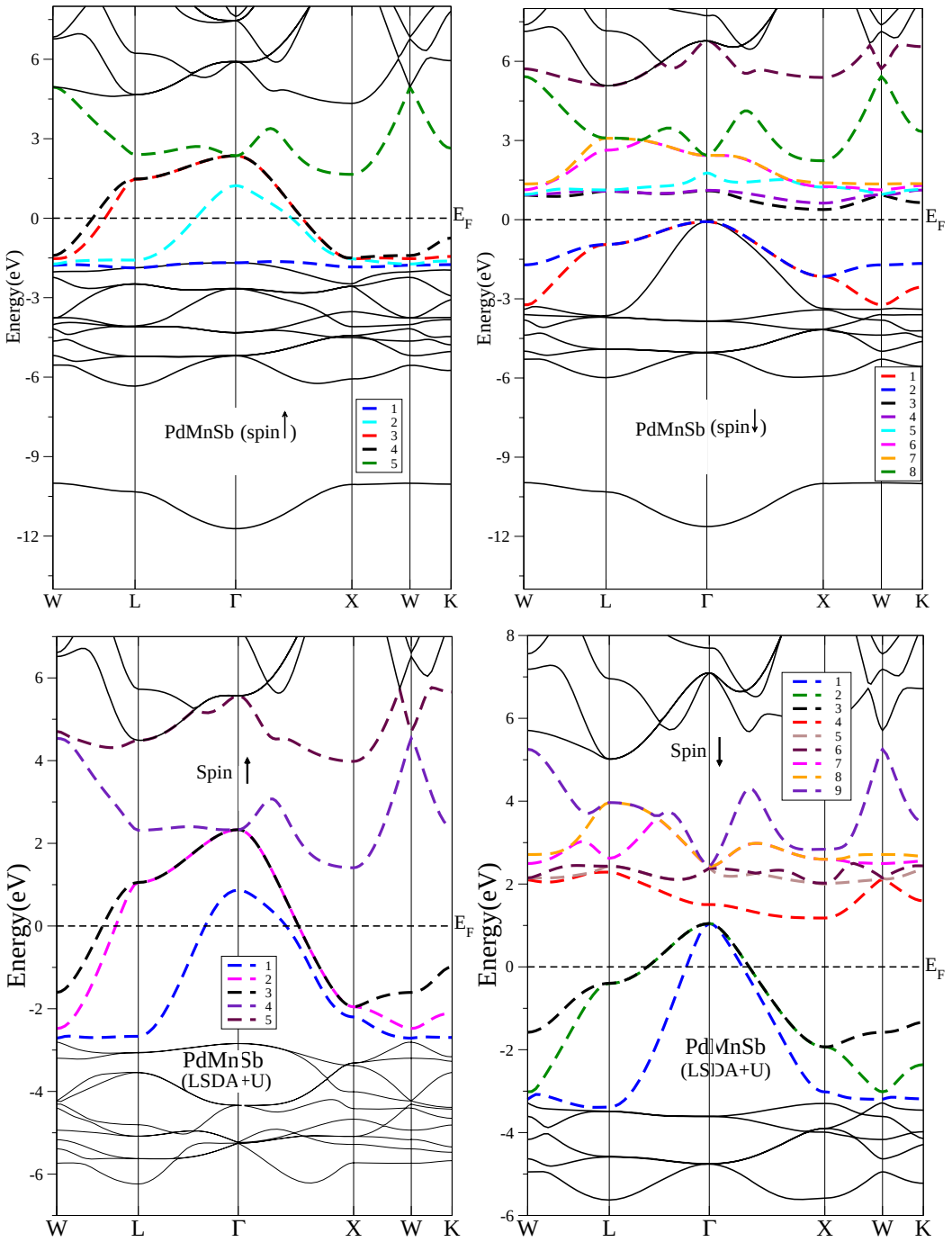

Figure 5.8 the band which contributed to the interband transition of PdMnSb compound with LSDA and LSDA+U.

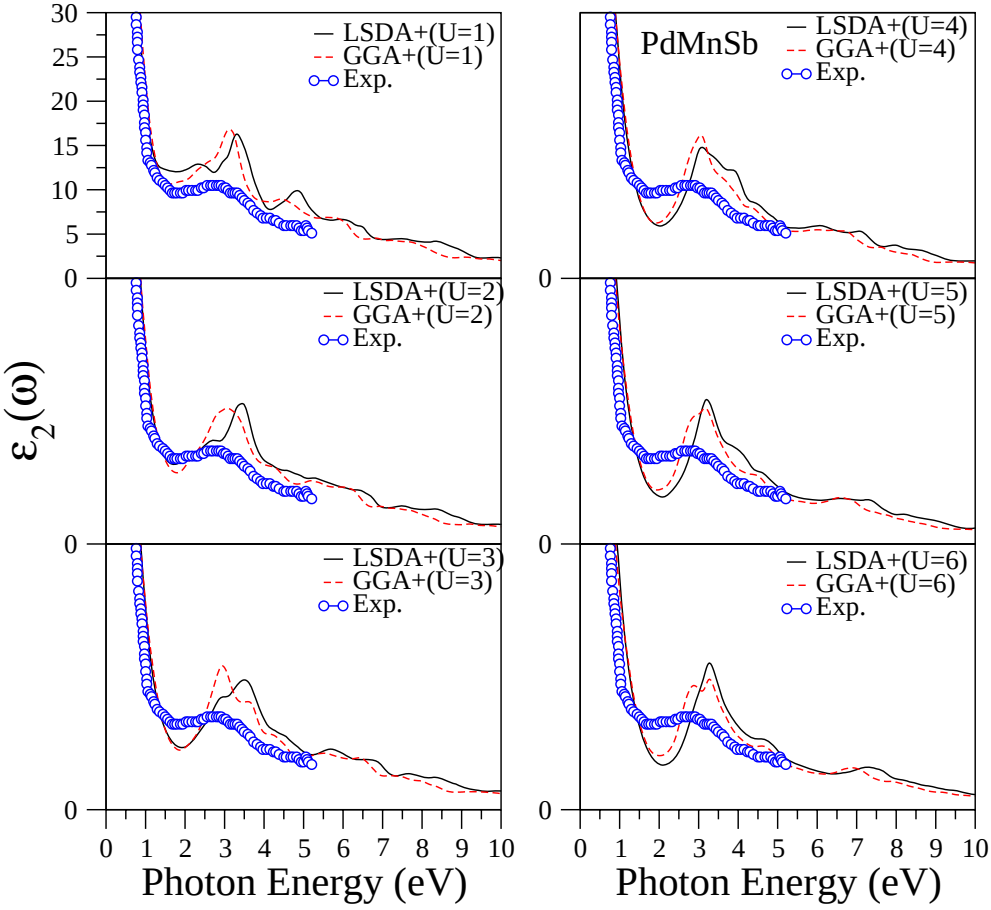

Figure 5.9 Comparison between the experimental [23] and the calculated imaginary part of The dielectric function for different values of U for PdMnSb. The Lorentzian broadening is equal to δ_L= 0.1 eV.

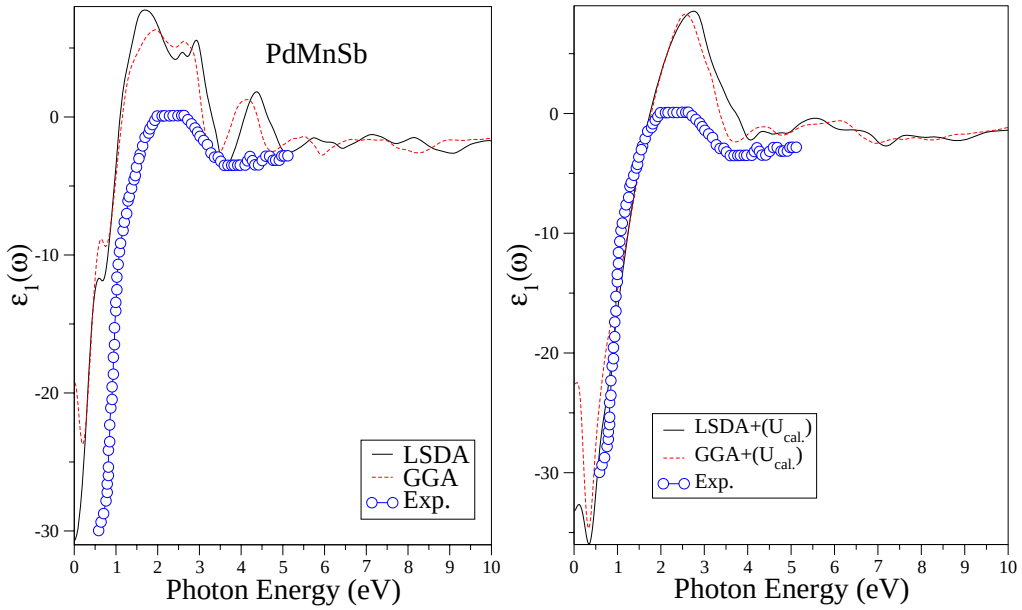

Figure 5.10 Calculated and experimental [23] real part of the dielectric tensor of PdMnSb compound. The Lorentzian broadening equal to δ_L= 0.1 eV.

After having shown the optical spectra, we turn to the magneto-optical spectra. According to the relation giving the Kerr rotation, this later can be enhanced by larger off-diagonal conductivity and a smaller diagonal part. In order to give more detailed insight into the origin of the features in MO spectra in terms of electronic structure, the complex diagonal optical conductivity σ_{xx} without the spin orbit coupling for both contributions intra and inter are shown in figures 5.11 and 5.12.

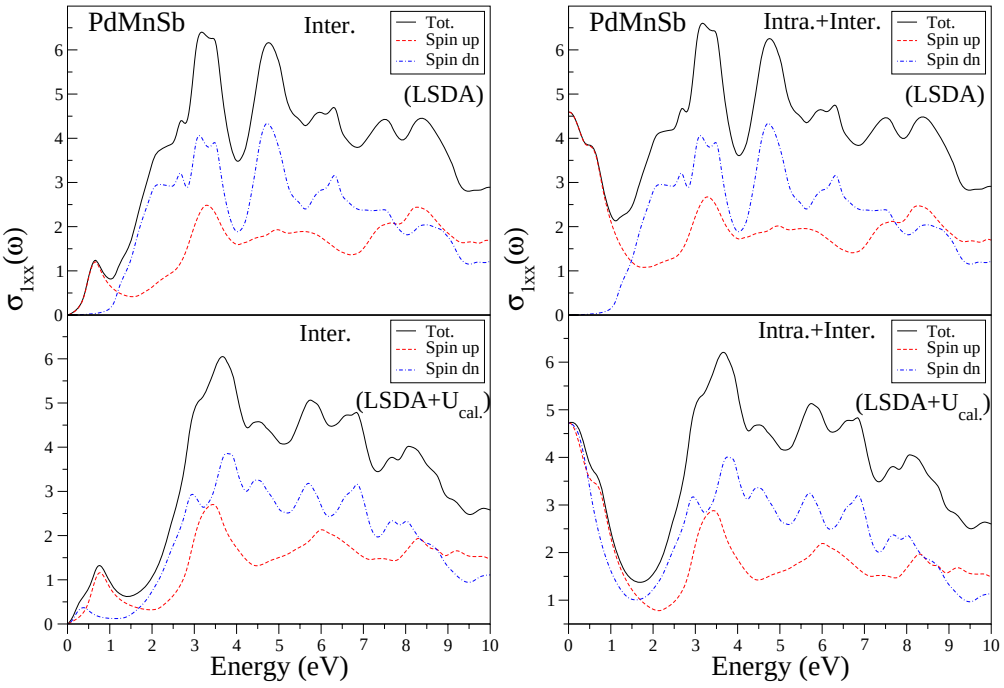

Figure 5.11 Spin decomposition of the diagonal optical conductivity $\sigma_{1xx}(\omega)$ of PdMnSb. The total dependence is shown by the solid line, spin-majority contribution by the dotted line (red colour), and spin-minority contribution by the dashed line (blue colour) with LSDA and LSDA+U. The Lorentzian broadening equal to δ_L= 0.1 eV

It is clear that the intra contribution is significant at lower energies, while at higher energies the conductivity is due mainly to the inter transition of the minority spin channel.

To understand the effect of interband transition on the magneto-optic properties, experimentalist often display $\omega\sigma_{xy}$ instead of σ_{xy} . So, we present $\omega\sigma_{xy}$ spectra in figure 5.13, the life time used for these spectra is 0.7 eV. In the LSDA+U the spectrum is shifted to higher energies, while conserving the same shape as the one obtained using the LSDA. The $Im\omega\sigma_{xy}$ spectra compares very well with that obtained by Antonov et al. [3].

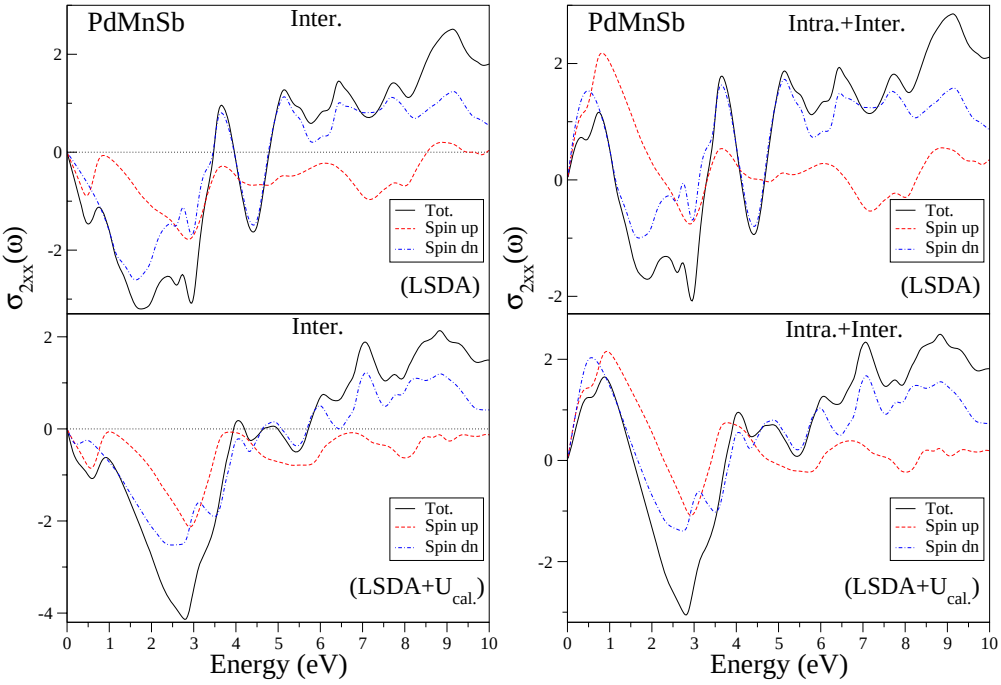

Figure 5.12 Spin decomposition of the diagonal optical conductivity $\sigma_{2xx}(\omega)$ of PdMnSb. The total dependence is shown by the solid line, spin-majority contribution by the dotted line (red colour), and spin-minority contribution by the dashed line (blue colour) with LSDA and LSDA+U. The Lorentzian broadening equal to δ_L= 0.1eV.

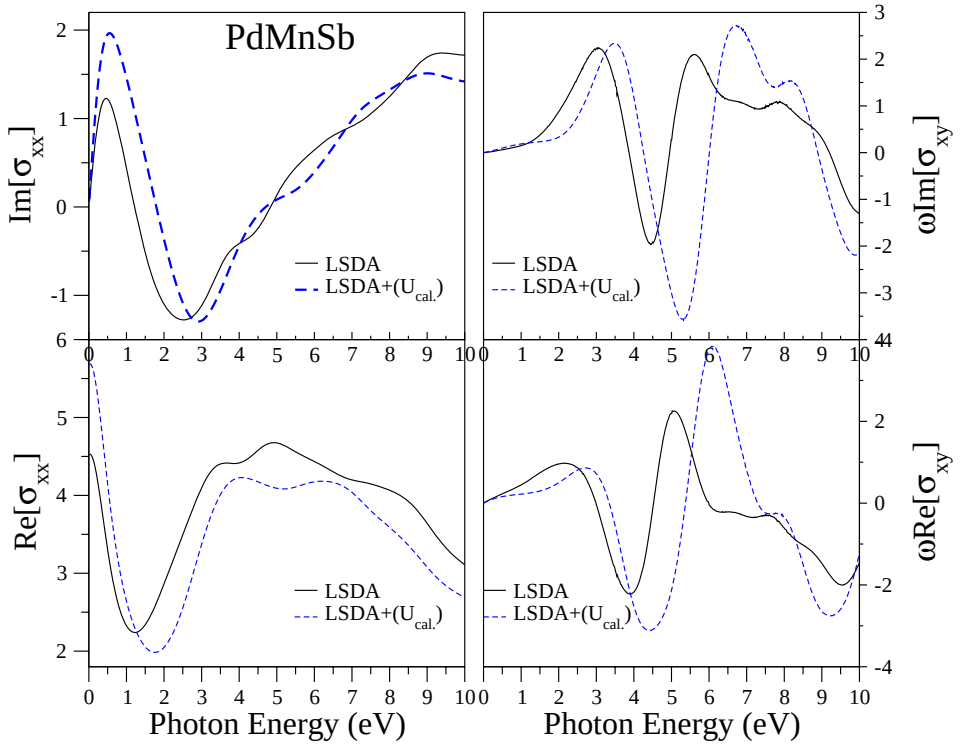

Figure 5.13 Diagonal and off diagonal optical conductivity $\sigma(\omega)$ of PdMnSb. The Lorentzian broadening is equal to δ_L= 0.7 eV.

The imaginary part of the conductivity, $Im[\omega\sigma_{xy}]$, has a direct physical interpretation. It is proportional to the difference of absorption rate of left and right circularly polarization light [24] and its zeros correspond to the equality of the absorption coefficient for right and left circularly polarization light.

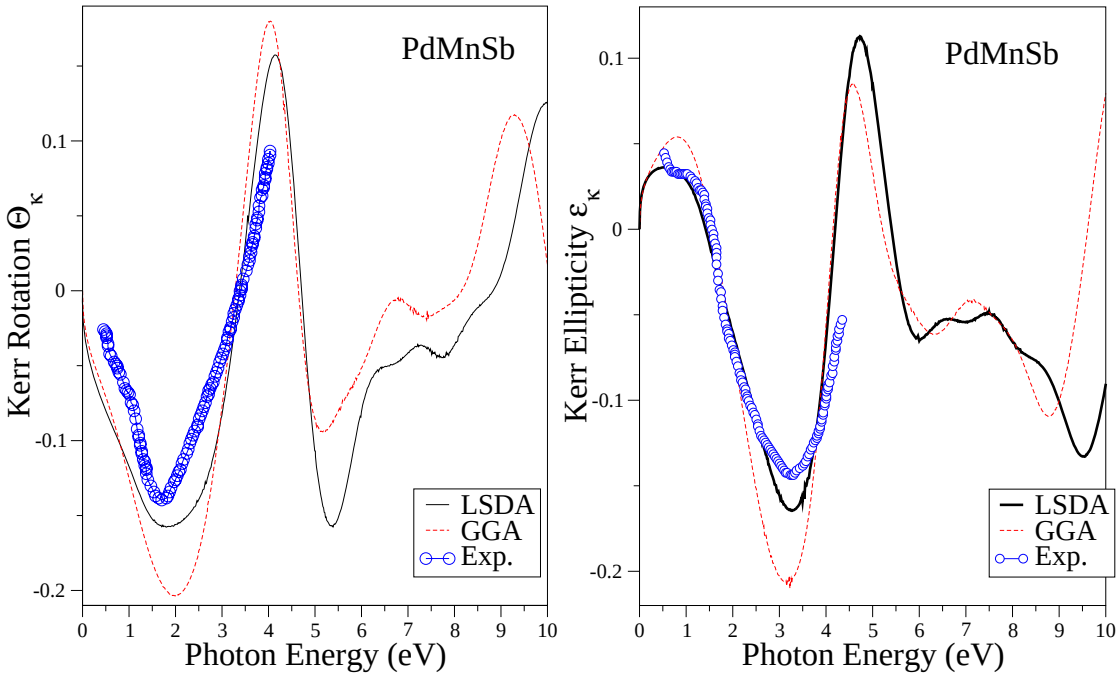

Figure 5.14 The calculated LSDA and GGA and experimental [8] Kerr rotation and ellipticity. The Lorentzian broadening equal to δ_L= 0.7 eV

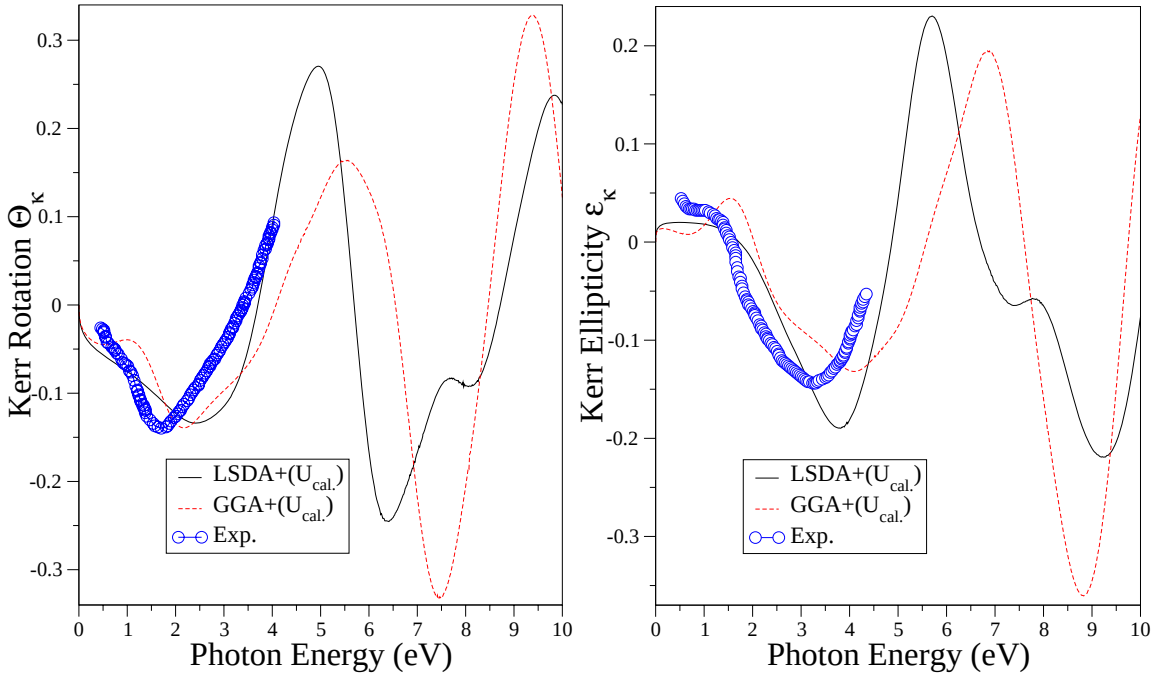

Figure 5.15 The calculated LSDA+U and GGA+U and experimental [8] Kerr rotation and ellipticity. The Lorentzian broadening equal to δ_L= 0.7 eV.

The polar Kerr rotation and Kerr ellipticity for PdMnSb are shown in figure 5.14 and 5.15 for different approximations and with Lorientzan broadening equals to 0.7 eV, which is nearly equal to the one used by Kübler in Ref [1]. The experimental spectrum [8] is also included in this figure. It is clear that there is an excellent agreement between the calculated (with LSDA) and the measured spectra; the only difference is being larger amplitude of the calculated Kerr angle. This is a common phenomena and can be ascribed to a sample surface that is not ideal, i.e., it my have dislocations, an oxide overlayer, or distortions due to surface treatment. Furthermore, our calculation reproduces the first peak position better than that reproduced by Antonov et al.[3], they used the LMTO method.

In order to get insight into the origin of the peaks in the Kerr rotation spectra, we compare them with the curve of diagonal and off diagonal part of the optical conductivity. The Kerr rotation displays the same slope as $Im[\omega\sigma_{xy}]$ being enhanced at 1-2 eV by the contribution from the denominator. Inspection of σ_{1xx} and σ_{2xx} curves shows that the spin orbit coupling and the spin polarization influnces the first rotation peak. While the others peaks are caused by $Im[\omega\sigma_{xy}]$. The Kerr ellipticity spectra are well reproduced by our calculations. Moreover, it is clearly seen that when the Kerr ellipticity cross the zero line, a peak always appears in the Kerr rotation spectra and vice versa due to the Kramer-Kronig relation.

When we use the LSDA+U (GGA+U) and exactly when U ranges from 1-3 there is no essential change in the shape of Kerr spectra with only the shift of the peaks to the higher energies as seen in figure 5.16.

Finaly we present our predicted MO results for the full Heusler alloys Pd_2MnSb and compare them to those of PdMnSb in figure 5.17. It is obvious that there exists four main peaks in the Kerr rotation spectra in Pd_2MnSb in the energy range 0-10eV, the same number as in PdMnSb. The overall shape of the Kerr rotation and ellipticity spectra is similar in both compounds. But at low energy, they have different signees. From the comparison of the spectra of PdMnSb with experiment, Pd_2MnSb, shows week Kerr rotation.

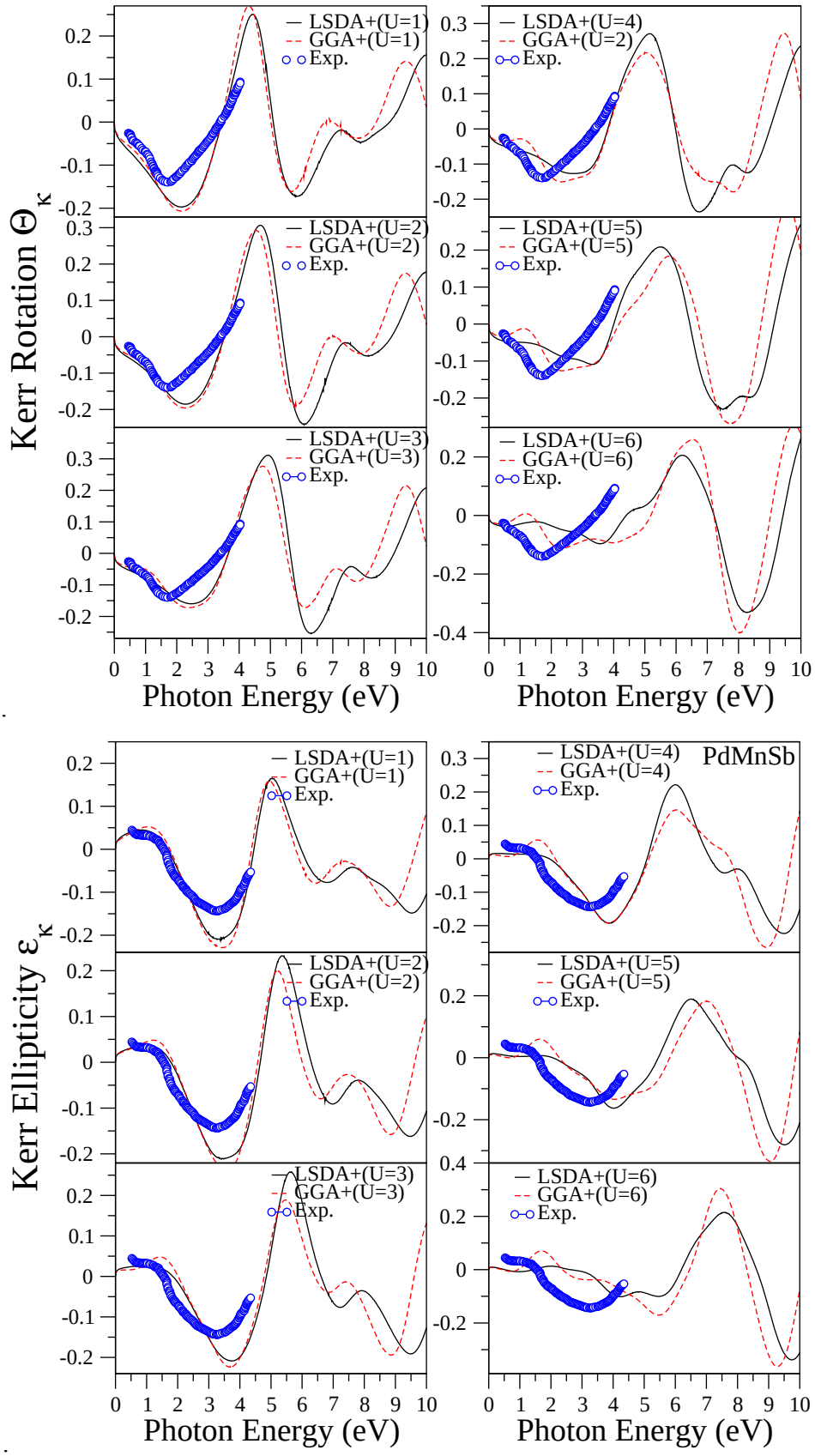

Figure 5.16 The calculated (LSDA+U) and (GGA+U) and experimental Kerr rotation and ellipticity with U ranged from 1 to 6 eV.

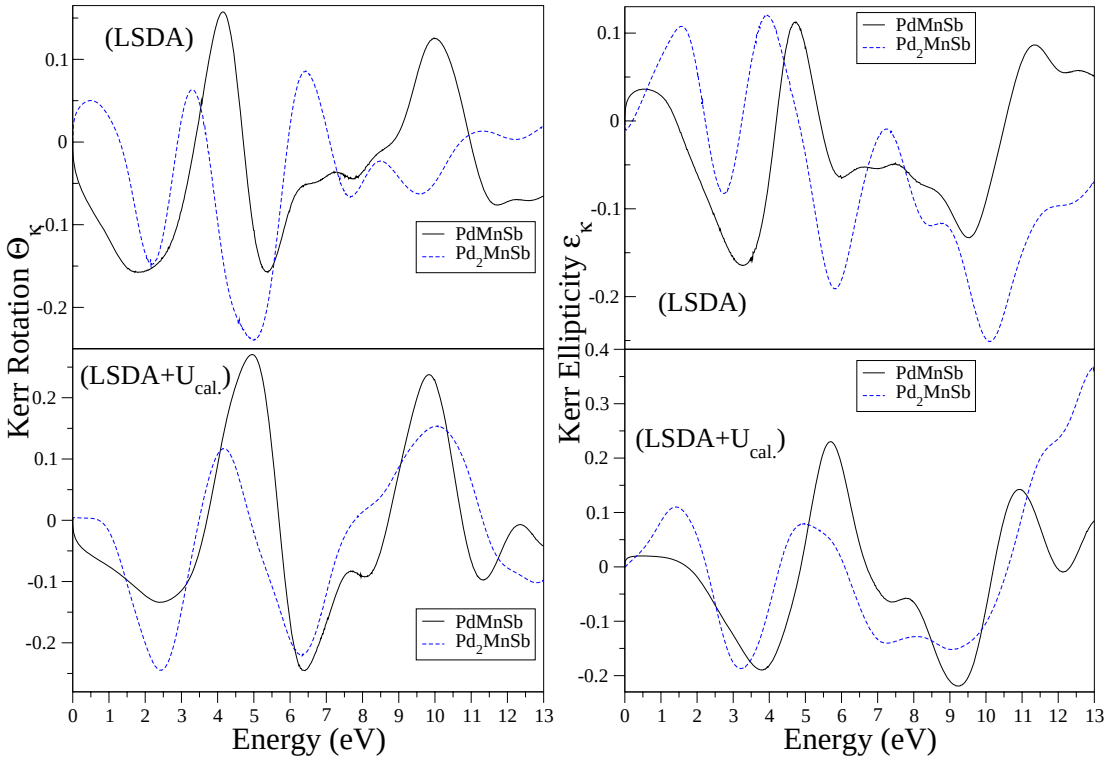

Figure 5.17 Comparison of the calculated LSDA (LSDA+U) Kerr rotation and ellipticity of PdMnSb and Pd_2MnSb compound.

CONCLUSION

We have investigated the electronic, optical and magneto-optical properties of the Heusler compounds PbMnSb, and Pb_2MnSb using the FP-LAPW method within LSDA (GGA) and with the on-site Coulomb correction LSDA+U (GGA+U).

Our LSDA calculations reveal a gap in the E_F, predicting half metallic nature. On the other hand, the LSDA+U results move the d states away from the Fermi level but the shift of the unoccupied states make this compound metallic in both spin (up and down).

We show that the LSDA+U can produce accurate optical properties; the calculated optical spectra using LSDA and LSDA+U are give good results as compared with the experimental data. Our calculations suggest that the magneto-optical are reproduce very well the experimental one when broadening is taken as 0.7 eV, i.e., with a larger impact of the finite lifetime effects.

The magnetic moments calculated by LSDA+U (GGA+U) for the present compounds are found to be very large. Moreover, there is a very good agreement of our GGA values with the experimental values for the magnetic moment. Furthermore, we found that the main contribution to the magnetic moments comes from Mn atom.

We have observed that LSDA gives an overall improvement of Kerr spectra with experiments whereas with LSDA+U the agreement is relatively poor. In another hand, a small difference in Kerr spectra appeared when we calculated it with and without inclusion of the Drude (intraband) contribution.

REFERENCE

1- J. Kübler J. Phys. Chem. Solid 56, (1995) 1529.

2- E. Kulatov, Yu. Uspenskii, S. Halilov J. Magn. Magn. Mater. 145, (1995) 395.

3- V. N. Antonov, P. M. Oppeneer, A. N. Yaresko, A. Ya. Perlov, and T. Kraft, Phys Rev. B 56 (1997) 13012.

4- P. Turban, S. Andrieu, and B. Kierren , C. Teodorescu and A. Traverse Phys. Rev. B 65, (2002) 134417.

5- S. Gardelis, J. Androulakis, Z. Viskadourakis, E. L. Papadopoulou, J. Giapintzakis, S. Rai, G. S. Lodha, and S. B. Roy Phys. Rev. B 74, (2006) 214427.

6- J S Kang , J. Park , C Olson , S J Youn and B I Min J. Phys. Cond. Matter 7 (1995)3789.

7- J. Kübler J. Phys. Chem. Solids 56, (1995) 1529.

8- V. Engen P., Buschow K. H. J., Jongebreur R. and Erman M., Appl. Phys. Lett. 42,202 (1983).

9- P. J. Webster and R. S. Tebble, Phil. Mag. 16, (1967) 347.

10- G. L. Ferreira-Fraga, L. A. Borba, and P. Pureur Phys. Rev. B 74, (2006) 064427.

11- L. J. Swartzendruber and B. J. Evans Phys. Lett. 38 (1972) 511,

12- B Lindgren, K Pernesthl, S Bedit and E Karlsson J. Phys. F: Metal Phys., 7, (1977) 2405.

13- J.P. Perdew, Y. Wang, Phys. Rev. B 45 (1992) 13244

14- J.P. Perdew, K. Burke, M. Ernzerhof, Phys. Rev. Lett. 77 (1996) 3865

15- D. D. Koelling and B. N. Harmon, J. Phys. C 10, 3107 _1977

16- A. H. MacDonald, W. E. Pickett, and D. D. Koelling, J. Phys. C 13, (1980) 2675.

17- J. Kuneš, P. Novák, M. Diviš, and P. M. Oppeneer, Phys. Rev. B 63, (2001) 205111.

18- P. Blaha, K. Schwarz, G. Madsen, D. Kvasnicka, J. Luitz, WIEN2k,an Augmented Plane Wave+ Local Orbitals Program for CalculatingCrystal Properties, Karlheinz Schwarz, TU Wien, Austria, ISBN 3-9501031-1-2, 2001.

19- V.I. Anismov, O. Gunnarsson, Phys. Rev. B 43, (1991) 7570.

20- K. Endo, J. Phys. Soc. Japan 29, (1970) 643.

21- P. G. van Engen, K. H. J. Buschow, R. Jongebreur, and M. Erman Appl. Phys. Lett. 42, (1983) 202.

22- P.J. Webster and R. S. Tebble, Phil. Mag. 16, (1967) 347.

23- M. M. Kirillova, A. A. Makhne, E. I. Shrede, V. P. Dyakin, and N. B. Gorina phys. stat. sol. (b) 187, (1995) 231.

24- J. Cai, X. Tao, W. Chen, X. Zhao, M. Tan, J. Magn. Magn. Mater. 292, (2005) 476.

Chapter: 06

Results and Discussion

PSEUDO-BINARY COMPOUNDS

PdX_2 (X=P, S And Se)

6.1. INTRODUCTION

During the last decade a considerable number of experimental and theoretical studies have been reported on the Transition-metal dichalcogenides with pyrite [1-5], marcasite [6-8] and loellingite[9] structures which have attracted considerable attention due to their electrical, magnetic, and optical properties and they have shown to have applications in many technologically important areas, such as photovoltaic solar cells[10,11] and as substrate for semiconductor growth[12]. The three dimensional pyrite structures can be transformed to the layer structure in a strong crystal field; in the transition metal diselenides and disulphide or transition metal diphosphided the d^8 cations such as Pd which preferentially adopt a square-planar coordination can be regarded as stacking of two-dimensional sandwiches. These crystal structures were confirmed by many researchers [13,14]. Bither et al. have described the preparation and studied the electrical and optical properties of new PdP_yS_{2-y} ($0<y<2$) compounds between the known end members PdP_2 and PdS_2 [15]. Burdett et al. have investigated the relationships between electronic and geometrical structure for the series Pd(XY), where XY=P_2, PS and S_2 by using molecular orbital calculations and tight-binding computations based on the extended Hückel method[16].

6.2. CRYSTAL STRUCTURE AND CALCULATIONS DETAILS

Figure 6.1 shows the unit cells of the compounds PdP_2 and $PdSe_2$. The crystal structure of Palladium diphosphide, PdP_2, is a monoclinic body-centered with the space group I2/a. The 4 Pd atoms positions are ±(1/4, 3/4, 1/4) and the 8 P atoms occupy the positions ±(xyz)(x,−y, 1/2 + z) with x = 0.1886, y = 0.1237, z = 0.3537 [14]. The P atoms form continuous zig-zag chains along one of the axis; each palladium atom is bonded to four phosphorus atoms and each phosphorus atom to two palladium atoms and to two phosphorus atoms. In the present calculations, we have used the space group B2/b instead of I2/a, the later basis vectors (a′, b′, c′) can be obtained from the former ones (a, b, c) by the transformation (a′, b′, c′) = P(a, b, c) with P is a rotation matrix given by :

$$p = \begin{pmatrix} -1 & 1 & 0 \\ 0 & 0 & -1 \\ -1 & 0 & 0 \end{pmatrix}$$

The PdS_2 and $PdSe_2$ compounds crystallize in an orthorhombic structure with space group Pbca− D^{15}_{2h}, the unit cell contains four palladium atoms and eight selenium (sulphur) atoms. The Wyckoff positions of Pd are (a): (0, 0, 0); (1/2, 1/2, 0); (0, 1/2, 1/2); (1/2, 0, 1/2) and the Se and S ones are (c): ±[(x, y, z); (1/2+x, 1/2−y,−z); (−x, 1/2+y, 1/2−z); (1/2−x,−y, 1/2+z)], where x, y and z are the internal free coordinates; x = 0.112(0.107) y = 0.117(0.112) and z = 0.407(0.425) for Se(S) [13]. This structure is considered as a deformed pyrite-like type. The nearly regular octahedral arrangement around the metal atom, characteristic of the pyrite-type structure, is transformed into a square arrangement as two of the six metalloid atoms have moved away. At the same time, the configuration around the metalloid atom has lost its regular tetrahedral character.

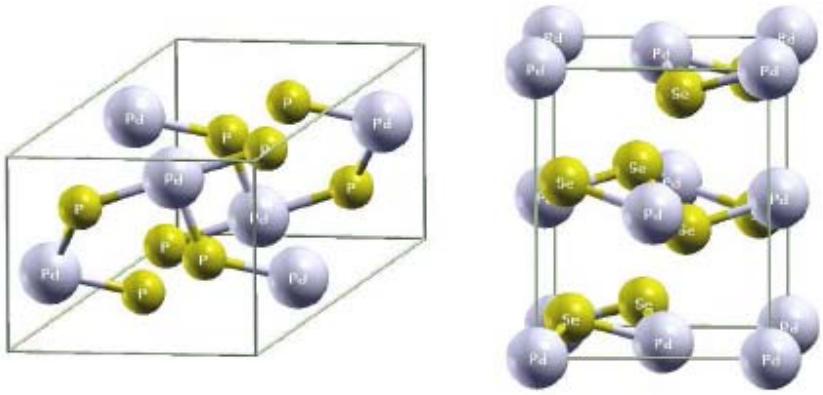

Figure 6.1 crystal structure PdP_2 and $PdSe_2$ compounds

The present calculations are performed using the all-electron full potential linear augmented plane wave plus local orbitals (FP-LAPW+LO) method [17] as implemented in WIEN2K code [18] within the local density approximation (LDA) [19,20]. This method described previously in chapter 4. In this work we treat the core electrons fully relativistically, and the valence electrons

semi relativistically (all relativistic effect are taken into account except the spin-orbit coupling). The MT sphere radii are chosen to be 1.9, 1.5 1.9 and 2.0 Bohr for S, P, Se and Pd respectively. The basis functions are expanded up to $R_{mt}K_{max}$=8, (where R_{mt} is the smallest of the MT sphere radii and K_{max} is the largest reciprocal lattice vector used in the plane wave expansion) and up to L_{max} =10 in the expansion of non spherical charge and potential. We were used the Perdew and Wang [21] functional for the exchange and correlation potential. For the Brillouin zone integration we have used 6 × 5 × 6 k points mesh for PdP_2 and 11 × 10 × 8 k points mesh for $PdSe_2$(S) in all the calculation. The self consistent calculations are considered to be convergent when the total energy is stable within 0.1 mRy and the forces are less than 1mRy/Bohr

6.3. STRUCTURAL PROPERTIES

To investigate the electronic properties of PdX_2 compounds, one has to determine accurately the ground state parameters. In this context, we have used the total energy approach to determine the positions of the atoms and the lattice parameters.

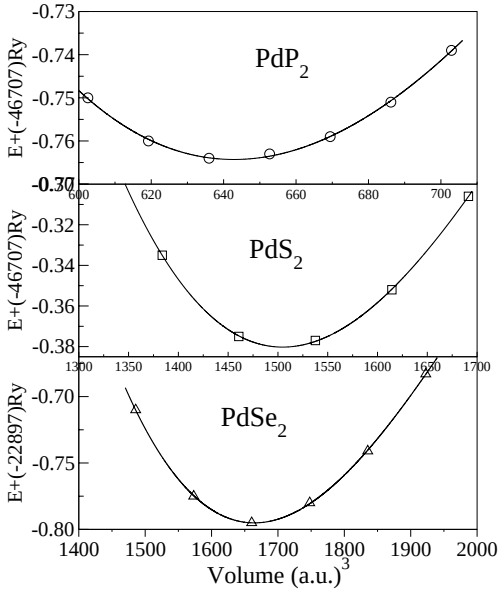

Figure 6.2 Total energy vs the variation of the unit cell volume of PdX_2 (P, S and Se) compounds.

The experimental lattice constants and positions are used as the starting point to perform the structural calculations. For PdP_2 compound and due to its complex monoclinic structure, the unit cell relaxed, according to the Newton's laws, by varying the a, b and c lattice parameters and the

angle beta simultaneously at a series of fixed volumes and the total energies were calculated for each volume and the optimized structural parameters corresponding to the lowest energy. While for the orthorhombic lattice parameters of PdS_2 and $PdSe_2$, we performed the structural optimization by calculating the total energies for different c/a and b/a ratio around the equilibrium cell. We have fixed these two equilibrium parameters by calculating the equilibrium volume using Murnaghan's equation of state as shown in figure 6.2. The positions of the atoms in the relaxed compounds are determined by minimizing the total energy and the forces acting on every atom of the system using the Hellman-Feynman theorem. The forces on the atoms are geometrically relaxed by allowing them to move according to Newton's laws in the presence of fictitious damping force. The system evolves until equilibrium geometry is obtained. In table 6.1

Table 6.1 Calculated equilibrium lattice constants (a, b and c), bulk moduli (B) and the engle β for the PdP_2, PdS_2 and $PdSe_2$ compounds and the available experimental data

	PdP_2		PdS_2		$PdSe_2$	
	cal.	exp.[1]	cal.	exp.[2]	cal.	exp.[2]
a (Å)	6.20	6.207	5.465	5.460	5.866	5.741
b (Å)	5.85	5.857	5.538	5.541	6.0	5.866
c (Å)	5.887	5.874	7.525	7.531	7.357	7.691
β (°)	111.76	111.8	-	-	-	-
B (GPa)	151.34	-	116.51	-	105.72	-

[1] Ref [14] [2] Ref [13]

the calculated values of the lattice constants a, b, c are compared with the experimental results, this table displays also the obtained values of the bulk modulus (B). The deviations of the absolute values of the lattice parameters are smaller than 4.5% for all parameters. The bulk modulus decreases in going from P to Se compounds, this is a normal behavior related to the increase in the equilibrium volume V_0. Since there are no reported experimental data for the bulk modulus, our results represent a prediction. One point needs to be added is that the obtained

results of the atom positions show no significant change between the calculated values and the experimental ones as shown in table 6.2. The optimized inter atomic positions are displayed in table 6.3 together with the experimental ones.

Table 6.2 Positional parameters of PdP_2, PdS_2 and $PdSe_2$ compounds and available experimental data.

	PdP_2		PdS_2		$PdSe_2$	
	cal.	exp. [1]	cal.	exp. [2]	cal.	exp. [2]
x	0.143	0.188	0.104	0.107	0.112	0.112
y	0.124	0.123	0.109	0.112	0.118	0.117
z	0.305	0.353	0.416	0.425	0.404	0.407

[1] Ref [14] [2] Ref [13]

Table 6.3 Shortest interatomic distances (Å) for the PdP2, PdS2 and PdSe2 compounds and the available experimental data.

		cal.	exp.
PdP_2	$Pd-P$	2.349	2.335 [1]
	$Pd-Pd$	2.944	––
	$P-P$	2.177	2.201 [1]
PdS_2	$Pd-S$	2.320	2.300 [2]
	$Pd-Pd$	3.890	––
	$S-S$	2.086	2.130 [2]
$PdSe_2$	$Pd-Se$	2.482	2.440 [2]
	$Pd-Pd$	4.195	––
	$Se-Se$	2.393	2.360 [2]

[1] Ref [14] [2] Ref [13]

6.4. ELECTRONIC STRUCTURE

Figure 6.3 shows the calculated band structures at equilibrium volume and for the optimized atomic positions for the PdX_2 (X=P, S and Se) compounds along the high symmetry lines in the corresponding Brillouin zone. It is clear from this figure that in the PdP_2 compound, there is no

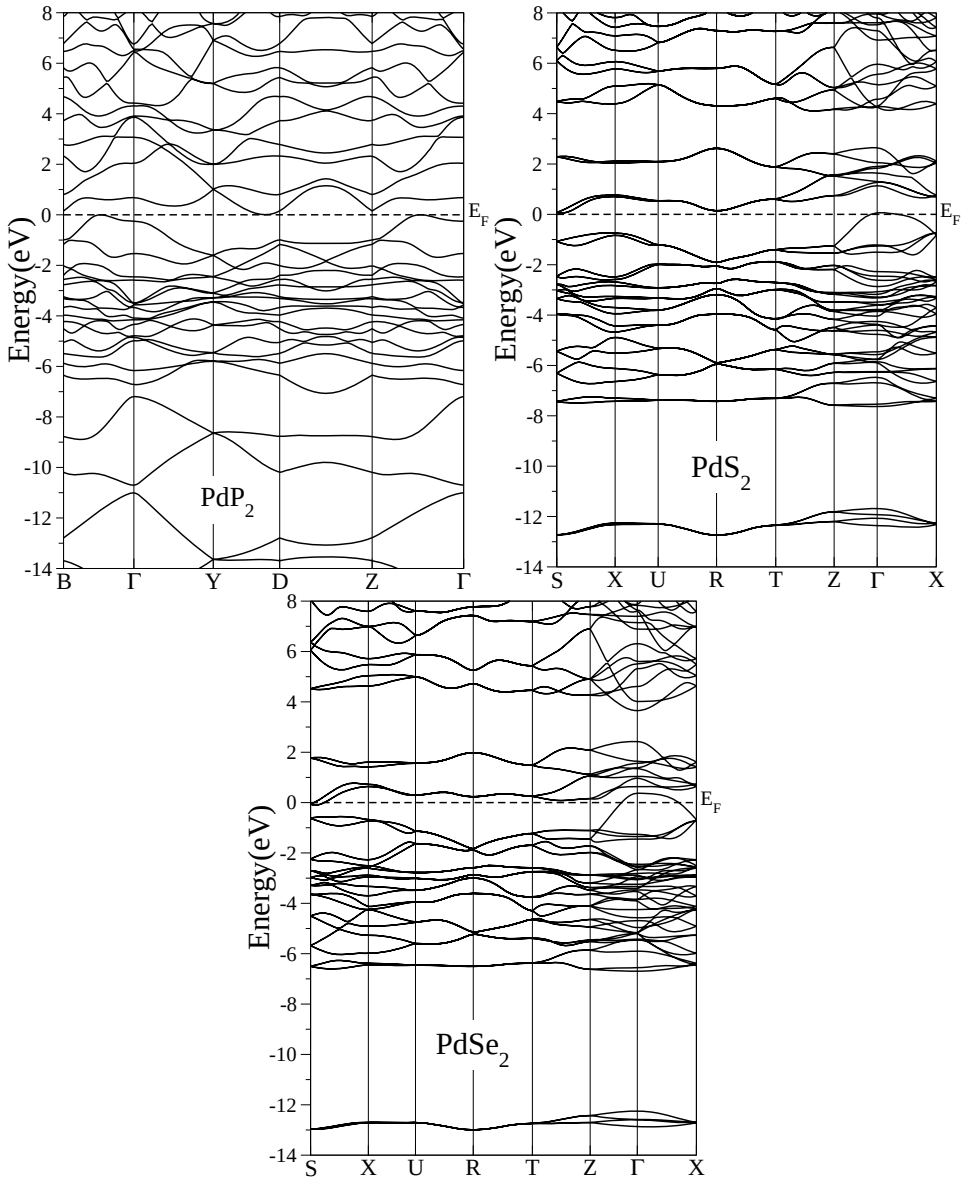

Figure 6.3 Band structure of PbX_2 compounds along high symmetry directions in the Brillouin Zone. The Fermi energy is at zero.

gap which separates the valence and the conduction states, i.e., the conduction band drops towards the Fermi level (E_F) which suggests that this system is a metal in contrast with the

experimental results [22-24] which were derived from resistivity measurements; 0.6-0.7 eV [23]. This discrepancy between the experimental and the theoretical data is due, as it is well known, to the approximation used (LDA) which underestimates the band gaps. Our calculations show that PdS_2 and $PdSe_2$ have similar band structures. In PdS_2 the conduction band drops towards the valence one but no band crossing the Fermi level; which makes the pseudo-gap exactly at the Fermi level, while, in $PdSe_2$ we observe an important feature which is the existence of a band that lies just above the Fermi level in the directions Z-Γ and Γ-X, which can be attributed to the fact that when we move from S to Se there is a significant increase in the valence band towards E_F. The experimental values of the gaps for PdS_2 and $PdSe_2$ which where also obtained from resistivity measurements are 0.7-0.8 eV and 0.4 eV [24], respectively. However, the smaller experimental value of the gap for $PdSe_2$ is translated by the occurrence of the overlap between the conduction and the valence bands in the calculated band structure for this compound compared to PdS_2. For this reason we have used the LDA+U, with U ranging from 1 to 3 eV, which predicts that PdS_2 is a semiconductor as shown in figure 6.4, with a gap value of 0.14 eV, while PdP_2 and $PdSe_2$ stay metallic.

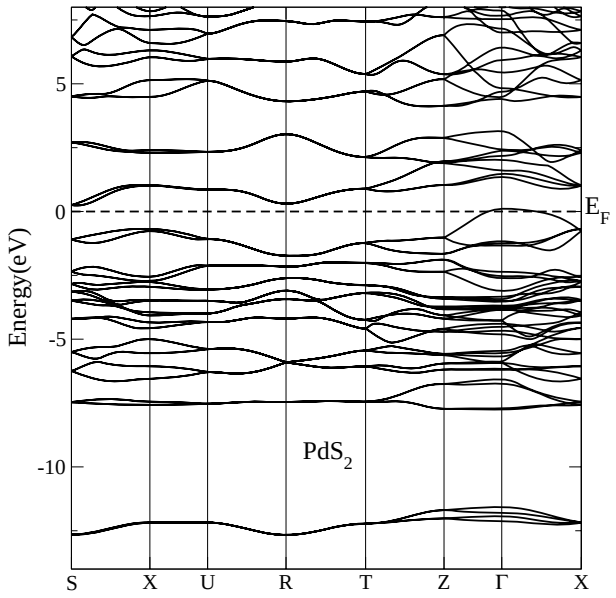

Figure 6.4 Band structure of the PbS_2 compound along high symmetry directions in the Brillouin zone with the LDA+U. The Fermi energy is set to zero.

The qualitative similarity of the electronic structure of these two compounds is also evident in the total density of states (DOS) as shown in figures 6.5, where the vertical dashed line represents the Fermi level. The whole shapes of the DOS are nearly identical, with some smaller differences. Te Fermi levels are located in the pseudo-gap region with a clear separation of bonding and antibonding states. For $PdSe_2$ and PdS_2 the density of state DOS, i.e., the bands, can be divided into four main energy regions. In order to understand the above-mentioned results, figure 6.6 displays the calculated partial density of states. We note that the lowest part which lies between 11−12.5 eV below EF comprises the Se-s states, while the second group extending from 7 eV below EF up to E_F, which contains a

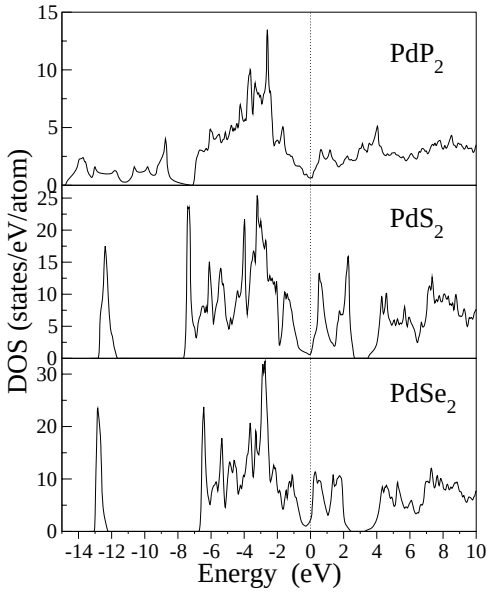

Figure 6.4 Total densities of states (DOS) of PdX2 (X=P,S and Se) compounds.

sharp pick at about 3 eV, is arising from the Pd-d and Se(S)-p states, where the Pd-d states contribution dominates and these states are shifted up in energy in $PdSe_2$ compared with the ones in PdS_2. These states represent the initial states for the optical transitions. The third region extending from E_F to 5 eV above EF has significant contribution from Pd-d and Se-p states. The last group, at about 3.5 − 10 eV above E_F, has contributions from Se(S)-s, and Se(S)-p states where the latter has the major component. The DOS of PdP_2 shows less structure and the low lying P-s and Pd-s states are delocalized and show strong dispersion, spreading from -14 to -6 eV,

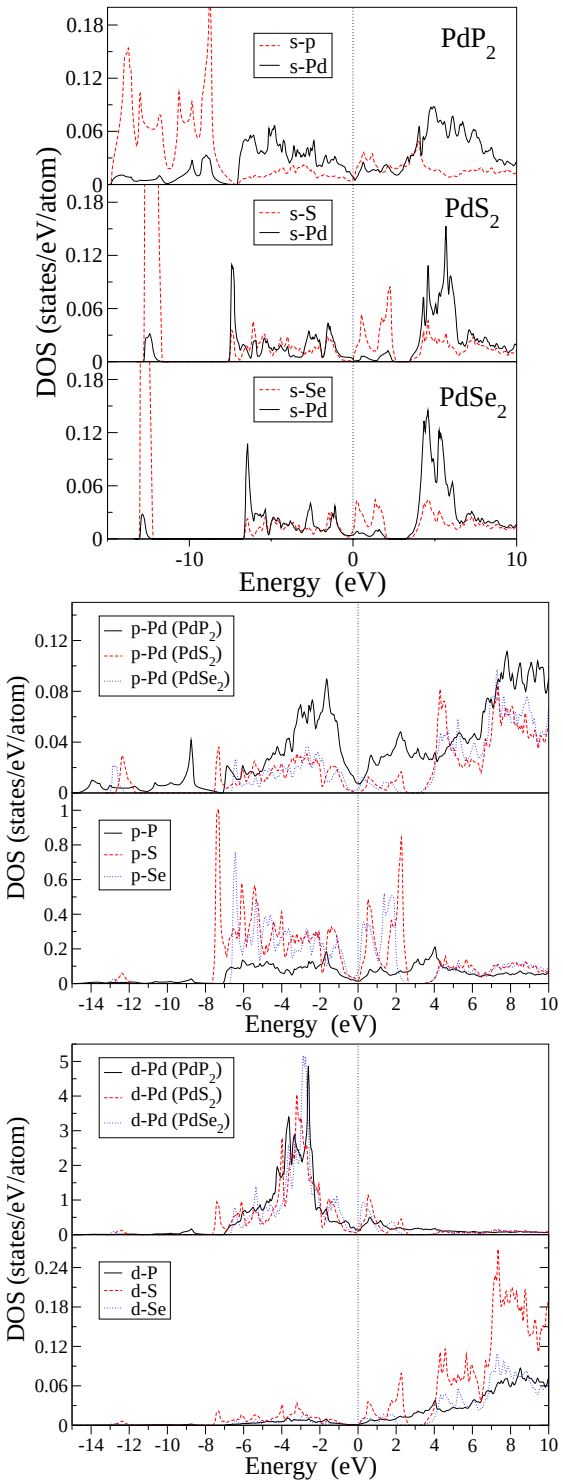

Figure. 6.5 Partial densities of states (DOS) of PdX_2 *(X=P,S and Se)* compounds

while in the other two compounds these bands are narrow and flat, reflected in the pronounced peaks. The calculated density of states for the studied compounds shows that the absorption starts with a modest intensity in the infrared region (IR) then it gets stronger at higher energies. Furthermore, the calculated density of the states at the bottom of the conduction bands and the top of the valence ones for PdS_2 might causes only a weak absorption in the IR region compared to PdP_2.

CONCLUSION

In conclusion, we have carried out first principles calculations to investigate the structural and electronic properties of PdX2 (X=P, S and Se), using the FP_LAPW+LO method. The structural properties are determined through total energy and interatomic forces minimization. The calculated lattice constants agree well with the experimental ones. Our results show that the studied compounds exhibit a metallic character with LDA. In another hand the LDA+U predict that PdS_2 is a semiconductor with narrow gap while PdP_2 and $PdSe_2$ have metallic character. The calculated density of states suggests that the absorption increases rapidly in the IR regions for PdP_2.

REFERENCE

1- M. Meier, R. Weihrich, Chem. Phys. Lett. 461 (2008) 38.

2- L. Charrona, D. Dumchenkob, E. Fortina, C. Ghermanb, L. Kulyuk, J. Lumines. 112 (2005)45.

3- A. Gaojun, L. Chenguang, H. Yuandong, Z. Xiaoling, L. Yunqi, Mater. Lett. 62 (2008) 2643.

4- X. Ming-Zhe, F. Zheng-Wen, Elec. Commun. 8 (2006) 1855.

5- K. S. Savage, D. Stefan, S. W. Lehner, Appl. Geochem. 23 (2008) 103.

6- P. Amornpitoksuk, S. Suwanboon, J. of Alloy. Compoun. 473 (2009) 373.

7- H. D. Lutz, B. Mller, Phys. Chem. Miner. 18 (1991) 265.

8- D. W. Bullett, J. Phys. C: Solid State Phys. 15 (1982) 6163-6174.

9- S. L. Harmer, H. W. Nesbitt, Surf. science 564 (2004) 38.

10- P. P. Altermatt, T. Kiesewetter, K. Ellmer, H. Tributsch, Sol. Ener. Mater. Solar Cell. 71 (2002) 181.

11- C. Ballif, M. Regula, F. Lvy Sol. Ener. Mater. Solar Cell. 57 (1999) 189.

12- A. Yamada, K.P. Ho, T. Maruyama, K. Akimoto, Appl. Phys. A 69 (1999) 89.

13- F. Gronvold, E. Rost, Acta Cryst. 10 (1957) 329.

14- W. H. Zacharisan, Acta Cryst. 16 (1963) 1253.

15- T. A. Bither, P. c. Donohue, H. S. Young J. solide state chem. 3 (1971) 300.

16- K. J. Burdett, B. A. Coddens, Inor. chem. 27 (1988) 418.

17- D. Singh, Planes waves, pseudo-potentials and the LAPW method. Kluwer Academic Publishers, Boston, Dortrecht, London, 1994.

18- P. Blaha, K. Schwarz, G. K. H. Madsen, D. Hvasnicka and J. Luitz. WIEN2k, An Augmented Plane Wave + Local Orbitals Program for Calculating Crystal Properties. Karlheinz Schwarz, Techn. Universit Wien, Austria, 2001.

19- P. Hohenberg, W. Kohn, Phys. Rev. B 136 (1964) 864.

20- W. Kohn, L. J. Sham, Phys. Rev. A 140 (1965) 1113.

21- J. R Perdew, Y. Wang, Phys. Rev. B 45 (1996) 13244.

22- Non-tetrahedrally bounded binary compounds, Landolt-Börnstein, group III, cond. mat. 41 (2000) 1.

23- F. Hulliger, Nature, 200 (1963) 1064.

24- F. Hulliger, J. Phys. Chem. Solids, 26 (1965) 639.

Chapter: 07

Results and Discussion
ORTHORHOMBIC COMPOUNDS
PdPX (X=S AND Se)

7.1. INTRODUCTION

As we have mentioned in the previous chapter, transition-metal chalcogenides, in terms of composition, provide a wide variety of compounds which crystallize in the pyrite structure [1], in ternary ordered versions (cobaltite, ullmannite) [2], and in the marcasite and distorted marcasite (arsenopyrite) one [3]. Moreover, the ternary pnictide chalcogenides MZX of the d^8 transition metals compounds with the ullmannite structure such as the palladium phosphide sulfide PdPS and the palladium phosphide selenide PdPSe which also belong to the class of layered inorganic materials and were firstly synthesized by Bither et al. [4], are less investigated compared to the transition-metal dichalcogenides. The crystal structure of these materials is closely related to the pseudobinary compounds PdS_2 and $PdSe_2$ [5,6]. Marzik et al. [7] have prepared and studied the electrical and optical properties of PdPSe single crystals. They have shown that this compound has quantum efficiency below 800 nm and an indirect optical gap of 1.29 eV. Burdett and Coddens [5] have used molecular orbital and tightbinding computations based on the extended Hückel method to investigate the relationship between the electronic and the geometrical structure for the series PdP_2, PdPS and PdS_2. Despite of few significant experimental achievements, our knowledge on their electronic and optical properties which will be of primary importance for their use in technological applications is still rather limited. Thus, further theoretical investigations of these properties are needed.

7.2. CRYSTAL STRUCTURE AND CALCULATION DETAILS

The palladium phosphide sulfide PdPS and the palladium phosphide selenide PdPSe compounds belong to the group of layered pnictide chalcogenides transition metal. They crystallize in an orthorhombic structure, space group Pbcn (D^{14}_{2h}) [8], the crystallographic structure is shown in figure 7.1. The lattice parameters a, b and c (shown as x, y and z in figure 7.1) correspond to $\Gamma-X$, $\Gamma-Y$ and $\Gamma-Z$ directions in the first Brillouin zone (BZ), respectively. In these structures the three-dimensional pyrite structure transforms to the slab one. These square-planar coordinations can be thought to evolve from an octahedral coordination by strongly elongating the octahedron of nearest anion neighbours along one diagonal. The palladium Pd elements in square-planar coordination with two Se and two P atoms. Pd atom above and below the coordination plane extend the coordination geometry to an extremely elongated octahedron.

Phosphorous is tetrahedrally coordinated to two Pd, one Se, and one P atom. Selenium is tetrahedrally coordinated to two Pd and one P and a lone pair of electrons as fourth ligand [8].

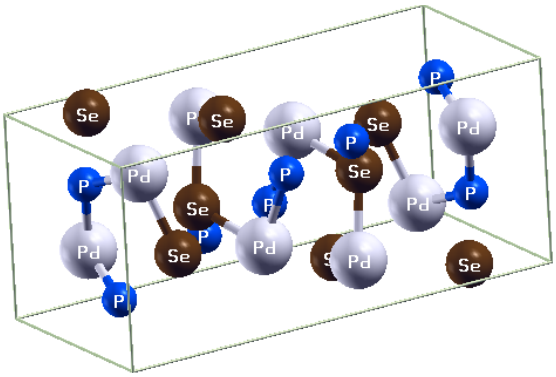

Figure 7.1 Optimized orthorhombic crystal structure of PdPSe

The present calculations are performed using the all-electron full potential linear augmented plane wave plus local orbitals (FP-LAPW+lo) method [9] as implemented in WIEN2K code [10] within the local density approximation (LDA) [11,12]. The MT sphere radii are chosen to be 1.9, 1.9, 2 and 2.2 Bohr for P, S, Se and Pd respectively. The basis functions are expanded up to $R_{mt}K_{max}=8$, (where R_{mt} is the smallest of the MT sphere radii and Kmax is the largest reciprocal lattice vector used in the plane wave expansion) and up to Lmax = 10 in the expansion of non spherical charge and potential. In order to keep the same degree of convergence for all lattice constants studied, we kept the values of the sphere radius and Kmax constants over all the range of lattice spacing considered. We used the Perdew and Wang functional [13] for the exchange and correlation potential. For the Brillouin zone integration and after performing convergence tests, we used 5×13×13 k point mesh in all the calculations. The self consistent calculations were considered to be convergent when the total energy is stable within 0.1 mRy and the forces are less than 1 mRy/bohr.

The calculated optical spectra depend strongly on the BZ sampling, therefore a sufficiently dense k-mesh is used in the calculations of optical spectra, which consists of 8×19×19 k points mesh.

7.3. STRUCTURAL PROPERTIES

We first analyze the structural properties of PdPX (X=S and Se) compounds. In order to determine the ground state parameters in this total energy approach the experimental lattice constants and atomic positions are used as starting points. We have performed the structural optimization by calculating the total energy for different c/a and b/a ratio around the experimental ones. We have fixed the values of these two parameters by calculating the equilibrium volume using Murnaghan's equation of state. The positions of the atoms are determined by minimizing the total energy and the forces acting on every atom of the system. The obtained results are displayed in table 7.1 together with the experimental ones. The calculated values of the atomic positions in the relaxed structures are very close to the measured ones.

Table 7.1 *Calculated positional parameters of PdPS and PdPSe compounds compared with the available experimental data (1 and 2 correspond to PdPS and PdPSe respectively).*

		Pd(*1*)	Pd(*2*)	P(*1*)	P(*2*)	S	Se
x	This work	0.11300	0.11045	0.41818	0.42072	0.34634	0.34203
	Exp1	0.11372	--	0.416	--	0.34624	--
y	This work	0.25085	0.25848	0.13030	0.12334	0.36400	0.36681
	Exp1	0.25292	--	0.12974	--	0.36324	--
z	This work	0.16024	0.15606	0.28145	0.28717	0.04506	0.04136
	Exp1	0.15907	--	0.28111	--	0.04553	--

1 Ref [8]

Furthermore, the calculated Pd-Se bond length is 2.443 Å, slightly larger than the Pd-S one 2.336 Å (Exp.: 2.356 Å [8]) in PdPS which might be attributed to the larger size of the Se atom relative to the S one. The Pd-Pd and P-Pd distances in PdPSe are 3.167 Å and 2.292 Å respectively, which are also slightly larger than the corresponding ones in PdPS; 3.165 Å and 2.285 Å (Exp.: 3.198 Å and 2.205 Å respectively [8]). While we found that the P-P bond length is 2.193 Å and 2.177 Å in PdPS and PdPSe respectively. Table 7.2 shows the calculated values of the lattice parameters and the bulk modulus together with the available experimental data. Bearing in mind the underestimation of the LDA to the lattice parameter, the agreement between the theoretical and the measured values is good. The PdPS bulk modulus value is greater than the

corresponding one for PdPSe, this is understood in the context of volume effect due to the difference in size of the chalcogenide atoms.

Table 7.2: *calculated equilibrium lattice constants (a,b,c) of PdPS and PdPSe compounds compared with the available experimental data*

	PdPS		*PdPSe*	
	Exp1	This work	Exp1	This
a (A°)	13.304	13.262	13.569	13.459
b (A°)	5.677	5.638	5.824	5.812
c (A°)	5.693	5.661	5.856	5.820
V (A°)	429.974	423.27	462.775	455.261
B (GPa)	--	133.93	--	122.55

1 Ref [3]

7.4. ELECTRONIC STRUCTURE

Since the optical properties are closely related to the electronic structure, it is of interest to describe it first and then use it in analysing the different optical spectra. The band structure of PdPS and PdPSe along the high symmetry lines in the Brillouin zone corresponding to the orthorhombic structure is displayed in figure 7.2, while the corresponding total density of states (TDOS) and the site and angular momentum decomposed DOS are shown in figure 7.3.

It is clear from these figures that both compounds are semiconductors and their overall band profiles are similar. The conduction bands shift towards the Fermi level when one moves from S to Se causing a reduction in the energy gap and leading to an increase in the width of the conduction band (see figure 7.3). According to our results there is a small dispersion of the energy bands observed parallel and perpendicular to the layers translated by the flat band around the top of the valence band but at lower energies some bands have significant.

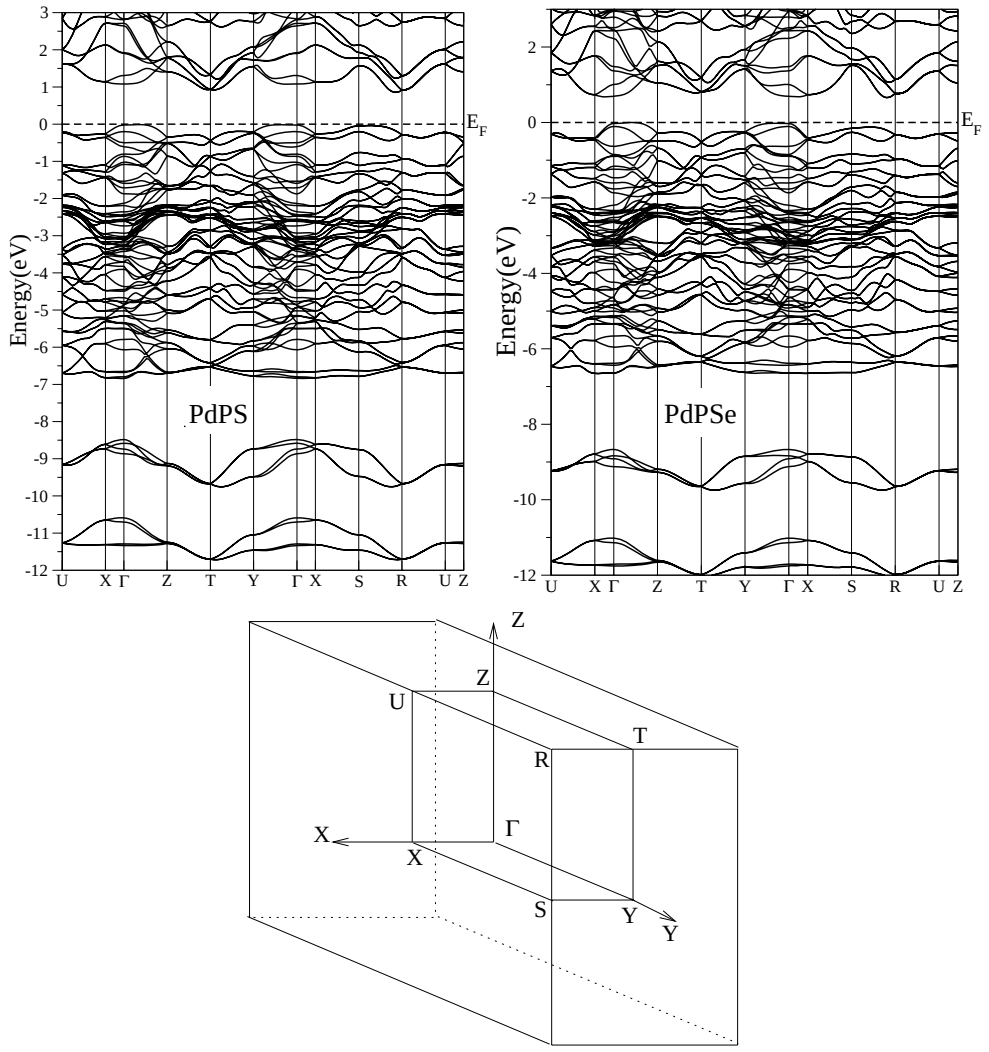

Figure 7.2 band structure of PdPS and PdPSe compounds and the corresponding orthorhombic Brillouin zone with the axis X, Y and Z corresponding to the crystal axes x, y and z respectively. The Fermi energy is set to zero.

The main features of the electronic structure can be followed in figures 7.2 and 7.3. From the calculated DOS and starting from lower energies, the first two peaks corresponding to the lower two energy band groups have mainly chalcogenes and P-s states origin. However, small contribution to these bands from p states of all atoms can be observed. The structure between -7 eV and Fermi level (E_F) characterizes the strong p-d hybridization, while the contribution from the s states are also significant in this region and can not be neglected. A closer inspection of the partial density of states shows that the upper valence.

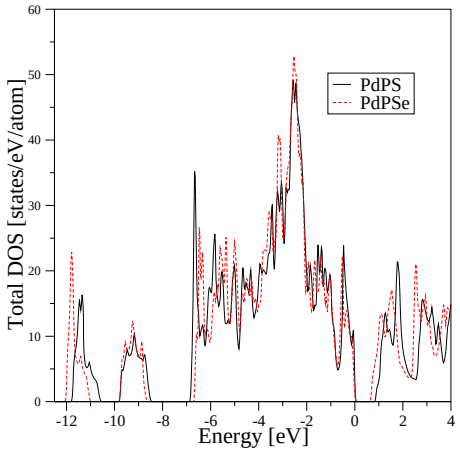

Figure 7.3a Total density of states (states/eV unit cell) for PdPS and PdPSe

The energy band gaps are found to be indirect, i.e., 0.87 eV and 0.66 eV of PdPS and PdPSe, respectively. The nature of the gaps is consistent with the experimental one reported in Refs. [3,7]. The top of the valence band is situated between Γ and Z points of the Brillouin zone and the bottom of the conduction band is located between S and R points for both compounds. It is also worth mentioning that the theoretical gaps are smaller than the experimental values 1.38 eV [3] and 1.29 eV [7] for PdPS and PdPSe respectively, this discrepancy is attributed to the LDA method which always underestimates the band gap.

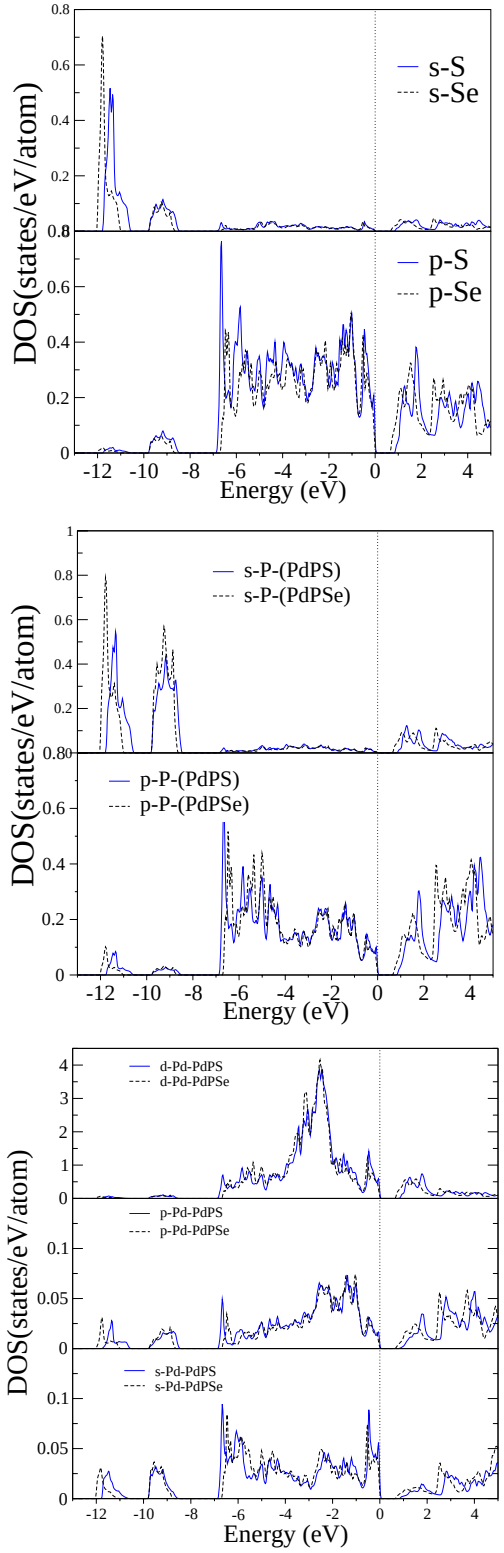

Figure 7.3b Partial density of states (states/eV unit cell) for PdPS and PdPSe compounds

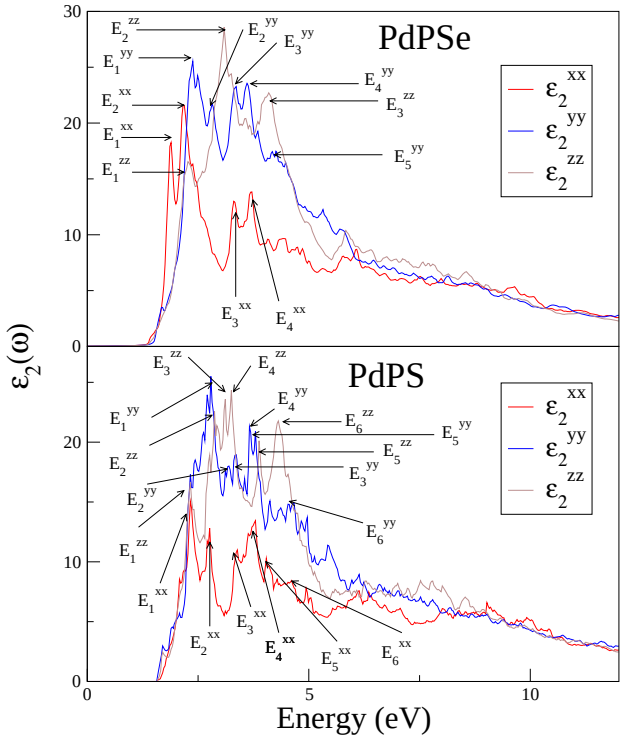

Figure 7.4 Imaginary part of the dielectric function $\varepsilon_2(\omega)$for PdPS and PdPSe compounds

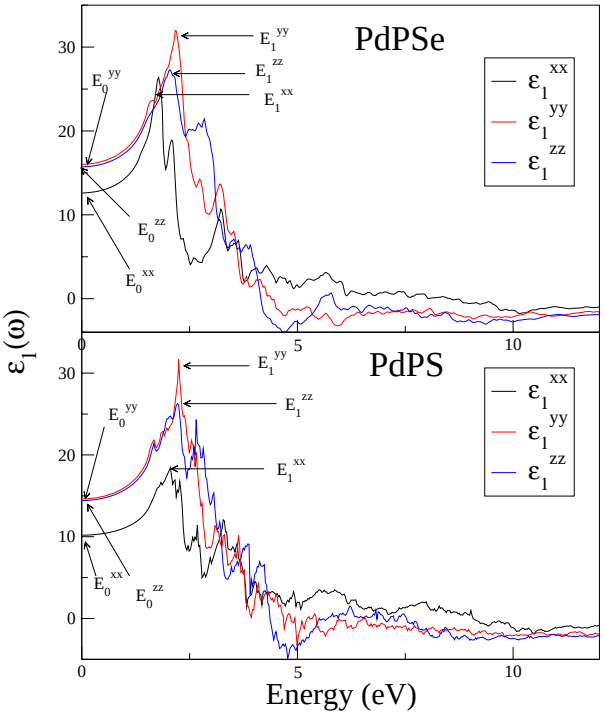

Figure 7.5 Real part of the dielectric function ε_1 for PdPS and PdPSe compounds

7.5. OPTICAL PROPERTIES

The compounds with orthorhombic symmetry have three non-zero components of the dielectric tensor. These compounds correspond to an electric field perpendicular and parallel to the z-axis which are indexed as ε^{xx}, ε^{yy} and ε^{zz}. The calculated imaginary parts for PdPS and PdPSe are shown in figure 7.4. These spectra are not broadened. It is clear from this figure that there is a considerable anisotropy between the three spectra corresponding to different polarisations for each compound. To analyse the calculated optical spectra and determine the origins of the

Table 7.3 *Optical transition in the PdPSe compound.*

Peak position (eV)			Transition	Region	Energy (eV)
xx	E_0	0.71	$(v_1 \rightarrow c_1)$	$(\Gamma - Z, Y - \Gamma)$	0.71
	E_1	1.22	$(v_1 \rightarrow v_2), (v_1 \rightarrow c_3)$	$(\Gamma - Z), (\Gamma - Z)$	1.22, 1.23
	E_2	1.50	$(v_1 \rightarrow c_4), (v_3 \rightarrow c_1)$	$(\Gamma - Z, Y - Z), (T - Y)$	1.49, 1.55
	E_3	2.65	$(v_1 \rightarrow c_9), (v_1 \rightarrow c_{10})$	$(U - X, X - S), (U - X, X - S)$	2.60, 2.67
	E_4	3.02	$(v_3 \rightarrow c_9), (v_4 \rightarrow c_9)$	$(S - R), (S - R)$	2.99, 3.07
			$(v_3 \rightarrow c_{10})$	$(S - R)$	3.04
yy	E_0	0.71	$(v_1 \rightarrow c_1)$	$(\Gamma - Z, Y - \Gamma)$	0.71
	E_1	1.71	$(v_4 \rightarrow c_1)$	$(U - X), (T - Y)$	1.67
			$(v_6 \rightarrow c_2), (v_7 \rightarrow c_2)$	$(T - Y), (S - R)$	1.75, 1.72
	E_2	1.81	$(v_4 \rightarrow c_3)$	$(U - X, S - R)$	1.79
	E_3	2.14	$(v_7 \rightarrow c_2)$	$(Z - T, T - X)$	2.14
	E_4	2.65	$(v_{11} \rightarrow c_2)$	$(Y - T)$	2.63
	E_5	2.95	$(v_{11} \rightarrow c_2), (v_{13} \rightarrow c_2)$	$(R - U), (S - R)$	2.99
zz	E_0	0.71	$(v_1 \rightarrow c_1)$	$(\Gamma - Z, Y - \Gamma)$	0.71
	E_1	1.61	$(v_4 \rightarrow c_3)$	$(U - X, Y - \Gamma, R - U)$	1.61
	E_2	2.42	$(v_5 \rightarrow c_4)$	$(\Gamma - Z, Y - \Gamma, X - S, S - R)$	2.39
			$(v_6 \rightarrow c_4)$	$(S - R)$	2.43
	E_3	3.44	$(v_{20} \rightarrow c_2)$	$(Y - \Gamma, \Gamma - X)$	3.45

different peaks and features, each spectrum is decomposed to its individual pair contribution, i.e., he contribution from each pair of valence v_i and c_j bands (v_i-c_j) (see figures 7.6a and 7.6b) and plotting the transition band structure, i.e., the transition energy $E(k) = E_{cj}(k) - E_{vi}(k)$ along the high symmetry lines (not shown here). The counting of the bands is from the top (bottom) for the valence (conduction) bands. These techniques which have been used to analyse the spectra of the binary [25,26], the ternary [27,28] compounds and superlattices [29], allow the knowledge of the bands which contribute more to the peaks and their location in the BZ.

Table 7.4 *Optical transition in the PdPSe compound.*

Peak position (eV)			Transition	Region	Energy (eV)
xx	E_0	1.04	$(v_1 \rightarrow c_1)$	$(S-R)$	1.04
	E_1	1.79	$(v_1 \rightarrow c_3)$	$(S-R, R-U)$	1.76
			$(v_1 \rightarrow c_4)$	$(\Gamma-Z, R-S, R-U)$	1.79
	E_2	2.23	$(v_2 \rightarrow c_5)$	$(\Gamma-Z, R-U)$	2.19
	E_3	2.85	$(v_{12} \rightarrow c_1)$	$(R-S, X-S)$	2.84
	E_4	3.27	$(v_3 \rightarrow v_{10})$	$(\Gamma-Z, R-U, Z-T)$	3.24
	E_5	3.51	$(v_4 \rightarrow c_9)$	$(\Gamma-Y)$	3.50
yy	E_0	1.04	$(v_1 \rightarrow c_1)$	$(S-R)$	1.04
	E_1	2.25	$(v_6 \rightarrow c_7)$	$(S-R, T-Z)$	2.25
	E_2	2.65	$(v_9 \rightarrow c_2)$	$(\Gamma-Y, U-X)$	2.61
	E_3	2.82	$(v_{11} \rightarrow c_2)$	$(\Gamma-Z, X-S)$	2.81
	E_4	3.14	$(v_{10} \rightarrow c_4)$	$(\Gamma-Y)$	3.13
	E_5	3.26	$(v_{15} \rightarrow c_2), (v_{15} \rightarrow c_2)$	$(\Gamma-Y), (\Gamma-Y)$	3.21, 3.22
	E_6	3.64	$(v_{19} \rightarrow c_2)$	$(T-Y, T-Z)$	3.64
zz	E_0	1.04	$(v_1 \rightarrow c_1)$	$(S-R)$	1.04
	E_1	1.80	$(v_4 \rightarrow c_2)$	$(T-Y, S-R)$	1.80
	E_2	2.32	$(v_6 \rightarrow c_3), (v_7 \rightarrow c_2)$	$(\Gamma-Z), (T-Y)$	2.32, 2.32
	E_3	2.57	$(v_{13} \rightarrow c_2)$	$(Z-T, T-Y)$	2.57
	E_4	2.72	$(v_{15} \rightarrow c_2)$	$(R-U, S-R)$	2.70
	E_5	3.36	$(v_{15} \rightarrow c_1)$	$(\Gamma-Z, X-S)$	3.35
	E_6	3.74	$(v_{24} \rightarrow c_1), v_{25} \rightarrow c_1)$	$(\Gamma-Y, \Gamma-Z, X-S), (\Gamma-Y, \Gamma-Z)$	3.74, 3.76

The threshold energy occurs at 1.04 eV and 0.71 eV for PdPS and PdPSe and they are due to the v1-c1 transition along the (S−R) and (Γ−Y) directions respectively. For PdPS just above the absorption edge the three spectra are practically the same and this shoulder originates mainly from the v_1-$c_{1,2,3}$ transitions in the regions (S−R), (Γ−Z) in the BZ. Then ε_2^{xx} becomes smaller than the other two components of the dielectric tensor, i.e., ε_2^{yy} and ε_2^{zz}. However, for PdPSe ε_2^{xx} raises rapidily before becoming also smaller than ε_2^{yy} and ε_2^{zz}. The strongest absorption peak in PdPS is in ε_2^{yy}, E_1^{yy}, which has almost the same height as E_4^{zz}, while in PdPSe is in ε_2^{zz}, E_2^{zz} .

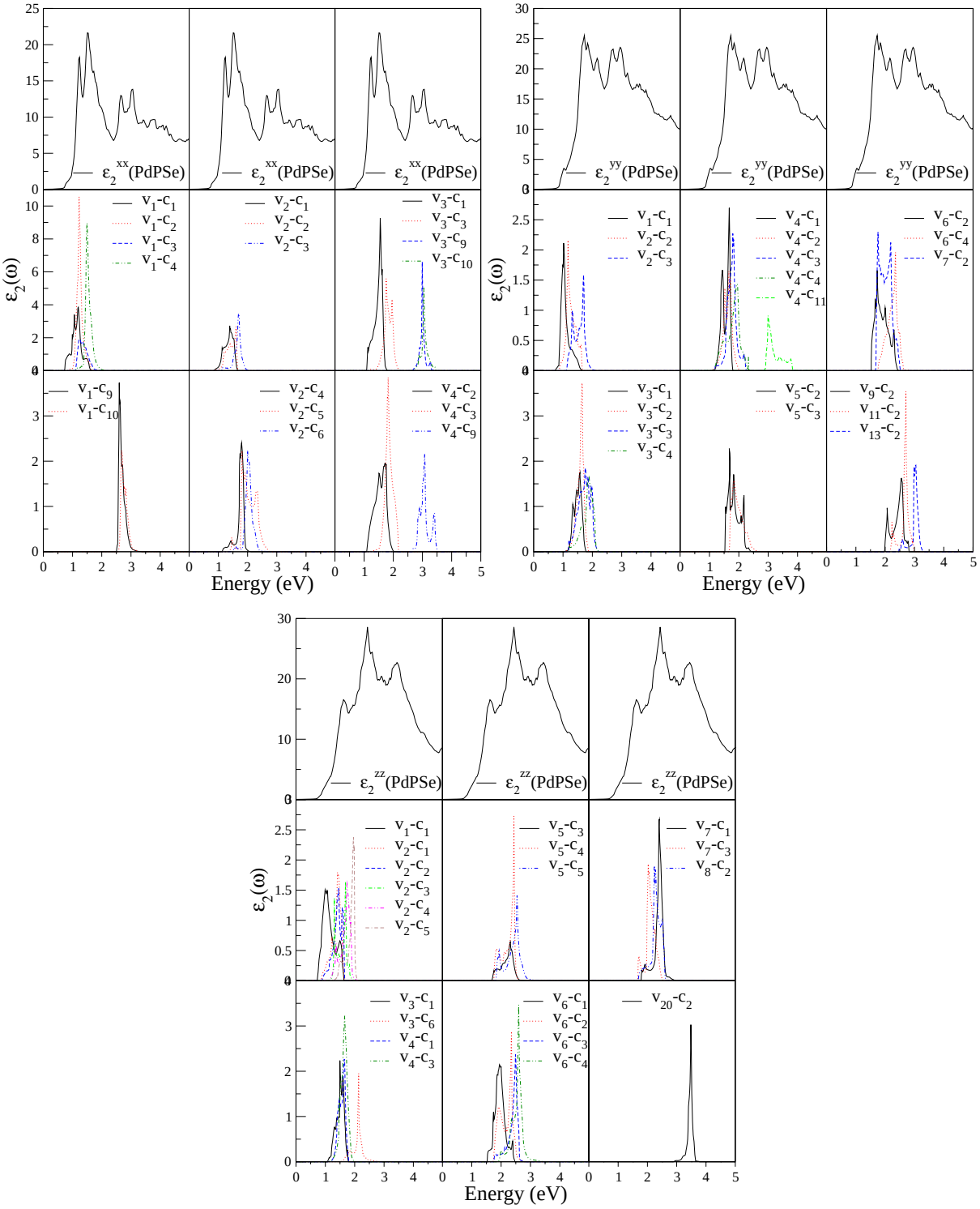

Figure 7.6a. Decomposition of ε_2^{xx}, ε_2^{yy} and ε_2^{zz} in partial band to band contribution. The upper panels show the total imaginary part in the direction x, y and z of PdPSe compound.

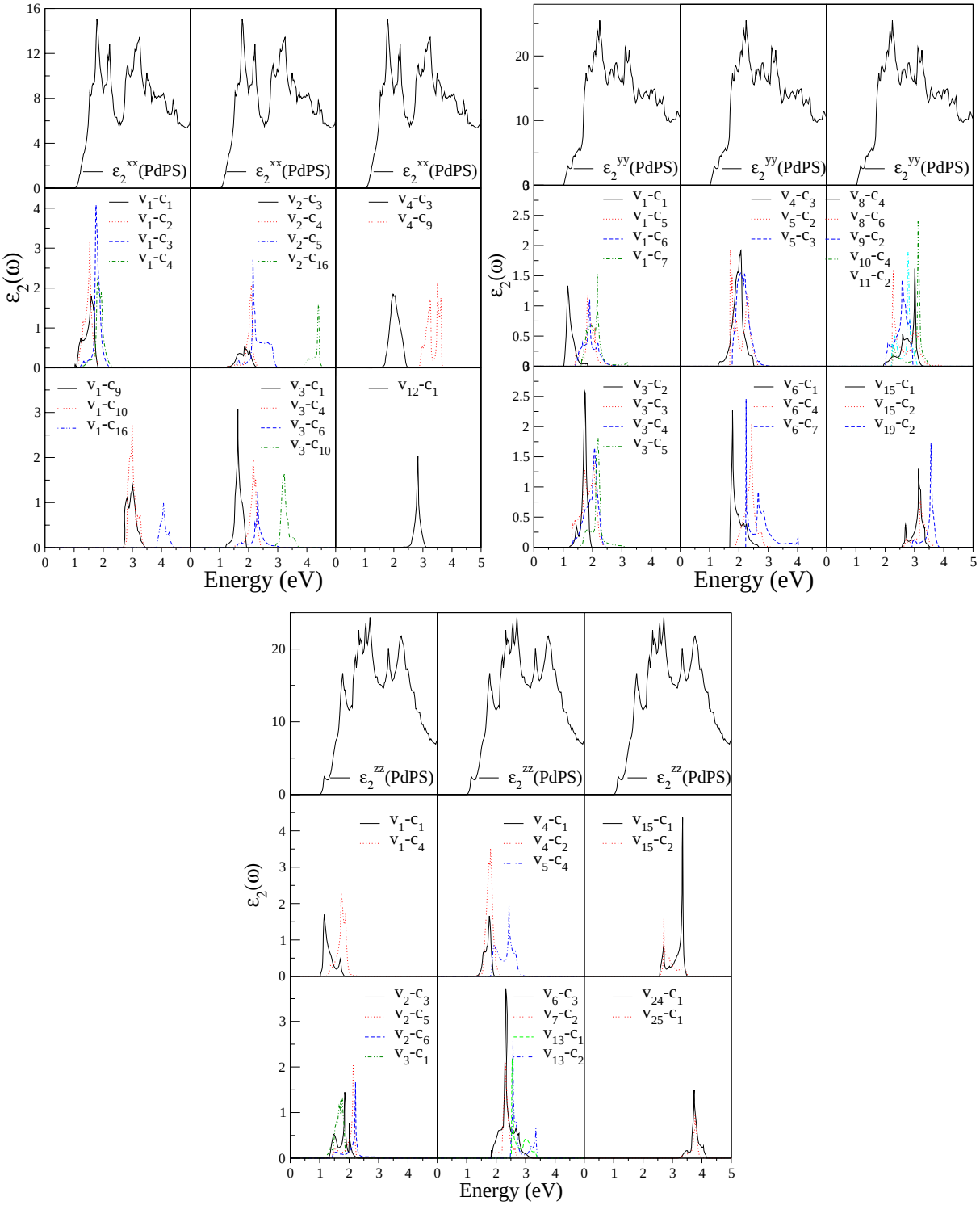

Figure 7.6b Decomposition of $\varepsilon_2^{xx}, \varepsilon_2^{yy}$ and ε_2^{zz} in partial band to band contribution. The upper panels show the total imaginary part in the direction x, y and z of PdPS compound.

These peaks can be identified as due to the v_6-c_7 in the (S−R) and (T −Z) directions in PdPS and from v_5-c_4 and v_6-c_4 ones in the (Γ−Z), (Γ−Y) and (X −R) directions in PdPSe. All the calculated spectra have two main features and a minimum between them (see figure 7.4; for example in PdPSe the two features are E_2^{xx} and E_3^{xx} in ε_2^{xx} , E_1^{yy} and E_2^{yy} in ε_2^{yy} and E_2^{zz} and E_3^{zz} in ε_2^{zz}).

Table 7.5 *Static value of* $\varepsilon_1(\omega)$ *of PdPS and PdPSe compounds*

		PdPS		***PdPSe***	
		uncorrected	***corrected***	***uncorrected***	***corrected***
$\varepsilon_1(0)$	*xx*	*15.74*	*12.66*	*11.75*	*10.21*
	yy	*19.68*	*16.08*	*17.09*	*1.67*
	zz	*19.20*	*15.78*	*16.78*	*14.46*

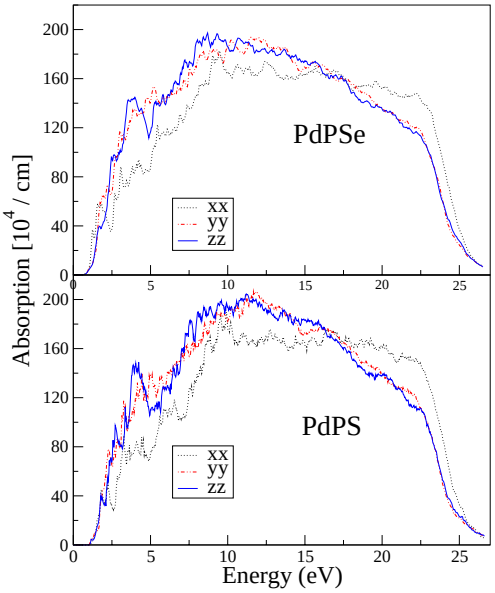

Figure 7.7 Calculated total absorption spectral response as a function of photon energy for different polarization planes for PdPS and PdPSe compounds.

The calculated energies of the peaks as well as the extended regions giving the dominent contributions to the elements of the structure in optical spectra are given in table 7.3 and 7.4. At higher photon energies the spectra decay rapidly with almost the same rate.

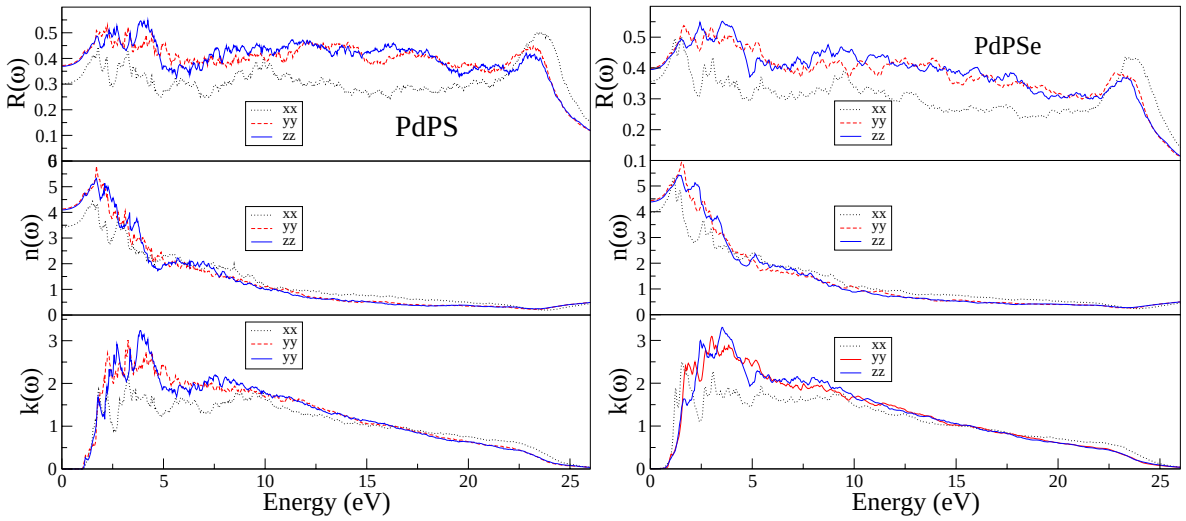

Figure 7.8 Calculated reflectivity, refractive index and the extinction coefficient spectra for PdPX compounds.

The real part of the elements of the dielectric tensor for PdPS and PdPSe were also calculated from the imaginary part using the Kramers-Kronig relations, but they are not shown here. We just give the static dielectric constants $\varepsilon_1^{xx}(0)$, $\varepsilon_1^{yy}(0)$ and $\varepsilon_1^{zz}(0)$. However, the values of the static dielectric constants are overestimated by the LDA as a consequence of the band gap underestimation [30,31]. It is found that a rigid shift of all conduction bands so as to match the calculated bandgaps with the experimental data can produce reliable results, i.e., very close to the measured ones (see table 6 of Ref. [27]). The theoretical values of the static dielectric constants (with and without shift) of the studied compounds are summarized in table 5. The values of $\varepsilon_1^{yy}(0)$ and $\varepsilon_1^{zz}(0)$ are almost the same for both compounds. The calculated results of the absorption, reflectivity and the indice of refraction and the extinction coefficients are shown in figures 7.7- 7.8. It is clear that there is a close resemblance between these spectra in the two compounds.

Table 7.6 *Value and energy of the complex index of refraction (n).*

	PdPS			PdPSe		
	n_{xx}	n_{yy}	n_{zz}	n_{xx}	n_{yy}	n_{zz}
n(0)	3.4289	4.13403	4.09712	3.96802	4.43711	4.3823
E(n=1)	11.06	10.51	10.43	11.14	10.19	9.37

The reason for this is the similar band structures of the two materials. For each compound, the absorption coefficients grow at different rates: α_{zz} being the fastest and α_{xx} the slowest. In the UV region α_{xx} is smaller than the other two absorption cofficients in both compounds. With regard to reflectivity, which represents another way which assesses how the electromagnetic energy is taken when interacting with a material medium, in both materials the one in the x direction R_{xx} is lower than R_{yy} and R_{zz}, except around 23 eV where it gets larger. This is in consistently with the absorption coefficients. The maximum of the reflectivity occurs in R_{zz} with a value of 54 % at 4.23 eV and 55 % at 3.55 eV in PdPS and PdPSe respectively. The values of refractive index n, which is an other optical parameter besides ε_1 which indicates how electromagnetic energy is dispersed when it penetrates in crystal, at zero energy are summarized in table 7.6, together with the energies for which n=1 ; i.e. no dispersion. There is an energy interval centred around these values for which n is close to one.

Table 7.6 *The values of the birefringence Δn at zero energy.*

	PdPS			PdPSe		
	Δn_a	Δn_b	Δn_c	Δn_a	Δn_b	Δn_c
Δn(0)	0.036	0.668	-0.705	0.039	0.413	-0.452

From the calculated refractive indices, we evaluated the birefringences along the three axes which are given by $\Delta n_a = (n_b - n_c)$, $\Delta n_b = (n_c - n_a)$ and $\Delta n_c = (n_a - n_b)$. The obtained results for the spectral behaviour of the birefringence $\Delta n_i(\omega)$ for the studied compounds are shown in figure 7.9. The birefringence is important only in the non absorbing region (below the energy gap) [32]. One may note that the general shape of the curves is similar and this is due to the similarity of the

underlying band structures. The $\Delta n_a(\omega)$ spectral dependence shows strong oscillations around zero in the energy range up to 10 eV. The values of the birefringence at zero energy are given in table 7.7.

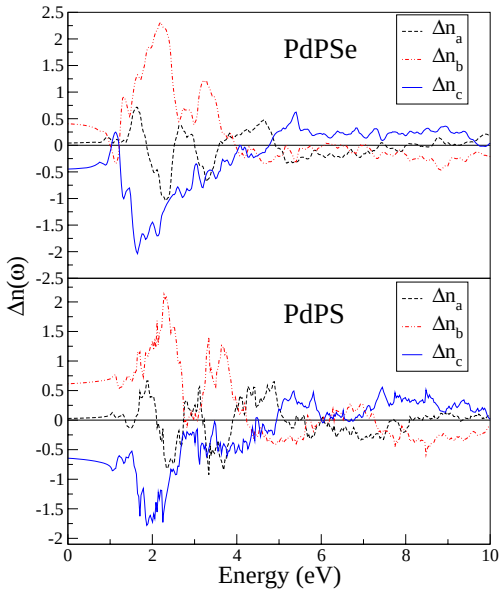

Figure 7.9 Calculated birefringence Δn(ω) for PdPX compounds

7.6. CONCLUSION

In conclusion, we have employed the all-electron full potential linear augmented plane wave plus local orbitals (FP-LAPW + lo) method with the LDA form of exchange and correlation to determine the structural and electronic properties of the orthorhombic compounds PdPS and PdPSe at normal pressure. The calculated equilibrium lattice constants and bulk moduli for these compounds were compared with the available experimental data when available, in all cases our results are in good agreement with the experimental data. The electronic properties are very well described by our calculations and show that these compounds have similar structures and the energy gap is indirect and decreases when S is replaced by Se. The anisotropic frequency dependent dielectric function, reflectivity, refractive index and absorption spectra are obtained and discussed in detail.

REFERENCES

1- D.W. Bullett, J. Phys. C: Solid State Phys. 15 (1982) 6163.

2- A.J. Foecker, W. Jeitschko, J. Solid State Chem. 162 (2001) 69.

3- S.L. Harmer, H.W. Nesbitt, Surf. Sci. 564 (2004) 38.

4- T.A. Bither, P.c. Donohue, H.S. Young, J. Solid State Chem. 3 (1971) 300.

5- J.K. Burdett, B.A. Coddens, Inorg. Chem. 27 (1988) 418.

6- A. Hamidani, B. Bennecer, K. Zanat, J. Phys. Chem. Solids 71 (2010) 42.

7- V. Marzik, J. Solid State Chem. 44 (1982) 380.

8- W. Jeitschko, Acta Cryst. B 30 (1974) 2565.

9- D. Singh, Planes Waves, Pseudo-Potentials and the LAPW Method, Kluwer Academic Publishers., Boston, Dortrecht, London, 1994.

10- P. Blaha, K. Schwarz, G.K.H. Madsen, D. Hvasnicka, J. Luitz, WIEN2k, An Augmented Plane Wave + Local Orbitals Program for Calculating Crystal Properties, Karlheinz Schwarz, Techn. Universit Wien, Austria, 2001, ISBN: 3-9501031-1-2.

11- P. Hohenberg, W. Kohn, Phys. Rev. 136 (1964) 864.

12- W. Kohn, L.J. Sham, Phys. Rev. A 140 (1965) 1113.

13- J. R Perdew, Y. Wang, Phys. Rev. B 45 (1996) 13244.

14- C. Ambrosch-Draxl, J.O. Sofo, Comput. Phys. Commun. 175 (2006) 1.

15- M. Alouani, S. Gopalan, M. Garriga, N. Christensen, Phys. Rev. Lett. 61 (1988) 643.

16- W.R.L. Lambrosch, B. Segall, J. Rife, W.R. Hunter, D.K. Wickenden, Phys. Rev. B 51 (1994) 13516.

17- F. Kalarasse, B. Bennecer, J. Phys. Condens. Matter 18 (2006) 7237.

18- F. Kalarasse, B. Bennecer, J. Phys. Chem. Solids 67 (2006) 1850.

19- A. Hamidani, B. Bennecer, Mater. Sci. Forum 609 (2009) 41.

20- F. Kootstra, P.L. de Boeij, J.G. Snijders, Phys. Rev. B 62 (2000) 7071.

21- C. Persson, R. Ahuja, A.F. da Silva, B. Johansson, J. Phys. Condens. Matter 13 (2001) 8945.

22- A.H. Reshak, S. Auluck, I.V. Kityk, J. Solid State Chem. 181 (2008) 789.

CONCLUSION

CONCLUSION

In the last four chapters we have presented the main results of this thesis which based on the total-energy calculations within the full-potential augmented plane-wave plus local orbitals (FP-LAPW + lo) method. We have used both the local density approximation (LDA) and generalized gradient approximations (GGA) for the exchange and correlation potential with including the spin-orbit effect. The correlated d-electron states are taken in the account by using the LSDA+U (GGA+U) methods with self-interaction correction method (SIC).

In Chapter 4 we have calculated the structural, elastic, electronic, magnetic and magneto-optical properties of the Mn-based half Heusler alloys (IrMnZ) where Z=Al, Sn and Sb. The energy minimization of these compounds indicates that the magnetic phase is the energetically favourable. The results show that IrMnAl are metallic and ferromagnetic. They are mechanically stable at zero pressure and possess the highest bulk, shear and Young's modulus, the sound velocities and the Debye temperatures are derived for the IrMnZ compounds. We have also found that in these compounds, the local moment of Mn is higher than the total moment. The reduction of the total moment is therefore accompanied by negative in Ir or in Z elements or in both, i.e., these atoms couple antiferromagnetically to the Mn moments. The hybridization between Ir and Mn is considerably larger. The local spin density approximation (LSDA) predicts that the IrMnAl have negligible magnetic moment. Furthermore, they predict that IrMnSb is a half metallic. While the LSDA+U (GGA+U) predict a large magnetic moment comparing to the experimental ones. Our results predict that the spin–orbit coupling is significant for these compounds, since they destroy the half-metallic band gap. We found the highest Kerr rotation arises at IrMnSb compound with weak values in IrMnAl in all the approximations used.

In Chapter 5 we have investigated the electronic, optical and magneto-optical properties of the Heusler compounds PbMnSb, and Pb_2MnSb. Our LSDA calculations reveal a gap in the E_F for PdMnSb, predicting half metallic nature. On the other hand, the LSDA+U move the d states away from the Fermi level but the shift of the unoccupied states make this compound metallic in both spin (up and down). The magnetic moments calculated by LSDA+U (GGA+U) for the present compounds are found to be very large comparing with the experimental ones. While the GGA give a good results. Furthermore, we found that the main contribution to the magnetic moments comes from Mn atom. We show that the LSDA+U can produce accurate optical properties; the calculated optical spectra using LSDA and LSDA+U are give good results as compared with the experimental data. We have observed that

LSDA+U gives an overall improvement of Kerr spectra with experiments. In another hand, a small difference in Kerr spectra appeared when we calculated it with and without inclusion of the Drude (intraband) contribution. Our calculations suggest that the magneto-optical are reproduce very well the experimental one when broadening is taken as 0.7 eV.

In Chapter 6 the structural and electronic properties of PdX_2 (X=P, S and Se), are investigated. The structural properties are determined through total energy and interatomic forces minimization. The calculated lattice constants and the atomic positions agree well with the experimental ones. Our results show that the studied compounds exhibit a metallic character with LDA. In another hand the LDA+U predict that PdS_2 is a semiconductor with narrow gap while PdP_2 and $PdSe_2$ have metallic character. The calculated density of states suggests that the absorption increases rapidly in the IR regions for PdP_2.

In Chapter 7 the structural, electronic and optical properties of the orthorhombic compounds PdPS and PdPSe at normal pressure are investigated. The calculated equilibrium lattice constants and bulk moduli for these compounds were compared with the available experimental data. Our results are in good agreement with the experimental data. The electronic properties are very well described by our calculations and show that these compounds have similar structures and the energy gap is indirect and decreases when S is replaced by Se. The anisotropic frequency dependent dielectric function, reflectivity, refractive index and absorption spectra are obtained and discussed in detail.